Chronic Ca^{2+} imaging of cortical neurons with long-term expression of GCaMP-X

by

Jinli Geng[1, 2#], Yingjun Tang[3#], Zhen Yu[1, 2#], Yunming Gao[1, 2], Wenxiang Li[1, 2], Yitong Lu[1, 2], Bo Wang[1, 2], Huiming Zhou[1, 2, 3], Ping Li[1], Nan Liu[5], Ping Wang[4], Yubo Fan[1], Yaxiong Yang[1]*, Zengcai V. Guo[3]*, Xiaodong Liu[1, 2]*

[#]Equal contributions

[*]Corresponding authors

[1]Advanced Innovation Center for Biomedical Engineering, School of Biological Science and Medical Engineering, School of Engineering Medicine, Key Laboratory for Biomechanics and Mechanobiology of Ministry of Education, Beihang University, Beijing, 100083, China.

[2]X-Laboratory for Ion-Channel Engineering, Beihang University, Beijing 100083, China;

[3]Tsinghua-Peking Joint Center for Life Sciences, IDG/McGovern Institute for Brain Research, School of Medicine, Tsinghua University, Beijing 100084, China;

[4]Laboratory for Biomedical Engineering of Ministry of Education, Zhejiang University, Hangzhou 310027, China.

[5]Center for Life Sciences, School of Life Sciences, Yunnan University, Kunming 650091, China.

Lead contact: Xiaodong Liu liu-lab@buaa.edu.cn;

Word count of title: 11

Word count of abstract: ~280

Word count of main text: ~6,900

Total figure count: 7

References: ~70

Running titles: Long-term Ca^{2+}/GCaMP-X imaging of neurons

Abstract

Dynamic Ca^{2+} signals reflect acute changes in membrane excitability (e.g. responses to stimuli), and also mediate intracellular signaling cascades that normally take longer time to manifest (e.g., regulations of transcription). In both cases, chronic Ca^{2+} imaging has been often desired, but largely hindered by unexpected cytotoxicity intrinsic to GCaMP, a popular series of genetically-encoded Ca^{2+} indicators. Here, we demonstrate the performance of GCaMP-X in chronic Ca^{2+} imaging with long-term probe expression in cortical neurons, which has been designed to eliminate the unwanted interactions between conventional GCaMP indicators and endogenous (apo)calmodulin-binding proteins. By expressing in live adult mice at high levels over an extended time frame, GCaMP-X indicators showed less damage and improved performance in two-photon imaging of acute Ca^{2+} responses to whisker deflection or spontaneous Ca^{2+} fluctuations. Chronic Ca^{2+} imaging data (≥1 month) were acquired from cultured cortical neurons expressing GCaMP-X, unveiling that spontaneous/local Ca^{2+} transients would progressively develop into autonomous/global Ca^{2+} oscillations. Besides the morphological indices of neurite length and soma size, the major metrics of oscillatory Ca^{2+}, including rate, amplitude and synchrony were also examined along with the multiple stages (from neonatal to mature) during neural development. Dysregulations of both neuritogenesis and Ca^{2+} oscillations were observed typically in 2-3 weeks, which were exacerbated by stronger or prolonged expression of GCaMP. In comparison, neurons expressing GCaMP-X exhibited significantly less damage. By varying the timepoints of virus infection or drug induction, GCaMP-X outperformed GCaMP similarly in cultured mature neurons. These data altogether highlight the unique importance of oscillatory Ca^{2+} to morphology and health of neurons, presumably underlying the differential performance between GCaMP-X and GCaMP. In summary, GCaMP-X provides a viable option for Ca^{2+} imaging applications involving long-time and/or high-level expression of Ca^{2+} probes.

Introduction

Ca^{2+} signals play pivotal roles in the brain, closely involved in membrane excitability, sensory transduction, synaptic transmission, neural development and plasticity (Berridge et al., 2003). Ca^{2+} dysregulations are linked with the mental disorders including Parkinson's diseases, Alzheimer's diseases, epilepsy and schizophrenia (Chan et al., 2007; Fernandez de Sevilla et al., 2006; Khan et al., 2020; Liebscher et al., 2016), suggesting that multiple factors and cascades may converge to Ca^{2+} as one of the central factors underlying brain diseases, referred as the calcium hypothesis (Berridge, 2010). According to their downstream consequences, cellular Ca^{2+} signals could be categorized as genomic versus non-genomic, to reflect the fact that in some cases where gene expressions are regulated (chronic) versus in other cases only the (acute) functions of existing proteins are concerned.

Acutely, cellular Ca^{2+} reflects single-neuron activities, such as spontaneous fluctuations and stimulus-evoked responses (Chen et al., 2013; O'Banion and Yasuda, 2020). Ca^{2+} imaging is often utilized to measure neuronal excitability, as one alternative to electrical recording. In fact, genetically encoded Ca^{2+} indicators (GECI) represented by GCaMP, based on CaM (calmodulin) and Ca^{2+}/CaM-binding motif M13, have been broadly applied to monitor neurons and other excitable cells (Akerboom et al., 2012; Chen et al., 2013; Dana et al., 2019; Nakai et al., 2001; Tallini et al., 2006; Tian et al., 2009; Yang et al., 2018). In addition to a faithful index of acute responses (in the timescale of seconds/minutes, such as a burst of action potentials), Ca^{2+} is often tightly coupled to various chronic effects or processes, e.g., Ca^{2+}-dependent gene transcription and expression, neurite outgrowth or pruning, long-term potentiation or depression, learning and memory, and neural degeneration (O'Banion and Yasuda, 2020). Therefore, it is highly desirable to monitor the long-term Ca^{2+} dynamics (days/weeks or longer) for cells, tissues, organs or even whole organisms, which would greatly facilitate mechanistic understanding of the genomic/chronic roles of Ca^{2+} in diverse pathophysiology (Garcia et al., 2017). Meanwhile, back to the context of non-genomic Ca^{2+}, longitudinal imaging may have a broad scope of applications where long-term changes in responses or behaviors are of interest. In parallel with Ca^{2+} imaging, different types of electrodes, such as MEA (multiple electrode array) and flexible electronics, have been extensively deployed for cultured neurons, brain slices, live animals or

89 human brains to record neural activities in the format of neuronal action potentials, local field
90 potentials and EEG (Hong and Lieber, 2019). The goal is to monitor neural activities across
91 multiple days, weeks or even the entire lifespan in the studies of training/behaviors, retina/vision,
92 brain disorders, addictions, and pharmacological and interventional therapeutics (Aramuni and
93 Griesbeck, 2013; Couto et al., 2021). GECIs hold great promise to avoid chronic immune
94 responses and recoding instability that electrodes are often encountered with (Aramuni and
95 Griesbeck, 2013). Indeed, GCaMP and other GECIs have been demonstrated as more
96 advantageous methods over electrodes or dyes during chronic imaging of neurons (Aoki et al.,
97 2017; Murphy et al., 2020; Tian et al., 2009). Unfortunately, neural toxicities often accompany
98 long-term expression of GCaMP or chronic GCaMP imaging with either virus-infected (Chen et
99 al., 2013; Tian et al., 2009; Yang et al., 2018) or transgenic neurons (Steinmetz et al., 2017).
100 Perturbing L-type Ca_V1 channels and presumably other (apo)CaM-binding proteins, GCaMP
101 indicators cause side-effects in neurons which have been documented especially for enhanced or
102 prolonged expressions. The unwanted molecular events of GCaMP may or may not be
103 manifested as the toxic effects at the cellular or system levels. For instance, when employing
104 viral infection, imaging experiments are restricted within the empirical time window and dosage
105 range to alleviate nuclear-filling of GCaMP (Resendez et al., 2016); or for transgenic mice, special
106 promoters, conditional expression and other tactics are utilized to reduce the expression level/time
107 of GCaMP (Madisen et al., 2015). With such work-around solutions, rich information and rapid
108 progress in neurosciences have been achieved by GCaMP imaging. At a cost, special cautions
109 and procedures are required due to GCaMP toxicity, e.g. virus dilution trials (Resendez et al.,
110 2016), which often cause inconvenience in experiments besides other potential problems (e.g.,
111 nucleus-filling or low SNR).
112 Under the testing conditions in this work, neuronal perturbations were evidenced from
113 GCaMP: with either earlier or newer versions, for either viral or transgenic expression, either *in*
114 *vitro* (cultured neurons) or *in vivo* (living mice), and on either acute sensory response to whisker
115 deflection or spontaneous oscillation encoding genomic Ca^{2+}. GCaMP-X has been designed to
116 resolve these perturbations by eliminating unwanted interferences with endogenous
117 (apo)calmodulin signaling. For *in vivo* imaging beyond the safe time-window (3-week extension)

and dosage (10-fold higher), GCaMP-X outperformed GCaMP in recapitulating both sensory responses to whisker stimulation and autonomous Ca^{2+} fluctuations. In cultured cortical neurons, GCaMP of strong and/or prolonged expression caused the damage to neurites accompanied by aberrant Ca^{2+} oscillations, all overcome by GCaMP-X as a simple solution, which also highlights the importance of oscillatory Ca^{2+} to neurons both *in vitro* and *in vivo*.

RESULTS

Design principles of GCaMP-X validated by newer GCaMP versions

Recently, GCaMP has been updated to its newest versions jGCaMP7 (but also see the bioRxiv preprint of jGCaMP8 (Zhang et al., 2021)), with enhanced sensing performance in multiple aspects over the previous GCaMP6 (Dana et al., 2019; Grødem et al., 2021). Considering that the design of jGCaMP7 is also on the basis of CaM, we postulated that jGCaMP7-contained apoCaM would have similar problems to those of earlier GCaMPs. We chose jGCaMP7b to further validate the design principles of neuron-compatible GCaMP-X established in our previous work (Yang et al., 2018). Following the protocol of transient transfection (***Figure 1A***), jGCaMP7b accumulated into the nuclei in a substantial subpopulation of cortical neurons indexed by N/C (nucleus/cytosol) ratio (***Figure 1B***), considered as the hallmark of GCaMP side-effects. Notably, jGCaMP7b exhibited even more severe nuclear accumulation than other GCaMP variants, which may account for the nuclear jGCaMP7b evidenced *in vivo* (Dana et al., 2019). Accordingly, the total length (***Figure 1C***) and the complexity (***Figure 1D***) of neurites were significantly reduced in jGCaMP7b-expressing neurons. The apoCaM-binding motif (CBM) and the localization tags were then appended onto jGCaMP7b, following the design of GCaMP-X (Yang et al., 2018), to construct jGCaMP7b-X_C and jGCaMP7b-X_N for cytosolic and nuclear Ca^{2+} imaging respectively. GCaMP-X is supposed to eliminate its binding to apoCaM targets in neurons and reduce the cytotoxicity intrinsic to GCaMP, a critical issue to long-term Ca^{2+} monitoring. Depicted by neurite tracing (***Figure 1A***), both cytosolic and nuclear versions of GCaMP7-X have greatly enhanced the compatibility with neurons. In fact, neurons expressing GCaMP7-X were essentially indistinguishable from GFP control neurons, in direct contrast to the neurons transfected with GCaMP7 of the same amount of cDNA (***Figure 1C, D***). In light of

electrophysiological analyses on calmodulation of Ca_V1 channels (Ben-Johny and Yue, 2014; Yang et al., 2018), we examined the effects of jGCaMP7b on recombinant $Ca_V1.3$ channels in HEK293 cells. jGCaMP7b significantly altered the major properties of $Ca_V1.3$ gating, i.e., both inactivation and activation were enhanced (***Figure 1E***). The expression level is a critical factor to evaluate the side effects of GCaMP. We then examined the actual levels of expressed proteins in HEK293 cells when transiently transfected with the same amount of cDNA for different indicators (**Figure 1—figure supplement 1**). Demonstrated by both western blotting and immunohistochemistry, jGCaMP7b in HEK293 cells was expressed either in the cytosol or in the nucleus at the same levels as jGCaMP7b-X_C or jGCaMP7b-X_N, respectively. Likewise, GCaMP7 and GCaMP7-X were at the same cytosolic or nuclear levels of expression when transiently transfected into neurons (**Figure 1—figure supplement 2**). Moreover, by co-expressing GCaMP7b-X_C and GCaMP7b-X_N, the total expression level estimated by immunostaining was even higher than that of jGCaMP7b, the latter of which caused significant damage to neurites whereas the total neurite length of GCaMP7b-X neurons was about the same as GFP control neurons. Therefore, the expression levels of GCaMP-X versus GCaMP did not underlie their differential performances.

Notably, by coimmunoprecipitation GCaMP bound $Ca_V1.3$ (α_{1D}) at its apoCaM binding domain whereas GCaMP-X was found no binding (**Figure 1—figure supplement 3**). Similarly, neurogranin, an important postsynaptic apoCaM-binding protein (Gerendasy and Sutcliffe, 1997), was unveiled to bind GCaMP but not GCaMP-X. Thus, the above direct evidence of molecular interactions further consolidated the design principles of GCaMP-X, serving as the major candidate mechanism of cellular GCaMP toxicities.

Acute sensory responses monitored by viral expression of GCaMP-X *in vivo*

GECIs including GCaMP have been widely applied to monitor neuronal responses to various stimuli. Due to the cytotoxicity known from the very early versions of GCaMP, *in vivo* imaging experiments are normally required to conduct within the time window. In practice, an optimal time window (OTW) is about 3-8 weeks post injection for GCaMP-infected neurons of live mice (Chen et al., 2013; Huber et al., 2012; Resendez et al., 2016), in order to achieve substantial levels

of GCaMP expression and fluorescence but not too high levels prone to side effects. Here we investigated into the Ca^{2+} dynamics under whisker stimulation within or beyond OTW by applying the adeno-associated viruses (AAV) of GCaMP6m or GCaMP6m-X_C with the neuro-specific *Syn* promoter to S1 primary somatosensory cortex in the brain of adult mice (2-month age or older) (***Figure 2A***). To exclude the potential bias due to level of expression, GCaMP6m-X_C viruses ($1.0x10^{13}$ v.g./ml) of higher dose than GCaMP6m ($1.0x10^{12}$ v.g./ml) were injected (60 nl/injection). Progressive nuclear accumulation of GCaMP was previously reported *in vivo* and *in vitro* (Chen et al., 2013; Yang et al., 2018; Zariwala et al., 2012). Consistently, by the criteria of N/C ratio (0.8), nucleus-filling GCaMP was observed in a fraction of neurons 4-6 weeks post injection, and the average N/C ratio was substantially increased when examined 8-13 weeks post injection (***Figure 2B***). In direct contrast, no neuron expressing GCaMP6m-X_C fell into the nucleus-filled category even weeks beyond OTW (up to 13 weeks post injection). In the earlier study (Chen et al., 2013), the impairment on visual responses was reported from nucleus-filled neurons after long-term expression of GCaMP6 (several months post injection); and during the initial phase (1-2 month post injection) nuclear GCaMP did not perturb the proper physiology of neurons. Here, nucleus-filled neurons expressing GCaMP (N/C ratio > 0.8) started to show less responsiveness than neurons expressing GCaMP-X_C as early as within OTW (4-6 weeks) (***Figure 2A)***, which may underlie the lower amplitude of Ca^{2+} responses ($\Delta F/F_0$) averaged over the whole population of neurons (***Figure 2C***). Another two indices of success rate and SNR (signal to noise ratio) were also consistent with the above notion that within OTW neurons filled with nuclear GCaMP might have been impaired. Beyond OTW (8-13 weeks), GCaMP was more frequently and clearly found in the nucleus, and the neurons exhibited more significant differences from GCaMP-X_C according to all the three indices of $\Delta F/F_0$, success rate and SNR.

Our data have extended the advantages of GCaMP-X over GCaMP from *in vitro* onto *in vivo*. Collectively, neurons may suffer from GCaMP side-effects either within or beyond OTW, for which nuclear GCaMP expression appears to be a critical factor. GCaMP-X outperformed GCaMP in imaging sensory-evoked Ca^{2+} dynamics especially beyond OTW, which provides a simple but promising solution for long-term Ca^{2+} imaging.

Long-term monitoring of Ca^{2+} oscillations by GCaMP-X_C *in vitro*

Before proceeding further with *in vivo* GCaMP-X imaging, we decided to conduct in-depth examinations on the long-term performance of GCaMP-X under *in vitro* conditions. Of note, slow Ca^{2+} oscillations have been observed from a variety of excitable or non-excitable cells (Uhlen and Fritz, 2010). In neurons, oscillatory Ca^{2+} signals can increase the efficiency and specificity of gene expression (Dolmetsch et al., 1998; Li et al., 1998), thus playing important role in neuronal functions, development, morphology and even general health (Kamijo et al., 2018; Nicotera and Orrenius, 1998; Toth et al., 2016). Spontaneous electrical activities are initiated at the early stage of neural development, and subsequently become more synchronized (Luhmann et al., 2016; Spitzer, 2006). Such longitudinal processes of oscillatory Ca^{2+} and neuritogenesis which are mechanistically coupled may serves as a perfect scenario to demonstrate the side-effects of GCaMP on neurons. We then hypothesized that GCaMP-X versus GCaMP neurons would make a clear difference in their chronic recordings of oscillatory Ca^{2+} signals. Meanwhile, GCaMP-X with enhanced neuron-compatibility is expected to provide new insights into the roles of spontaneous Ca^{2+} oscillations in neuronal morphology (Gomez and Zheng, 2006; Rosenberg and Spitzer, 2011). To monitor such Ca^{2+} dynamics *in vitro*, the adeno-associated viruses (AAV) carrying GCaMP6 or GCaMP6-X_C (for *in-vitro* use) were equally (1 μl, $1x10^{12}$ v.g./ml) added to the cortical neurons of neonatal mice (DIV 0, 0 day *in vitro*) which were maintained and examined till DIV 28 (***Figure 3A, B***). Fluctuations of Ca^{2+} activities were perceivable starting from the first week (DIV 3 and DIV 6) with GCaMP6-X_C, in the pattern of high-frequency, low-amplitude and unsynchronized signals. On DIV 10, the oscillation frequency decreased while the amplitude was increased with an enhanced level of synchronization. On DIV 28, Ca^{2+} oscillations of individual or sub-grouped neurons became widely synchronized featuring robust spikes and slow frequency (***Figure 3—video 1***), indicative of the formation of neural circuitry. In contrast, Ca^{2+} signals were severely distorted in GCaMP6-infected DIV-10 neurons. Despite that the performance of GCaMP6 in the first week resembled GCaMP6-X_C, longer expression time of GCaMP6m resulted in altered patterns of Ca^{2+} oscillations (***Figure 3—video 2, 3***). One major abnormity was the substantial reduction in oscillatory activities of GCaMP6-expressing neurons, which was manifested after DIV 10 by much longer intervals between two adjacent peaks

and much smaller amplitudes in average. Occasionally, abnormal Ca^{2+} spikes with ultralong lasting duration could be observed on DIV 17 (***Figure 3B, Figure 3—video 2***). Around DIV 28, cease of Ca^{2+} oscillations and broken neurites were often evidenced (***Figure 3—video 3***). We then further analyzed oscillatory Ca^{2+} signals by the frequency and other key indices across the timespan from DIV 3 up to DIV 28. Statistical results demonstrated that the frequency of Ca^{2+} fluctuation with GCaMP6m-X_C was about 150 mHz during the first week, then gradually declined to the plateau around 20 mHz (***Figure 3C***). Meanwhile, the peak amplitude exhibited a rising trend in the neurons expressing GCaMP6m-X_C across the full term (***Figure 3D***). In contrast, both the frequency and the amplitude of Ca^{2+} oscillations acquired by GCaMP6m were drastically changed after DIV 17, and then even more deteriorated later in that the oscillation was less and less recognizable and eventually halted on DIV 28 (***Figure 3C, D***). Synchronization is one major hallmark of autonomous Ca^{2+} oscillations, which was evaluated by the mean of correlation coefficient. As demonstrated by the temporal profiles of correlation coefficients, the comparison between GCaMP6m versus GCaMP6m-X_C unveiled a crucial phase turning from increasing to decreasing synchronization around DIV 17-21 in GCaMP6m-expressing neurons (***Figure 3E***). Likewise, the full width at half maximum (FWHM), another index of oscillatory waveforms, was aberrantly wider for GCaMP6m than GCaMP6m-X_C, becoming noticeable on DIV 10, and much more pronounced (10-fold) later on (***Figure 3F***). Collectively from these indices, GCaMP indeed caused progressive damage on cortical neurons along with the culturing time or developmental stages; in contrast, GCaMP6m-X_C has overcome nearly all the above negative effects, emerging as a promising tool for chronic Ca^{2+} imaging with enhanced neural compatibility. Also, Fast Fourier Transformation (FFT) was applied to the Ca^{2+} waveforms acquired by GCaMP6-X_C (***Figure 3G*** and ***Figure 3—figure supplement 1***). The distribution of frequency components started to change during DIV 10-17, when slow Ca^{2+} oscillations of 10-100 mHz appeared to be the dominant form (***Figure 3H***). Based on separate preparations of neurons, we conducted another two experiments to compare GCaMP6m and GCaMP6m-X_C up to DIV 42 (***Figure 3—figure supplement 2***). Statistical results from these data on frequency, $\Delta F/F_0$, correlation coefficient per view and FWHM support that GCaMP-X outperforms GCaMP in chronic Ca^{2+} imaging of cultured neurons (***Figure 3I***). The newer probes of jGCaMP7b and

jGCaMP7b-X_C resulted in differential performance that jGCaMP7b-X_C was much less toxic, consistent with the above notion (***Figure 3—figure supplement 3***).

In summary, the same set of neurons were chronically monitored with GCaMP-X across the development stages from newborn to mature, by which the temporal profiles of the major characteristics were achieved for oscillatory Ca^{2+} signals in cultured cortical neurons. As one additional control, Fluo-4 AM (Ca^{2+} dye) imaging was conducted for synchronized Ca^{2+} oscillations on DIV 21 (***Figure 3—figure supplement 4***). The key parameters of Ca^{2+} dynamics measured by GCaMP7b-X_C were much closer to those by Fluo-4 AM than GCaMP7b, supporting that GCaMP7b-X_C is less toxic than GCaMP7b. Minor to moderate differences still existed between Fluo-4 AM and GCaMP7b-X_C, which were more likely attributed to intrinsic probe properties (e.g., Ca^{2+} sensing kinetics) rather than neuronal toxicities.

Close correlations between autonomous Ca^{2+} oscillations and neuronal morphology *in vitro*

Spontaneous Ca^{2+} oscillations, the slow periodic Ca^{2+} waveforms in particular, are tightly coupled with neuronal morphology, development and neuritogenesis (Kamijo et al., 2018; Toth et al., 2016). GCaMP-X promises unprecedented opportunities for concurrent imaging of both neuronal functionalities and morphogenesis across different stages of development. Such chronic Ca^{2+} imaging is difficult to implement if using other approaches, e.g., conventional GCaMP or Ca^{2+} dyes, both would cause side-effects to neurons (Smith et al., 2018; Yang et al., 2018). By taking advantage of GCaMP-X, we here aimed at the relationship between cellular Ca^{2+} and neuronal morphology.

Indistinguishable from control neurons infected with GFP viruses (***Figure 4—figure supplement 1***), neurons expressing GCaMP6m-X_C followed the typical development process of neonatal neurons, including neurite elongation/arborization and soma enlargement (***Figure 4A***). In contrast, these developmental processes were severely impaired by virally-delivered GCaMP6m, especially after DIV 14 onwards, when nuclear accumulation and neurite shortening became evident. Depicted by DIV-28 neurons with neurite tracings, GCaMP6m caused significant damage on neurite outgrowth, and to the extreme, discernable death of neurons, in contrast to GCaMP6m-X_C which had no apparent perturbation. In addition, the temporal profiles

across the full time-course were achieved for both GCaMP6m (***Figure 4B***) and GCaMP6m-X_C (***Figure 4C***) by the major indices of neurite length and soma size. At the early phase (before DIV 17), no significant difference between the two groups of GCaMP6m versus GCaMP6m-X_C could be detected. However, toward the late stage (DIV 28 or later) of GCaMP-expressing neurons, the soma size was as small as ~200 μm^2 in contrast to the neurons expressing GFP or GCaMP6m-X_C (~300 μm^2), as confirmed by the statistical summary over three independent experiments (***Figure 4—figure supplement 1*).** Likewise, the total neurite length of GCaMP-expressing neurons rapidly declined, whereas GCaMP-X expressing neurons went through an initial phase (~ 2 weeks) of rapid outgrowth before entering into the plateau phase, forming a monotonic increasing curve. Similar to neuritogenesis, the temporal profile of soma size also exhibited an upward-plateau trend (***Figure 4C***). Combining the data and analyses from both developmental and functional perspectives (***Figure 3*** and ***Figure 4***), we speculated on the potential correlations between neuronal growth and spontaneous Ca^{2+} activities (***Figure 4—figure supplement 2***). Functionally, Ca^{2+} dynamics appeared to be either ascending (amplitude) or descending (frequency) along with the developmental stages (DIV) (***Figure 4D***). Roughly, the oscillation amplitude linearly (R^2=0.84) correlated with the neurite length in total (***Figure 4—figure supplement 2A***). In direct contrast, the oscillation frequency and the total neurite length were inversely correlated (R^2=0.99) (***Figure 4—figure supplement 2B***). Resembling the amplitude, the level of synchrony (correlation coefficient) indicative of circuitry formation was positively correlated with the total neurite length (R^2=0.86) (***Figure 4—figure supplement 2C)***. All these tight correlations support the notion that spontaneous Ca^{2+} activities including its mature form of synchronized Ca^{2+} oscillations may underpin neuritogenesis (Estrada et al., 2006; Gomez and Zheng, 2006; Kamijo et al., 2018). According to the spectral analyses (***Figure 3G, H***), the frequency band of 10-100 mHz played a crucial role in Ca^{2+}-dependent neuritogenesis.

Previous studies mainly relied on measuring transient Ca^{2+} and neurite growth-rate within a brief period of time (Ito et al., 2010; Mukai et al., 2010; Rosenberg and Spitzer, 2011; Van et al., 2004). However, the overall neurite outgrowth across the developmental phases may help elucidate the roles of Ca^{2+} in neuritogenesis, which has been lacking due to the difficulties of long-term Ca^{2+} imaging. In fact, contradictory observations have been reported regarding how

Ca^{2+} actually regulates the rates of neuronal growth. Here, based on GCaMP-X imaging data, the first derivative of the growth curves was calculated as the growth rate of neurite or soma (***Figure 4E***). The bell-shaped curves suggested that the relationships between Ca^{2+} oscillations and neuronal growth rates may depend on developmental stages, which reached the peak rates around DIV 10 for both neurite length and soma size. Therefore, the maximum growth rate appeared to be determined by both amplitude and frequency of Ca^{2+} oscillations. In general, there might not be a simple relationship between oscillation characteristics and neuronal development. Within a short or brief timeframe, the growth rates in relation to various combinations of amplitude and frequency could be complicated (Gomez and Zheng, 2006), especially without considering the development stage of neurons. Similar results were obtained from jGCaMP7b-X_C in comparison with jGCaMP7b (***Figure 4—figure supplement 3***). In summary, chronic GCaMP-X imaging provided a glimpse of the potential roles of slow Ca^{2+} oscillations in neuritogenesis across multiple stages of neuronal development.

To further exclude any potential artifact related to probe expressions, a gradient of expression levels by jGCaMP7b-X_C viruses were examined in cultured cortical neurons (***Figure 4—figure supplement 4***). 3 μl AAV-*Syn*-jGCaMP7b-X_C (1.0×10^{12} v.g/ml) and 1 μl AAV-*Syn*-jGCaMP7b (1.0×10^{12} v.g/ml) led to the similar levels of whole-cell expression (the former would express much more in the cytosol). Under such conditions, the results from the two groups of neurons were consistent with those with equal amounts/volumes of viruses. jGCaMP7b-X_C was much less toxic than jGCaMP7b, by comparing the indices of neuronal growth and Ca^{2+} oscillations (***Figure 4—figure supplement 4F***), where neurite length and soma size of neurons expressing high-level jGCaMP7b-X_C were nearly indistinguishable from GFP control neurons.

Chronic imaging of spontaneous Ca^{2+} activities *in vivo*

GCaMP6m perturbed autonomous Ca^{2+} oscillations, presumably as one leading cause of neuronal toxicities. Such tight correlations between Ca^{2+} dysregulations and aberrant morphology were clearly manifested during early development, which may extend onto mature neurons. The viruses were added to cultured cortical neurons at the mature stage (DIV 21), which were

subsequently examined to compare the effects of jGCaMP7b versus jGCaMP7b-X_C (***Figure 5—figure supplement 1***). Analyses of both neurites and oscillations demonstrated similar side-effects of jGCaMP7b in comparison with jGCaMP7b-X_C, starting to show up on DIV 28 and later on DIV 35 exhibiting significant differences in neurite length and oscillation characteristics. Similar to cultured neurons, spontaneous Ca^{2+} activities *in vivo* are also correlated to gene transcription and expression at the cellular and circuity levels (Laviv et al., 2020; Takahashi et al., 2016). Therefore, based on our experiments and other published reports, a common theme of correlation exists between spontaneous Ca^{2+} and neuronal morphology, for both premature and mature neurons, and both *in vitro* and *in vivo* (***Figure 5—figure supplement 2***). For adult mouse brain infected by AAV viruses of GCaMP6m or GCaMP6m-X_C (the same procedures and dosages as in ***Figure 2***), we characterized spontaneous Ca^{2+} activities in S1 primary somatosensory cortex (***Figure 5A, B*** and ***Figure 5—video 1, 2***). Two checkpoints were set at 4-weeks post virus injection (within OTW) and at 8- or 11-weeks post virus injection (prolonged expression time beyond OTW), respectively. Similar to whisker deflection-response experiments in ***Figure 2***, the nucleus-filled neurons exhibited noticeable abnormalities in spontaneous Ca^{2+} activities even within OTW. Beyond OTW, nucleus-filling was often found from GCaMP6m while very rare from GCaMP6m-X_C as indexed by N/C ratio (***Figure 5C***). Accordingly, the damage was much exacerbated, as evidenced from the total or nucleus-filled neurons expressing GCaMP in comparison with the total neurons expressing GCaMP-X (***Figure 5D***). With GCaMP6m, the frequency and amplitude resulted in significantly lower values, accompanied by aberrantly wider FWHM and slower on/off rates. In contrast, neurons expressing GCaMP6m-X_C maintained robust and stable spontaneous Ca^{2+} activities with key characteristics within the normal ranges across the full term of experiments (up to 11 weeks post virus injection). Notably, GCaMP6m-X_C significantly improved the SNR calculated from spontaneous Ca^{2+} signals *in vivo*, both within and beyond OTW (***Figure 5D***).

Effects on neuronal morphology *in vivo* during long-term expression of GCaMP versus GCaMP-X

Similar to chronic GCaMP-X imaging *in vitro*, a similar correlation has been expected between

oscillatory Ca^{2+} and neuronal morphology for live adult mice which may underlie GCaMP side-effects observed from *in vivo* imaging (***Figure 2*** and ***Figure 5***). Firstly, titrations of GCaMP viruses were applied to characterize the dose-dependent damage of neurons, for which the concentrations were at $1x10^{11}$, $5x10^{11}$ and $1x10^{12}$ v.g./ml for AAV-*Syn*-GCaMP6m, and $1x10^{12}$ v.g./ml for AAV-*Syn*-GCaMP6m-X_C, respectively. The viruses (30 nl) at the above concentrations were microinjected into different brain regions of the same mouse and then after three weeks the expression levels in brain slices were examined (***Figure 6A***). Low-concentration injection of virus at $1x10^{11}$ v.g./ml exhibited extremely sparse expression of GCaMP6m and yielded a low cell count. Correspondingly, the fluorescence signals were difficult to distinguish from the background, i.e., low contrast and SNR. The virus concentration, when increased to $5x10^{11}$ v.g./ml, resulted in a relatively larger number of healthy-looking cells expressing GCaMP6m. But the low image contrast still affected proper detection of Ca^{2+} signals due to neuropil fluorescence. High-expression levels of GCaMP (at the virus concentration of $1x10^{12}$ v.g./ml) significantly enhanced the fluorescence image contrast and greatly increased the numbers of GCaMP-positive cells. However, the majority of neurons exhibited severe nuclear accumulation, which would subsequently lead to aberrant Ca^{2+} dynamics and cell death (***Figure 6B***). In contrast, high-dose injection of GCaMP6m-X_C virus at $1x10^{12}$ v.g./ml was beneficial for image contrast and the number of positive and healthy cells; meanwhile, the N/C ratio remained within the low range as expected. Next, under the conditions similar to ***Figure 2*** and ***Figure 5***, we injected 60 nL GCaMP6m viruses of high dose ($1x10^{12}$ v.g./ml) and GCaMP6m-X_C viruses of ultrahigh dose ($1x10^{13}$ v.g./ml, 10-fold higher) to examine the temporal profile of damage in the same cortical region of S1BF (***Figure 6C***). At the checkpoints of 17-, 55-, 70- and 92-days post injection, neurons expressing GCaMP6m-X_C were compared with GCaMP6m. Confocal microscopy with brain slices revealed that the percentage of infected neurons and the expression level of GCaMP6m-X_C were close to their peaks on 17-days, suggesting that the ultrahigh dose could expedite GCaMP6m-X_C expression to reach the high level. Most importantly, long-term, high-level expression of GCaMP6m-X_C up to 92-days did not induce nuclear accumulation, whereas GCaMP6m at relatively lower concentration ($1x10^{12}$ v.g./ml) already caused severe nuclear accumulation evidenced from 17-days to 92-days (***Figure 6D***). Meanwhile, the soma

size of GCaMP6m-infected neurons was significantly smaller than that of GCaMP6m-X_C from 55-days to 92-days, presumably due to impaired spontaneous Ca^{2+} activities and related Ca^{2+} signals in these neurons. To directly confirm the relative expression levels, immunocytochemistry was performed on the brain slices infected by GCaMP6m and GCaMP6m-X_C, under similar conditions as in ***Figure 6C, D***. Long-term (13 weeks) expression levels of AAV-*Syn*-GCaMP6m (at the concentrations of $5x10^{11}$ v.g./ml and $1x10^{12}$ v.g./ml) in the brains of adult mice were quantified by anti-GFP immunofluorescence (***Figure 6—figure supplement 1***). And both dosages resulted in significantly lower expression levels than AAV-*Syn*-GCaMP6m-X_C of higher concentration ($1x10^{13}$ v.g./ml), excluding the expression level as the cause of less damage. Of note, the soma size of neurons after long-term GCaMP-X expression was larger than GCaMP, while indistinguishable from the blank control neurons. In summary, in comparison with GCaMP, GCaMP-X exhibited high compatibility with neurons as desired by chronic Ca^{2+} imaging.

Transgenic GCaMP mice may have similar neuronal toxicities

Although the drawbacks of GCaMP were noticed at the very beginning of its invention and then improved by mechanism-based rational-design later on, GCaMP transgenic mice have been considered to be relatively safe in comparison with viral delivery of GCaMP. Nevertheless, recent studies reported that some transgenic mouse lines, such as Ai93 and Ai148, suffered from epileptiform activities (Daigle et al., 2018; Steinmetz et al., 2017). Based on our data thus far mostly by way of transient transfection and viral infection, we suspected that the mechanisms of side-effects are likely applicable to transgenic expression of GCaMP. Following up this hypothesis, brain slice or culture neurons from transgenic mice were examined from both functional and morphological aspects.

Ai148 is a widely-used transgenic line, for which TIGRE2.0 has been utilized for GCaMP6f to enhance its expression level, such that the damage by GCaMP is potentially more pronounced (Daigle et al., 2018). Using confocal fluorescence microscopy, we examined GCaMP-expressing neurons from the layer II-III cortex of the 6-month old Rasgrf2-2A-dCre;Ai148D mice (with TMP-inducible expression of GCaMP6f) (***Figure 7A***). Nuclear accumulation of GCaMP was

readily discernible, although it was relatively less severe than long-term expression of viral GCaMP6m of high doses (***Figure 6***). Next, dissected from newborn Rasgrf2-2A-dCre;Ai148 mice, cortical neurons were cultured, and subsequently 10 μM TMP was added to induce GCaMP expression. Similar to viral delivery, transgenic neurons were also subject to GCaMP6f perturbations, especially in nucleus-filled neurons. Neurite tracings indicated that the complexity and length of neurites were reduced in Ai148 neurons as compared to GFP control neurons from DIV 21 onwards (***Figure 7C***). The temporal profile of total neurite length indicated that neurite outgrowth was significantly slowed down or even halted on DIV 14, in comparison with the control neurons (GFP virus-infected and TMP treated) (***Figure 7D***). Consistently, N/C ratio of GCaMP indicative of nuclear accumulation was gradually increased along with the expression time up to one month (***Figure 7E***). Functionally, Ca^{2+} waveforms of lower amplitude were acquired from Ai148 neurons expressing nucleus-filled GCaMP across the full month than the nucleus-excluded subgroup (***Figure 7F, G***), consistent with the previous results by GCaMP plasmids and viruses that the side-effects would be exacerbated by nuclear GCaMP. Similar results were obtained from analyzing the peak amplitude and integrated frequency of Ca^{2+} oscillations by comparing nucleus-filled versus nucleus-excluded subgroups of neurons on DIV 14 or later (***Figure 7H, I***). Another trial of neurite tracing and Ca^{2+} imaging with Ai148 neurons confirmed the effects and analyses described above (***Figure 7—figure supplement 1***).

Comparing with GFP control neurons from Ai140 mice, the potential effects of tTA (Moullan et al., 2015) were excluded from the major results and conclusions regarding GCaMP toxicities (***Figure 7—figure supplement 2***). Also, by adding TMP on DIV 14 to induce transgenic GCaMP6f expression at the mature stage, similar damage on neurite morphology and Ca^{2+} oscillation was observed from Ai148 neurons, consistent with the previous notions that both premature and mature neurons are subject to GCaMP perturbations (***Figure 7—figure supplement 3***). In addition to chemical-inducible expression of GCaMP, newborn Emx1-Cre;Ai148 mice were deployed to constitutively express GCaMP6f (***Figure 7—figure supplement 4***). GCaMP6f started to accumulate in the nucleus at very early stage indexed by N/C ratio (criteria of 0.8). The damage was clearly evidenced when compared with the control neurons virally expressing GCaMP6m-X_C. Meanwhile, the major characteristics of spontaneous

466 Ca^{2+} oscillation in transgenic neurons were also significantly altered, resulting in relatively lower
467 frequency, less synchronization, smaller amplitude, and abnormally wider FWHM.
468 In summary, the major findings by virus-infected neurons are applicable to transgenic mice,
469 where GCaMP expression is either TMP-inducible or constitutive. Morphological and functional
470 analyses strongly suggest that cortical neurons in transgenic GCaMP6 mice are also subject to
471 GCaMP toxicity similar to virus-infected neurons.
472

473 # Discussion

474 In this work, we applied GCaMP-X with reduced cell toxicity or enhanced neuron compatibility,
475 to monitor Ca^{2+} dynamics across multiple days/weeks both *in vitro* and *in vivo*. By way of
476 transient transfection, viral infection or transgenic expression, GCaMP of prolonged/excessive
477 expression caused neuronal toxicities presumably due to its perturbations on endogenous apoCaM
478 interactions, which were significantly reduced by rationally-designed GCaMP-X. By relieving
479 the concerns on the time and level of probe expression, GCaMP-X provides a simple solution for
480 chronic calcium imaging in alternative to circumventing GCaMP toxicity. GCaMP-X paves the
481 way to unexplored directions previously impeded or discouraged due to GCaMP perturbations.
482

483 **Available design solutions to avoid the side-effects of CaM-based GECI**

484 To better utilize CaM-based GECIs *in vitro and in vivo*, solutions with no or minimum side-effects
485 are in need. *In utero* electroporation and viral infection often result in high expression levels
486 particularly near the injection site, and some lines of transgenic mice using weaker promoters
487 could control probe expression within the low levels to alleviate nuclear accumulation (Akerboom
488 et al., 2012; Dana et al., 2019). Since probes present in the cytosol are able to bind
489 apoCaM-targets including Ca_V1 channels (Yang et al., 2018), neurons may still suffer from the
490 toxicity of the probes. Evidently, cytosolic GCaMP affected neural excitability in transgenic
491 mice expressing GCaMP5G or GCaMP6 (Steinmetz et al., 2017). To overcome these problems,
492 one solution is to substitute the core components of GECI design, e.g., to utilize troponin C from
493 muscle as a Ca^{2+}-binding motif (Mank et al., 2008). The TN-XXL has been claimed to be
494 suitable for chronic imaging potentially benefitted from its design basis (less likely to bind

endogenous proteins in neurons). However, the TN-XXL solution has at least two shortcomings. First, TNXXL is a FRET-based ratiometric sensor, of which the dynamic range is limited by FRET methods and indeed much narrower than GCaMP. Second, the Ca^{2+} binding motif from mammalian troponin C has the canonical EF-hands (resembling CaM), thus still possible to perturb neurons by binding endogenous targets at the apo states, which needs further investigations.

The approach adopted by this work is to introduce an additional protective motif that specifically binds apoCaM within the probe (***Figure 1A***). Such apoCaM binding motif (CBM) has been fused onto the N-terminus of conventional GCaMPs (from GCaMP3 to GCaMP7) to construct a new series of GCaMP-X correspondingly. When Ca^{2+} level is low, CBM successfully prevents apoCaM contained within GCaMP-X from interfering with Ca_V1 channels and other important apoCaM targets (***Figure 1—figure supplement 3***). Once Ca^{2+} concentration rises, M13 binds to Ca^{2+}/CaM with high affinity, without altering Ca^{2+}-sensing characteristics of GCaMP-X inherited from years of efforts and improvements. With GCaMP-X as the proof-of-principle, the design rules centered with apoCaM/Ca^{2+}-CaM binding are potentially applicable to CaM-based sensors or actuators of a broader scope (Grødem et al., 2021; Haiech et al., 2019), which may face similar challenges or problems to those associated with enhanced/prolonged expression of GCaMP.

Spontaneous Ca^{2+} activities in association with neural development and degeneration

While the membrane voltage is oscillating, cellular Ca^{2+} signals are also fluctuating, closely involved in neuronal development and circuit formation both *in intro* and *in vivo* (Kirkby et al., 2013; Sun et al., 2010). Meanwhile, in line with the aforementioned calcium hypothesis, dysregulated spontaneous Ca^{2+} activities would lead to defective morphology and functions of neurons, and eventually neural diseases (Harr and Distelhorst, 2010; Khan et al., 2020; Nicotera and Orrenius, 1998). In Ca^{2+} imaging experiments, Ca^{2+} fluorescence signals and electrical activities are often referred to each other since action potentials initiated by Na^+ channels would subsequently drive the fast opening of Ca^{2+} channels that mediate Ca^{2+} influx. Electrical recording via MEA (multiple electrode array) has been widely applied in long-term brain/neuron

monitoring (Obien and Frey, 2019; Shafer, 2019), among other methods. On the other hand, both membrane potentials and ion fluxes (Na^+ or Ca^{2+}) could have sophisticated mechanisms and specific consequences, e.g., Ca^{2+} oscillations of different forms: subthreshold oscillations by L-type Ca^{2+} channels, or intracellular Ca^{2+} fluctuations by intracellular Ca^{2+}-release channels (Chan et al., 2007; Uhlen and Fritz, 2010). GECIs are promising tools to overcome the limitations of many other methods including MEA, if the cell compatibility issues could be resolved as demonstrated by GCaMP-X in this work. GECI imaging methods directly and faithfully capture Ca^{2+} activities at different loci in the brain or within the cell, allowing high spatial-temporal resolution of concurrent morphological/functional imaging. Subcellular Ca^{2+} oscillations may be responsible for different aspects of neurogenesis and neuritogenesis, awaiting future investigations with organelle-specific GCaMP-X, such as the nuclear version GCaMP-X_N. Earlier Ca^{2+} activities (weak fluctuations of higher frequency) may represent spontaneous activity before synapse or network formation (Spitzer, 2006). At the later stage, synchronized Ca^{2+} oscillations (of lower frequency) emerge, along with dramatic changes in morphology and other aspects of development. Autonomous oscillations of SNc neurons are tightly coupled with $Ca_V1.3$ channels which may underpin Parkinson's disease or neural aging (Chan et al., 2007; Guzman et al., 2009). Cultured cortical slices and hiPSC-derived cortical neurons also suggest that L-type Ca^{2+} channels are crucial for both spontaneous Ca^{2+} activities and neuronal development (Horigane et al., 2020; Plumbly et al., 2019). A similar mechanism is likely shared by the correlation between spontaneous/oscillatory Ca^{2+} activities and neuronal morphology/development unveiled in this study. Expression, trafficking and functions of ion channels and membrane receptors are also subject to regulations by activities of different patterns (Ruffinatti et al., 2013; Spitzer, 2006; Toth et al., 2016), and chronic GECI imaging is expected to help elucidate these compound effects and mechanisms. In this work, we have particularly focused on spontaneous Ca^{2+} activities of cortical neurons in association with neuronal morphology both *in vitro* (***Figure 3*** and ***Figure 4***) and *in vivo* (***Figure 2***, ***Figure 5*** and ***Figure 6***), and in both neonatal (***Figure 3*** and ***Figure 4***) and mature neurons (***Figure 5—figure supplement 1*** and ***Figure7—figure supplement 3***), as the exemplars to demonstrate the performance of chronic GCaMP-X imaging. Importantly, since such Ca^{2+} activity-neuronal morphology

coupling was perturbed by GCaMP under various testing conditions, we are expecting a broad scope of applications awaiting GCaMP-X to explore both *in vitro* and *in vivo*.

Improved neuron-compatibility of GCaMP-X

GCaMP, as widely-applied GECI, has been evolved into its 8th version (Grødem et al., 2021), with enhanced sensitivity, brightness and kinetic properties tailored to specific imaging purposes, including single action potentials and activities in neuronal populations and microcompartments (Dana et al., 2019). However, the cytotoxicity of GCaMP has been a persistent problem from early on, mainly due to the fact that the CaM-centered schemes of GCaMP have been largely inherited across generations of its design (Akerboom et al., 2012; Chen et al., 2013; Dana et al., 2019; Nakai et al., 2001; Tallini et al., 2006; Tian et al., 2009). *In vivo* Ca^{2+} imaging with GCaMP viruses is facing the dilemma of safety versus reliability. On one hand, reducing GCaMP levels could alleviate or postpone the cytotoxicity, but low levels of expression would also reduce the contrast and SNR (Rose et al., 2014). On the other hand, increasing the expression level of GCaMP would enhance the data quality of Ca^{2+} imaging, but exacerbate the damage to neurons (Resendez et al., 2016). It is not surprising that GCaMP transgenic mice have encountered with similar problems. Several lines of GCaMP transgenic mice reported earlier, such as Emx1-Cre;Ai38 GCaMP3 transgenic mice, attempted to resolve the safety issue by restricting the expression to ultra-low levels (~5 μM) (Zariwala et al., 2012), but sacrificing the imaging quality (Rose et al., 2014). The mouse lines reported recently, such as Emx1-Cre;CaMK2α-tTA;Ai93 GCaMP6f transgenic mice and Slc17a7-IRES2-Cre;Ai148 GCaMP6f transgenic mice (Daigle et al., 2018; Madisen et al., 2015), managed to elevate the expression levels. However, epileptiform activities have been observed from these mice presumably due to GCaMP perturbations (Daigle et al., 2018; Steinmetz et al., 2017). One bypass solution is to conditionally induce GCaMP expression to conduct GCaMP imaging within a time window, which would be much less feasible for long-term expression and/or chronic imaging.

Instead, GCaMP-X allows long-term and high-level expression to increase the quality and reliability of Ca^{2+} imaging while reducing neuronal toxicities. For *in vitro* studies, investigations

of long-term Ca^{2+} dynamics are largely hindered by the cytotoxicity of GECIs or dyes (Rose et al., 2014; Smith et al., 2018). GCaMP-X is well suited for longitudinal Ca^{2+} dynamics, e.g., during neural development as in this study, for high-throughput screening of long-term drug effects (Vetter et al., 2020), or in other similar scenarios. For *in vivo* studies, due to the concerns known to GCaMP, false-negative or false-positive results by nuclear-filled GCaMP or under-expressed GCaMP are misleading especially in imaging large populations of neurons (Resendez et al., 2016). The existing reports have not yet reached an agreement regarding whether nuclear GCaMP would cause neuronal toxicities with a significant impact during the early post-injection phase, e.g., ***Figure 2*** and ***Figure 5***. Such discrepancy may reflect different doses of virus injection, different expression levels of GCaMP or even different types of neurons in different brain regions. Alternatively, it may still reinforce that neuronal damage could still exist even within OTW, as a precaution for selecting neurons and planning experiments. In this regard, GCaMP-X provides a viable option with higher SNR, more healthy neurons, lower neurotoxicity, prolonged expression/imaging and meanwhile less experimental complexity.

Additional control experiments would help evaluate how close GCaMP-X data are to the reality, considering potential Ca^{2+}-buffering effect intrinsic to Ca^{2+} probes and also other factors. Applicable controls were incorporated to better evaluate GCaMP-X data, e.g., Ai140 mice (GFP, ***Figure 7—figure supplement 2***) and Fluo-4 AM (Ca^{2+} dye, ***Figure 3—figure supplement 4***). The results have been encouraging in that GCaMP-X neurons were nearly indistinguishable in the morphological and functional aspects from Ai140 neurons expressing GFP or loaded with Fluo-4 AM. The feedbacks from GCaMP-X applications should continue to help clarify this matter in the future.

Methods

Key resources table

Reagent type (species) or resource	Designation	Source or reference	identifiers	Additional information

Strain, strain background (*Mus musculus*)	ICR			Produced by Tsinghua University & Beihang University
Strain, strain background (*Mus musculus*)	C57	Jackson Labs	C57BL/6J; stock no.000664	Produced by Tsinghua University
Strain, strain background (*Mus musculus*)	Ai148D	Jackson Labs	B6.Cg-Igs7tm148.1(tetO-GCaMP6f,CAG-tTA2)Hze/J; stock no.030328	
Strain, strain background (*Mus musculus*)	Rasgrf2-2A-dCre	Jackson Labs	B6;129S-Rasgrf2tm1(cre/folA)Hze/J; stock no.022864	
Strain, strain background (*Mus musculus*)	Ai140D	Jackson Labs	B6.Cg-Igs7tm140.1(tetO-EGFP,CAG-tTA2)Hze/J; stock no.030220	
Strain, strain background (*Mus musculus*)	Emx1-cre	Jackson Labs	B6.129S2-Emx1tm1(cre)Krj/J; stock no.005628	
cell line (*Homo-sapiens*)	Kidney (normal epithelial, embryo)	ATCC	HEK293	
antibody	anti-GFP antibody (Rabbit polyclonal)	Abcam	Cat#ab290; RIDD: AB_2313768	WB(1:1000); IF(1:200)
antibody	anti-GAPDH antibody (Rabbit polyclonal)	Gene-Protein Link	Cat#P01L081	WB(1:10000)
antibody	anti-Histone H3 antibody (Mouse monoclonal)	Beyotime	Cat#AF0009; RIDD: AB_2715593	WB(1:1000)
antibody	anti-Calmodulin 1/2/3 antibody (Rabbit monoclonal)	Abcam	Cat#ab45689; RIDD: AB_725815	WB(1:10000)
antibody	anti-His antibody (Rabbit	Gene-Protein Link	Cat#P01L071	WB(1:2000)

	monoclonal)			
antibody	HRP-conjugated Affinipure Goat Anti-Mouse IgG (H+L)	Proteintech	Cat#SA00001-1; RRID: AB_2722565	WB(1:10000)
antibody	HRP-conjugated Affinipure Goat Anti-Rabbit IgG (H+L)	Proteintech	Cat#SA00001-2; RRID: AB_2722564	WB(1:10000)
antibody	anti-NeuN antibody (Mouse monoclonal)	Millipore	Cat#MAB377; RRID: AB_2298772	IF(1:500)
antibody	anti-IgG Alexa Fluor 568 (Goat polyclonal)	Invitrogen	Cat#A11004; RRDI: AB_2534072	IF(1:800)
antibody	Anti-IgG Alexa Fluor 647 (Goat polyclonal)	Invitrogen	Cat#A21244; RRID: AB_2535812	IF(1:800)
chemical compound, drug	DAPI	Beyotime	2-(4-Amidinophenyl)-6-indolecarbamidine dihydrochloride; Cat#C1002	IF(1:1000)
chemical compound, drug	TMP	Sigma	Trimethoprim, Cat#T7883-5G	Dilute to DMSO
chemical compound, drug	Fluo-4 AM	Beyotime	Cat#S1060	
chemical compound, drug	Pluronic F-127	Beyotime	Cat#ST501-1g	
commercial assay or kit	Nuclear extraction kit	Abcam	Cat#113474	
software, algorithm	GraphPad Prism v8.0.1	GraphPad Software	RRID: SCR_002798	
software, algorithm	Imaris Viewer x64 v7.7.2	Oxford Instruments Group	RRID:SCR_007370	
software, algorithm	Fiji v6.6.1	National Institutes of Health	RRID:SCR_002285	

software, algorithm	Origin 2019b	OriginLab	RRID:SCR_014212	
software, algorithm	Clampex	Molecular Devices	RRID:SCR_011323	
software, algorithm	Matlab	MathWorks	RRID:SCR_001622	
recombinant DNA reagent	pGP-CMV-GCaMP6m (plasmid)	PMID: 23868258	Addgene 40754	
recombinant DNA reagent	pEGFP-N1-GCaMP6m-X_C (plasmid)	PMID: 29666364	Addgene 111543	
recombinant DNA reagent	pGP-CMV-jGCaMP7b (plasmid)	PMID: 31209382	Addgene 104484	
recombinant DNA reagent	pEGFP-N1-GCaMP7b-X_C (plasmid)	Created in this study	Addgene 178361	
recombinant DNA reagent	pEGFP-N1-GCaMP7b-X_N (plasmid)	Created in this study	Addgene 178362	
recombinant DNA reagent	pcDNA3-α_{1DL} (plasmid)	PMID: 35589958		To obtain the plasmid, please contact to Liu lab.
recombinant DNA reagent	pcDNA3-α_{1DL}-3x Flag (plasmid)	PMID: 35589958		To obtain the plasmid, please contact to Liu lab.
recombinant DNA reagent	pcDNA3-Flag-CaMBD_α_{1DL} (plasmid)	Created in this study		To obtain the plasmid, please contact to Liu lab.
recombinant DNA reagent	pcDNA3.1-YFP-Ng_S36A-Myc-HisA (plasmid)	Created in this study		To obtain the plasmid, please contact to Liu lab.
other	AAV2/DJ-*Syn*-GCaMP6m	Hanbio Biotechnology		
other	AAV2/DJ-*Syn*-GCaMP6m-X_C	Hanbio Biotechnology		

other	AAV2/DJ-*Syn*-jGCaMP7b	Hanbio Biotechnology		
other	AAV2/DJ-*Syn*-jGCaMP7b-X_C	Hanbio Biotechnology		
other	AAV2/DJ-*Syn*-ZsGreen	Hanbio Biotechnology		
other	pLenti-*Syn*-mCherry	OBiO Technology		
other	AAV2/9-*Syn*-GCaMP6m	BrainVTA		
other	AAV2/9-*Syn*-GCaMP6m-X_C	BrainVTA		

Molecular biology

GCaMP7b-X_C and GCaMP7b-X_N were constructed by replacing previously reported GCaMP6m-X_C or GCaMP6m-X_N (Yang et al., 2018) with appropriate PCR-amplified segments from jGCaMP7b via unique EcoRI and HindIII sites, or EcoRI and NotI sites, respectively. pcDNA3-Flag-CaMBD_α_{1DL} was generated by replacing YFP from pcDNA3-YFP-preIQ$_3$-IQ$_D$-PCRD$_D$ (Yang et al., 2022), with PCR-amplified Flag (DYKDDDDK) to by KpnI and NotI. pcDNA3.1-YFP-Ng_S36A-Myc-His was generated by inserting the PCR-amplified segments of neurogranin (NM_024140.2) containing S36A into a customized pcDNA3.1-MCS-Myc-His vector via unique EcoRI and HindIII sites.

Mice

Procedures involving animals have been approved by local institutional ethical committees (IACUC in Tsinghua University and Beihang University), similar to the previous protocol (Huber et al., 2012). *In vivo* experiments were conducted with adult mice (C57BL/6J, both male and female) of 2-6 months old. In total, 23 mice (C57BL/6J) were used for expression tests and functional tests (GCaMP6m and GCaMP6m-X_C). Three mice of Ai148D x Rasgrf2-2A-dCre (Jax #030328; Jax #022864) were used for brain-slice imaging to examine transgenic GCaM6f neurons. Expression of GCaMP6f in Ai148D x Rasgrf2-2A-dCre mice was induced with antibiotic Trimethoprim (TMP) by intraperitoneal injection with the dose of 0.25-0.5 mg/g *in vivo* (Sando et al., 2013). *In vitro* experiments were based on data from 82 mice (P0-P1, both male

and female). 52 ICR mice were used for expression and functional tests of Ca^{2+} indicators. Two newborn Ai148D x Emx1-Cre mice were used to persistently express GCaMP in cultured neurons. In the tests of cortical neurons expressing GCaMP6f from Ai148D x Rasgrf2-2A-dCre mice, 15 Ai148D x Rasgrf2-2A-dCre GCaMP6f positive mice were compared with 7 ICR control mice, 3 Ai140D x Rasgrf2-2A-dCre GFP positive mice and 2 Ai140D positive x Ragrf2-2A-dCre GFP negative mice. Expression of GCaMP6f or GFP was induced by directly adding 10 μM TMP into growth medium of cultured neurons after dissection.

Dissection and culturing of cortical neurons

Cortical neurons were dissected from newborn mice. Isolated tissues of cortex were digested with 0.25% trypsin for 15 min at 37 °C. Then digestion was terminated by DMEM supplemented with 10% FBS. The cell suspension was sieved through a filter and centrifuged at 1000 rpm for 5 min. The cell pellet was resuspended in DMEM supplemented with 10% FBS and were plated on poly-D-lysine-coated 35 mm No. 0 confocal dishes (In Vitro Scientific). After 4-6 hours, neurons were maintained in Neurobasal medium supplemented with 2% B27 and 1% glutaMAX-I (growth medium), and cultured in the incubator with temperature of 37 °C and 5% CO_2. Fresh growth medium was supplemented to neurons every 3-4 days to maintain the volume of 2 ml growth medium. All animals were obtained from the laboratory animal research center, Tsinghua University. Procedures involving animals has been approved by local institutional ethical committees (IACUC in Tsinghua University and Beihang University).

Virus infection on cultured neurons

All viruses for infection of cultured neurons were provided by Hanbio Biotechnology, China. The neuron broad-spectrum promoter *Syn* and AAV2/DJ serotypes were selected for neuro-specific expression of GFP, GCaMP or GCaMP-X in cultured cortical neurons. 1 μl $1x10^{12}$ v.g./ml of the desired kinds of viruses were added to growth medium on DIV 0 unless otherwise noted. The same batches of cortical neurons were simultaneously observed for comparison. The expression of GCaMP and GCaMP-X was detectable on DIV 3, reached the peak on DIV 7 and sustained the high-level up to one-month. All experiments *in vitro* were

repeated independently at least twice.

Ca^{2+} imaging with GCaMP or GCaMP-X in cultured cortical neurons

Ca^{2+} imaging of neurons expressing GCaMP or GCaMP-X was acquired by confocal microscopy (A1RMP, Nikon, Japan; Dragonfly 200, Andor, England). 488 nm laser was used for excitation. 35 mm confocal dish containing cultured cortical neurons was set in the live-cell imaging culture chamber of the confocal microscope to maintain the environment of 37°C, 5% CO_2 and 95% humidity. Sampling rate of images was at 1-5 Hz and 3-5 view fields were selected from each dish. Fluorescence intensity (F) was subtracted from its background. F_0 is the baseline fluorescence averaged from 5 data points at rest, and $\Delta F = F\text{-}F_0$. $\Delta F/F_0$ serves as the index for Ca^{2+} dynamics. Ca^{2+} waveforms were analyzed by the gadget of Quick Peaks in Origin software with the Three-Standard-Deviations Rule (values > 3 S.D.). On and off rate were characterized by the time to rise up or decay down to 50% of the maximum ($\Delta F/F_0$), respectively. And the full width at half maximum (FWHM) is defined as the duration of time between the (upward and downward) half-maximum timepoints. The mean of correlation coefficients based on Spearman Rank Correlation Coefficient in Origin software (Schaworonkow and Nikulin, 2019) was applied to quantify the degree of neuronal correlations based on all the traces of spontaneous Ca^{2+} signals per view (Sumi et al., 2020). FFT analyses were performed in Origin software. One-sided is selected for spectrum type and amplitude is define as below:

$$FFT\ Amplitude = 2\sqrt{Re^2 + Im^2}/n$$

Here Re and Im are the real and imaginary parts of FFT results, and n is the size of the input signal.

Neurite tracings were depicted with Imaris 7.7.2 from the images under average intensity projection. Analyses on neuronal morphology and Ca^{2+} oscillations were performed with at least 30 neurons at each time point in each independent experiment. Fluorescence intensities of Ca^{2+} dynamics in neurons were color-coded by Matlab (Mathworks) and Fiji.

Transfection, confocal fluorescence imaging and analysis of neurite morphology

2 μg of cDNA encoding jGCaMP7b, jGCaMP7b-X_C or jGCaMP7b-X_N and 1 μg cDNA encoding

CFP (for labelling the soma area and neurites) were transiently transfected into DIV 5-7 cultured cortical neurons by Lipofectamine 2000 (Invitrogen) with a typical protocol according to the manual. The opti-MEM containing plasmids and Lipofectamine 2000 was added to the Neurobasal medium for transfection. After 2 hours, neurons were maintained in Neurobasal medium supplemented with 2% B27, 1% glutaMAX-I for at least 2 days before analyzing neurite morphology.

Fluorescence imaging of cultured cortical neurons was performed on ZEISS Laser Scanning Confocal Microscope (LSM710, Carl Zeiss) and ZEN 2009 software. N/C ratio of GCaMP or GCaMP-X was calculated by the ratio of fluorescence intensity (nuclear/cytosolic). Measurement of the total length and *Sholl* analysis for neurites were performed with Imaris 7.7.2 (Bitplane). Only nonoverlapping neurons were selected for analysis and images of at least 24 neurons from two independent culture preparations were analyzed. Neurite tracings were depicted with Imaris 7.7.2 in CFP channel.

Craniotomy and *in vivo* virus injection

Wildtype mice were used for virus injection and craniotomy under isoflurane anesthesia (5% for induction, 1-1.5% during surgery). AAV2/9-*Syn*-GCaMP6m-X_C ($1.0x10^{13}$ v.g./ml, customized by BrainVTA, Wuhan, China) virus was tested in the primary somatosensory cortex (S1BF: AP -1.5, ML -3.0, DV 0.2/0.4), in comparison with AAV2/9-*Syn*-GCaMP6m ($1.0x10^{12}$ v.g./ml, BrainVTA, Wuhan, China) virus as a control.

Craniotomy was done three weeks after virus injection. A piece of skull above S1BF was removed to expose a square imaging window (~3 mm x 3 mm, centered on S1BF) and the cortex was protected by a hand-cut glass window using #1 coverglass. Then the glass window was fixed using adhesive (Krazy glue, Elmer's Products Inc) and dental cement. A head-post was also fixed to the posterior area of the mouse head using dental cement. 0.2 ml flunixin meglumine (0.25 mg/ml) was subcutaneously injected after surgery for 3 consecutive days.

Preparations of brain slices and image analysis

Mice were anaesthetized by intraperitoneal injection of avertin solution (250-500 mg/kg). Then they were transcardially perfused with phosphate buffer saline (PBS) followed by 4% PFA

(paraformaldehyde) solution. Brains were immersed in 4% PFA solution overnight and were embedded in 2.5% agarose gel for slicing operation. Slices were obtained using the Lecia vibratome (LeciaVT1200S) with proper parameters including depth, speed and thickness of the brain section (50, 70 or 100 μm). Contrast of image was estimated by the equation below:

$$Constast\ of\ image = 1 - \frac{2}{(F/F_{background} + 1)}$$

In vivo two-photon Ca^{2+} imaging

A 2-photon random access mesoscope controlled with ScanImage 2017 (Vidrio Technologies) was used for *in vivo* Ca^{2+} imaging (Pologruto et al., 2003; Sofroniew et al., 2016). Images (512x512 pixels, 600x600 or 300x300 μm^2) of L2/3 cells (150-250 μm under pia) in S1BF were collected at 7.4 Hz frame rate. Laser power (970 nm) was up to 60 mW out of objective. Calcium signal was extracted using CaImAn toolbox and data analysis was performed using Matlab (Giovannucci et al., 2019).

For functional test, imaging was carried out together with contralateral whisker stimulation using a 1.2 mm-diameter pole (~3 mm in amplitude, 10 vibrations in 0.5 s or 1 s for each trial). For each ROI, 20-40 trials were performed and calcium signaling was aligned to the onset of the whisker stimulation.

The fluorescence of each neuron was measured by averaging all pixels within the ROI (regions of interest) and corrected for neuropil contamination. The fluorescence signal was estimated by the equation below:

$$F_{cell}(t) = F_{measured}(t) - r * F_{neuropil}(t)$$

where r = 0.7 and $F_{neuropil}(t)$ was measured by averaging the fluorescence signal of all pixels within a 40 μm radium from the cell (Chen et al., 2013).

Signal-to-noise (SNR) was calculated as the ratio of F_{max}/F_0 to standard deviation of the filtered trace, 1 s period right before the whisker stimulate.

Whole-cell electrophysiology

HEK293 cells (ATCC) were cultured in 60 mm dishes and checked by PCR with primers 5'-GGCGAATGGGTGAGTAACACG -3' and 5'- CGGATAACGCTTGCGACCTATG -3' to ensure

743 free of mycoplasma contamination. Recombinant channels by α_{1DL}, β_{2a} (M80545) and $\alpha_2\delta$
744 (NM012919.2) subunits (4 μg of cDNA for each) were transiently transfected according to
745 established calcium phosphate protocol (Liu et al., 2017a; Liu et al., 2017b; Liu et al., 2010). To
746 enhance expression, cDNA for simian virus 40 T antigen (1 μg) was also co-transfected.
747 Additional 2 μg of cDNA of GCaMP7b or GCaMP7b-X_C was added as required in
748 co-transfections. Whole-cell recordings of transfected HEK293 cells were performed at room
749 temperature (25 °C) using an Axopatch 200B amplifier (Axon Instruments). The internal
750 solutions contained, (in mM): $CsMeSO_3$, 135; CsCl, 5; $MgCl_2$, 1; MgATP, 4; HEPES, 5; and
751 EGTA, 5; at 290 mOsm adjusted with glucose and at pH 7.3 adjusted with CsOH. The
752 extracellular solution contained (in mM): TEA-$MeSO_3$, 135; HEPES, 10; $CaCl_2$ or $BaCl_2$, 10; 300
753 mOsm, adjusted with glucose and at pH 7.3 adjusted with TEAOH. Whole-cell currents were
754 generated from a family of step depolarizations (-70 to +50 mV from a holding potential of -70
755 mV and step of 10 mV).
756
757 **Western blot**
758 HEK293 cells or cortical neurons were washed by PBS 3 times, followed by being lysed in lysis
759 buffer RIPA with protease inhibitor cocktail (Beyotime, P1006) for 20 min and centrifuged for
760 5min at 14,000 × g at 4 ℃. Loading buffer was added to the supernatant. Then the sample
761 were boiled for 7 min. Proteins were separated using 10% sodium dodecyl sulphate
762 polyacrylamide gel electrophoresis and transferred to a PVDF membrane for 90 min. Then
763 PVDF membrane was blocked in 5% non-fat dry milk and incubated with primary antibodies
764 overnight at 4 °C. Next, the PVDF membrane was washed three times with 1×TBST at room
765 temperature with shaking, and incubated with secondary antibodies for 1–2 hours at room
766 temperature then washed with 1×TBST for 3 times again. The membrane was coved with ECL
767 chemiluminescent liquid (beyotime, P0018FM) before detection with an enhanced
768 chemiluminescence system. Three or more independent replicates were performed for each
769 experiment. Cytoplasmic proteins were extracted using nuclear extraction kit (Abcam,
770 ab113474) following the instructions. Cytoplasmic proteins were collected by removing the
771 nuclear proteins extracted via the kit.

Co-Immunoprecipitation assay

HEK293 cells were transfected by Lipofectamine and cultured for 2 days before cell lysates were prepared by lysis buffer RIPA (with protease inhibitor cocktail, Beyotime, P1006) and centrifugation at 14,000×g for 5 min at 4 ℃. The supernatants were subjected to co-immunoprecipitation by using 20 μl anti-Flag or anti-Myc Magnetic Beads (Cat# B26102, B26301, bimake); and 5 mM EGTA overnight at 4 °C. Beads were washed with PBST for 3 times. Proteins were separated by sample loading buffer and boiled for 7 min. Then western blot was performed using the antibodies as indicated. Three or more independent replicates were performed for each experiment.

Immunofluorescence staining

For immunostaining of cultured cortical neurons: Cortical neurons were fixed with PBS + 4% PFA for 15 min at room temperature, and washed three times by PBS. Fixed neurons were permeabilized in PBS + 0.3% Triton X-100 for 10 min, blocked in the 10% goat serum in PBS for 60 min, and then incubated in primary antibodies + 10% goat serum + PBS overnight in 4℃. Next day, cells were washed 3 times by PBS with gentle shaking, incubated in PBS + secondary antibodies for 60 min, and then washed 3 times by PBS with gentle shaking.

For immunostaining of brain slices: Sections after slicing (50 μm thickness) were immersed in 0.3% PBST solution for 15 min and the solution was renewed every 5 min. Then, sections were blocked in blocking solution (0.3% PBST solution with 3% BSA) for 1 hour at room temperature and stained with primary antibodies at 4℃ for 36 hours. After washing 3 times by PBS, sections were incubated with secondary antibodies in turn for 60 min. Finally, sections were rinsed 3 times by PBS and prepared for visualization.

Fluorescence Ca^{2+} imaging with Fluo-4 AM

Neurons were loaded with 2 μM Fluo-4 AM and 0.05% (w/v) Pluronic F127 in neurobasal medium at 37°C for 20 min in dark. Then neurons were gently washed twice with preheated 1×PBS. Neurons were incubated with neurobasal medium for 10 min in dark. Fluo-4 AM was

excited at 488 nm, and emission signals were detected in 521 nm. Images were obtained using a 20× objective with 512 × 512 pixel.

Data analysis and statistics

Data were analyzed in Matlab, OriginPro and GraphPad software. Standard error of the mean (S.E.M.) and two-tailed Student's *t*-test or one-way ANOVA followed by Bonferroni for post hoc tests were calculated when applicable. Criteria of significance: *, $p<0.05$; **, $p<0.01$; ***, $p<0.001$; and *n.s.* denotes "not significant". All experiments were performed at least twice with appropriate sample sizes. Analyses of data were individually performed by at least 3 persons. Key experiments, such as the *in vivo* tests, were performed by one person, which were analyzed by other persons to avoid the potential bias.

Acknowledgements

We thank all X-Lab members for discussions and help. This work is supported by grants from Natural Science Foundation of China (NSFC 81971728, 21778034 and 11902021) and of Beijing (BNSF 7191006 and 5204037), China Postdoctoral Science Foundation (BX20180027 and 2018M641146), and open fund from Laboratory for Biomedical Engineering of Ministry of Education, Zhejiang University.

References

Akerboom, J., Chen, T.W., Wardill, T.J., Tian, L., Marvin, J.S., Mutlu, S., Calderon, N.C., Esposti, F., Borghuis, B.G., Sun, X.R., *et al.* (2012). Optimization of a GCaMP calcium indicator for neural activity imaging. J Neurosci *32*, 13819-13840.

Aoki, R., Tsubota, T., Goya, Y., and Benucci, A. (2017). An automated platform for high-throughput mouse behavior and physiology with voluntary head-fixation. Nat Commun *8*, 1196.

827 Aramuni, G., and Griesbeck, O. (2013). Chronic calcium imaging in neuronal development and
828 disease. Exp Neurol *242*, 50-56.

829 Ben-Johny, M., and Yue, D.T. (2014). Calmodulin regulation (calmodulation) of voltage-gated
830 calcium channels. J Gen Physiol *143*, 679-692.

831 Berridge, M.J. (2010). Calcium hypothesis of Alzheimer's disease. Pflügers Archiv - European
832 Journal of Physiology *459*, 441-449.

833 Berridge, M.J., Bootman, M.D., and Roderick, H.L. (2003). Calcium signalling: dynamics,
834 homeostasis and remodelling. Nat Rev Mol Cell Biol *4*, 517-529.

835 Chan, C.S., Guzman, J.N., Ilijic, E., Mercer, J.N., Rick, C., Tkatch, T., Meredith, G.E., and
836 Surmeier, D.J. (2007). 'Rejuvenation' protects neurons in mouse models of Parkinson's
837 disease. Nature *447*, 1081-1086.

838 Chen, T.-W., Wardill, T.J., Sun, Y., Pulver, S.R., Renninger, S.L., Baohan, A., Schreiter, E.R.,
839 Kerr, R.A., Orger, M.B., Jayaraman, V.*, et al.* (2013). Ultrasensitive fluorescent proteins for
840 imaging neuronal activity. Nature *499*, 295-300.

841 Couto, J., Musall, S., Sun, X.R., Khanal, A., Gluf, S., Saxena, S., Kinsella, I., Abe, T.,
842 Cunningham, J.P., Paninski, L.*, et al.* (2021). Chronic, cortex-wide imaging of specific cell
843 populations during behavior. Nat Protoc *16*, 3241-3263.

844 Daigle, T.L., Madisen, L., Hage, T.A., Valley, M.T., Knoblich, U., Larsen, R.S., Takeno, M.M.,
845 Huang, L., Gu, H., Larsen, R.*, et al.* (2018). A Suite of Transgenic Driver and Reporter Mouse
846 Lines with Enhanced Brain-Cell-Type Targeting and Functionality. Cell *174*, 465-480 e422.

847 Dana, H., Sun, Y., Mohar, B., Hulse, B.K., Kerlin, A.M., Hasseman, J.P., Tsegaye, G., Tsang,
848 A., Wong, A., Patel, R.*, et al.* (2019). High-performance calcium sensors for imaging activity in
849 neuronal populations and microcompartments. Nat Methods *16*, 649-657.

850 Dolmetsch, R.E., Xu, K., and Lewis, R.S. (1998). Calcium oscillations increase the efficiency
851 and specificity of gene expression. Nature *392*, 933-936.

852 Dutta, S., and Sengupta, P. (2016). Men and mice: Relating their ages. Life Sci *152*, 244-248.

853 Estrada, M., Uhlen, P., and Ehrlich, B.E. (2006). Ca2+ oscillations induced by testosterone
854 enhance neurite outgrowth. J Cell Sci *119*, 733-743.

855 Fernandez de Sevilla, D., Garduno, J., Galvan, E., and Buno, W. (2006). Calcium-activated
856 afterhyperpolarizations regulate synchronization and timing of epileptiform bursts in
857 hippocampal CA3 pyramidal neurons. J Neurophysiol *96*, 3028-3041.

858 Garcia, M.I., Chen, J.J., and Boehning, D. (2017). Genetically encoded calcium indicators for
859 studying long-term calcium dynamics during apoptosis. Cell Calcium *61*, 44-49.

860 Gerendasy, D.D., and Sutcliffe, J.G. (1997). RC3/neurogranin, a postsynaptic calpacitin for
861 setting the response threshold to calcium influxes. Mol Neurobiol *15*, 131-163.

862 Giovannucci, A., Friedrich, J., Gunn, P., Kalfon, J., Brown, B.L., Koay, S.A., Taxidis, J., Najafi,
863 F., Gauthier, J.L., Zhou, P.*, et al.* (2019). CaImAn an open source tool for scalable calcium
864 imaging data analysis. Elife *8*.

865 Gomez, T.M., and Zheng, J.Q. (2006). The molecular basis for calcium-dependent axon
866 pathfinding. Nat Rev Neurosci *7*, 115-125.

867 Grødem, S., Nymoen, I., Vatne, G.H., Björnsdottir, V., Lensjø, K.K., and Fyhn, M. (2021). An
868 updated suite of viral vectors for in vivo calcium imaging using local and
869 retro-orbital injections. bioRxiv, 2021.2005.2014.443815.

870 Guzman, J.N., Sanchez-Padilla, J., Chan, C.S., and Surmeier, D.J. (2009). Robust
871 pacemaking in substantia nigra dopaminergic neurons. J Neurosci *29*, 11011-11019.

872 Haiech, J., Moreau, M., Leclerc, C., and Kilhoffer, M.C. (2019). Facts and conjectures on
873 calmodulin and its cousin proteins, parvalbumin and troponin C. Biochim Biophys Acta Mol
874 Cell Res *1866*, 1046-1053.

875 Harr, M.W., and Distelhorst, C.W. (2010). Apoptosis and autophagy: decoding calcium signals
876 that mediate life or death. Cold Spring Harb Perspect Biol *2*, a005579.

877 Hong, G., and Lieber, C.M. (2019). Novel electrode technologies for neural recordings. Nat
878 Rev Neurosci *20*, 330-345.

879 Horigane, S.I., Hamada, S., Kamijo, S., Yamada, H., Yamasaki, M., Watanabe, M., Bito, H.,
880 Ohtsuka, T., and Takemoto-Kimura, S. (2020). Development of an L-type Ca(2+)
881 channel-dependent Ca(2+) transient during the radial migration of cortical excitatory neurons.
882 Neurosci Res.

883 Huber, D., Gutnisky, D.A., Peron, S., O'Connor, D.H., Wiegert, J.S., Tian, L., Oertner, T.G.,
884 Looger, L.L., and Svoboda, K. (2012). Multiple dynamic representations in the motor cortex
885 during sensorimotor learning. Nature *484*, 473-478.

886 Isaev, N.K., Genrikhs, E.E., Voronkov, D.N., Kapkaeva, M.R., and Stelmashook, E.V. (2018).

887 Streptozotocin toxicity in vitro depends on maturity of neurons. Toxicol Appl Pharmacol *348*,
888 99-104.

889 Ito, D., Tamate, H., Nagayama, M., Uchida, T., Kudoh, S.N., and Gohara, K. (2010). Minimum
890 neuron density for synchronized bursts in a rat cortical culture on multi-electrode arrays.
891 Neuroscience *171*, 50-61.

892 Kamijo, S., Ishii, Y., Horigane, S.I., Suzuki, K., Ohkura, M., Nakai, J., Fujii, H.,
893 Takemoto-Kimura, S., and Bito, H. (2018). A Critical Neurodevelopmental Role for L-Type
894 Voltage-Gated Calcium Channels in Neurite Extension and Radial Migration. J Neurosci *38*,
895 5551-5566.

896 Khan, T.A., Revah, O., Gordon, A., Yoon, S.J., Krawisz, A.K., Goold, C., Sun, Y., Kim, C.H.,
897 Tian, Y., Li, M.Y.*, et al.* (2020). Neuronal defects in a human cellular model of 22q11.2 deletion
898 syndrome. Nat Med *26*, 1888-1898.

899 Kirkby, L.A., Sack, G.S., Firl, A., and Feller, M.B. (2013). A Role for Correlated Spontaneous
900 Activity in the Assembly of Neural Circuits. Neuron *80*, 1129-1144.

901 Laviv, T., Scholl, B., Parra-Bueno, P., Foote, B., Zhang, C., Yan, L., Hayano, Y., Chu, J., and
902 Yasuda, R. (2020). In Vivo Imaging of the Coupling between Neuronal and CREB Activity in
903 the Mouse Brain. Neuron *105*, 799-812 e795.

904 Li, W., Llopis, J., Whitney, M., Zlokarnik, G., and Tsien, R.Y. (1998). Cell-permeant caged
905 InsP3 ester shows that Ca2+ spike frequency can optimize gene expression. Nature *392*,
906 936-941.

907 Liebscher, S., Keller, G.B., Goltstein, P.M., Bonhoeffer, T., and Hubener, M. (2016). Selective
908 Persistence of Sensorimotor Mismatch Signals in Visual Cortex of Behaving Alzheimer's
909 Disease Mice. Curr Biol *26*, 956-964.

910 Liu, N., Liu, Y., Yang, Y., and Liu, X. (2017a). Linker flexibility of IVS3-S4 loops modulates
911 voltage-dependent activation of L-type Ca2+ channels. Channels (Austin) *11*, 34-45.

912 Liu, N., Yang, Y., Ge, L., Liu, M., Colecraft, H.M., and Liu, X. (2017b). Cooperative and acute
913 inhibition by multiple C-terminal motifs of L-type Ca2+ channels. Elife *6*.

914 Liu, X., Yang, P.S., Yang, W., and Yue, D.T. (2010). Enzyme-inhibitor-like tuning of Ca(2+)
915 channel connectivity with calmodulin. Nature *463*, 968-972.

916 Luhmann, H., Sinning, A., Yang, J.-W., Reyes-Puerta, V., Stüttgen, M., Kirischuk, S., and
917 Werner, K. (2016). Spontaneous Neuronal Activity in Developing Neocortical Networks: From
918 Single Cells to Large-Scale Interactions. Frontiers in Neural Circuits *10*.

919 Madisen, L., Garner, A.R., Shimaoka, D., Chuong, A.S., Klapoetke, N.C., Li, L., van der Bourg,
920 A., Niino, Y., Egolf, L., Monetti, C.*, et al.* (2015). Transgenic mice for intersectional targeting of
921 neural sensors and effectors with high specificity and performance. Neuron *85*, 942-958.

922 Mank, M., Santos, A.F., Direnberger, S., Mrsic-Flogel, T.D., Hofer, S.B., Stein, V., Hendel, T.,
923 Reiff, D.F., Levelt, C., Borst, A.*, et al.* (2008). A genetically encoded calcium indicator for
924 chronic in vivo two-photon imaging. Nat Methods *5*, 805-811.

925 Mori, N., and Mook-Jung, I. (2015). Aging mechanisms: Longevity, metabolism, and brain
926 aging (Springer).

927 Moullan, N., Mouchiroud, L., Wang, X., Ryu, D., Williams, E.G., Mottis, A., Jovaisaite, V.,
928 Frochaux, M.V., Quiros, P.M., Deplancke, B.*, et al.* (2015). Tetracyclines Disturb Mitochondrial
929 Function across Eukaryotic Models: A Call for Caution in Biomedical Research. Cell Rep *10*,
930 1681-1691.

931 Mukai, Y., Shiina, T., and Jimbo, Y. (2010). Continuous monitoring of developmental activity
932 changes in cultured cortical networks. Electrical Engineering in Japan *145*, 28-37.

933 Murphy, T.H., Michelson, N.J., Boyd, J.D., Fong, T., Bolanos, L.A., Bierbrauer, D., Siu, T.,
934 Balbi, M., Bolanos, F., Vanni, M.*, et al.* (2020). Automated task training and longitudinal
935 monitoring of mouse mesoscale cortical circuits using home cages. Elife *9*.

936 Nakai, J., Ohkura, M., and Imoto, K. (2001). A high signal-to-noise Ca2+ probe composed of a
937 single green fluorescent protein. Nature Biotechnology *19*, 137-141.

938 Nicotera, P., and Orrenius, S. (1998). The role of calcium in apoptosis. Cell Calcium *23*,
939 173-180.

940 O'Banion, C.P., and Yasuda, R. (2020). Fluorescent sensors for neuronal signaling. Curr Opin
941 Neurobiol *63*, 31-41.

942 Obien, M.E.J., and Frey, U. (2019). Large-Scale, High-Resolution Microelectrode Arrays for
943 Interrogation of Neurons and Networks. Advances in neurobiology *22*, 83-123.

944 Opitz, T., De Lima, A.D., and Voigt, T. (2002). Spontaneous Development of Synchronous
945 Oscillatory Activity During Maturation of Cortical Networks In Vitro. Journal of Neurophysiology
946 *88*, 2196-2206.

947 Plumbly, W., Brandon, N., Deeb, T.Z., Hall, J., and Harwood, A.J. (2019). L-type voltage-gated
948 calcium channel regulation of in vitro human cortical neuronal networks. Sci Rep *9*, 13810.

949 Pologruto, T.A., Sabatini, B.L., and Svoboda, K. (2003). ScanImage: Flexible software for
950 operating laser scanning microscopes. Biomedical Engineering Online *2*, 9.

951 Resendez, S.L., Jennings, J.H., Ung, R.L., Namboodiri, V.M., Zhou, Z.C., Otis, J.M., Nomura,
952 H., McHenry, J.A., Kosyk, O., and Stuber, G.D. (2016). Visualization of cortical, subcortical
953 and deep brain neural circuit dynamics during naturalistic mammalian behavior with
954 head-mounted microscopes and chronically implanted lenses. Nat Protoc *11*, 566-597.

955 Rose, T., Goltstein, P.M., Portugues, R., and Griesbeck, O. (2014). Putting a finishing touch on
956 GECIs. Front Mol Neurosci *7*, 88.

957 Rosenberg, S.S., and Spitzer, N.C. (2011). Calcium signaling in neuronal development. Cold
958 Spring Harb Perspect Biol *3*, a004259.

959 Ruffinatti, F.A., Gilardino, A., Lovisolo, D., and Ferraro, M. (2013). Spatial wavelet analysis of
960 calcium oscillations in developing neurons. PLoS One *8*, e75986.

961 Sando, R., 3rd, Baumgaertel, K., Pieraut, S., Torabi-Rander, N., Wandless, T.J., Mayford, M.,
962 and Maximov, A. (2013). Inducible control of gene expression with destabilized Cre. Nat
963 Methods *10*, 1085-1088.

964 Schaworonkow, N., and Nikulin, V.V. (2019). Spatial neuronal synchronization and the
965 waveform of oscillations: Implications for EEG and MEG. PLoS Comput Biol *15*, e1007055.

966 Shafer, T.J. (2019). Application of Microelectrode Array Approaches to Neurotoxicity Testing

967 and Screening. Advances in neurobiology *22*, 275-297.

968 Smith, N.A., Kress, B.T., Lu, Y., Chandler-Militello, D., Benraiss, A., and Nedergaard, M.
969 (2018). Fluorescent Ca(2+) indicators directly inhibit the Na,K-ATPase and disrupt cellular
970 functions. Sci Signal *11*.

971 Sofroniew, N.J., Flickinger, D., King, J., and Svoboda, K. (2016). A large field of view
972 two-photon mesoscope with subcellular resolution for in vivo imaging. Elife *5*.

973 Spitzer, N.C. (2006). Electrical activity in early neuronal development. Nature *444*, 707-712.

974 Steinmetz, N.A., Buetfering, C., Lecoq, J., Lee, C.R., Peters, A.J., Jacobs, E.A.K., Coen, P.,
975 Ollerenshaw, D.R., Valley, M.T., de Vries, S.E.J.*, et al.* (2017). Aberrant Cortical Activity in
976 Multiple GCaMP6-Expressing Transgenic Mouse Lines. eNeuro *4*, ENEURO.0207-0217.2017.

977 Sumi, T., Yamamoto, H., and Hirano-Iwata, A. (2020). Suppression of hypersynchronous
978 network activity in cultured cortical neurons using an ultrasoft silicone scaffold. Soft Matter *16*,
979 3195-3202.

980 Sun, J.J., Kilb, W., and Luhmann, H.J. (2010). Self-organization of repetitive spike patterns in
981 developing neuronal networks in vitro. European Journal of Neuroence *32*, 1289-1299.

982 Takahashi, N., Oertner, T.G., Hegemann, P., and Larkum, M.E. (2016). Active cortical
983 dendrites modulate perception. Science *354*, 1587-1590.

984 Tallini, Y.N., Ohkura, M., Choi, B.R., Ji, G., Imoto, K., Doran, R., Lee, J., Plan, P., Wilson, J.,
985 Xin, H.B.*, et al.* (2006). Imaging cellular signals in the heart in vivo: Cardiac expression of the
986 high-signal Ca2+ indicator GCaMP2. Proceedings of the National Academy of Sciences *103*,

4753-4758.

Tian, L., Hires, S.A., Mao, T., Huber, D., Chiappe, M.E., Chalasani, S.H., Petreanu, L., Akerboom, J., McKinney, S.A., Schreiter, E.R.*, et al.* (2009). Imaging neural activity in worms, flies and mice with improved GCaMP calcium indicators. Nature Methods *6*, 875-881.

Toth, A.B., Shum, A.K., and Prakriya, M. (2016). Regulation of neurogenesis by calcium signaling. Cell Calcium *59*, 124-134.

Uhlen, P., and Fritz, N. (2010). Biochemistry of calcium oscillations. Biochem Biophys Res Commun *396*, 28-32.

Van, P.J., Wolters, P.S., Corner, M.A., Rutten, W.L., and Ramakers, G.J. (2004). Long-Term Characterization of Firing Dynamics of Spontaneous Bursts in Cultured Neural Networks. Biomedical Engineering IEEE Transactions on *51*, 2051-2062.

Vetter, I., Carter, D., Bassett, J., Deuis, J.R., Tay, B., Jami, S., and Robinson, S.D. (2020). High-Throughput Fluorescence Assays for Ion Channels and GPCRs. In Calcium Signaling, 2nd Edition, M.S. Islam, ed. (Cham: Springer International Publishing Ag), pp. 27-72.

Yang, Y., Liu, N., He, Y., Liu, Y., Ge, L., Zou, L., Song, S., Xiong, W., and Liu, X. (2018). Improved calcium sensor GCaMP-X overcomes the calcium channel perturbations induced by the calmodulin in GCaMP. Nat Commun *9*, 1504.

Yang, Y., Yu, Z., Geng, J., Liu, M., Liu, N., Li, P., Hong, W., Yue, S., Jiang, H., Ge, H.*, et al.* (2022). Cytosolic peptides encoding CaV1 C-termini downregulate the calcium channel activity-neuritogenesis coupling. Commun Biol *5*, 484.

1007 Zariwala, H.A., Borghuis, B.G., Hoogland, T.M., Madisen, L., Tian, L., De Zeeuw, C.I., Zeng,
1008 H., Looger, L.L., Svoboda, K., and Chen, T.W. (2012). A Cre-Dependent GCaMP3 Reporter
1009 Mouse for Neuronal Imaging In Vivo. Journal of Neuroscience *32*, 3131-3141.

1010 Zhang, Y., Rózsa, M., Liang, Y., Bushey, D., Wei, Z., Zheng, J., Reep, D., Broussard, G.J.,
1011 Tsang, A., Tsegaye, G.*, et al.* (2021). Fast and sensitive GCaMP calcium indicators for
1012 imaging neural populations. bioRxiv, 2021.2011.2008.467793.

1013

1014

FIGURE LEGENDS

Figure 1. The design principles applicable to jGCaMP7 and jGCaMP7-X. (**A**) Cultured cortical neurons from newborn mice were transiently transfected with YFP, jGCaMP7b, jGCaMP7b-X_C or jGCaMP7b-X_N, respectively on DIV 5-7, then imaged by confocal microscopy on DIV 7-9. As illustrated, apoCaM binding motif (CBM) was fused onto N-terminus of GCaMP and the tags of localization signals (nuclear export signal or nuclear localization signal, NES/NLS) were fused to the C-terminus of GCaMP to construct GCaMP-X_C or GCaMP-X_N, respectively. Neurite tracing and subcellular GCaMP distributions are shown below. (**B**) N/C ratio of jGCaMP7b or jGCaMP7b-X_C in neurons, by calculating the nucleus versus cytosol ratio of fluorescence intensities. (**C** and **D**) Total length (**C**) and *Sholl* analysis (**D**) for cortical neurons expressing YFP or GCaMP variants. Two independent experiments from 2 independent culture preparations (**A-D**). (**E**) Electrophysiological validations of jGCaMP7b versus jGCaMP7b-X with recombinant $Ca_V1.3$ channels. Full-length $Ca_V1.3$ channels (α_{1DL}) were expressed in HEK293 cells alone (left) or with jCaMP7b (middle) or with jGCaMP7b-X_C (right). At -10 mV, Ca^{2+} current traces (red, with scale bars indicating current amplitudes) and Ba^{2+} current traces (gray, rescaled) are shown. S_{Ca} and I_{Ca} (quantified by the equations shown in the first column) are the indices of calcium dependent inactivation and voltage dependent activation, respectively. Cell numbers are indicated in the parentheses right after the values.

Standard error of the mean (S.E.M) and two-tailed unpaired Student's *t*-test (**B**) or one-way ANOVA followed by Bonferroni for post hoc tests (**C** and **E**) (criteria of significance: * $p<0.05$; ** $p<0.01$; *** $p<0.001$; *n.s.* denotes "not significant") were applied.

Figure 2. *In vivo* Ca^{2+} imaging of sensory-evoked responses in cortical neurons virally infected with GCaMP-X versus GCaMP. (**A**) Ca^{2+} dynamics of GCaMP6m and GCaMP6m-X_C in S1 primary somatosensory cortex under whisker stimulation by *in vivo*

two-photon Ca^{2+} imaging. 4-6 weeks and 10-13 weeks post injection were considered as optimal time window (OTW) or beyond OTW, respectively. The orange and blue circles in the representative two-photon images indicate nucleus-filled and nucleus-excluded GCaMP6m, respectively. The colored scale bar indicates the fluorescence intensity of Ca^{2+} probes. Multiple trials of the same neuron are shown for nucleus-filled GCaMP6m, nucleus-excluded GCaMP6m, or GCaMP6m-X_C. The averaged Ca^{2+} responses are shown at the bottom. (**B**) Subcellular distributions of GCaMP6m and GCaMP6m-X_C *in vivo* within OTW or beyond OTW. Neurons were divided into two distinct subgroups, nucleus-excluded and nucleus-filled, by applying the cut-off value (N/C ratio) of 0.8. (**C**) Responses to repetitive whisker stimuli were evaluated and compared for GCaMP6m nucleus-filled neurons, total GCaMP6m neurons and GCaMP6m-X_C. The average amplitude ($\Delta F/F_0$) (left), success rate of the trials (middle) and SNR (right) during whisker stimuli were compared. Data were obtained from 5 or 4 mice for GCaMP6m and GCaMP6m-X_C, respectively. Standard error of the mean (S.E.M) and one-way ANOVA followed by Bonferroni for post hoc tests (criteria of significance: * $p<0.05$; ** $p<0.01$; *** $p<0.001$) were calculated when applicable.

Figure 3. Chronic Ca^{2+} fluorescence imaging for autonomous Ca^{2+} oscillations in cultured cortical neurons. (**A**) Time-lapse images of cultured cortical neurons infected with AAV-*Syn*-GCaMP6m or AAV-*Syn*-GCaMP6m-X_C. Spontaneous Ca^{2+} activities by the two probes are shown for DIV 10 and DIV 28. See ***Figure 3—video 1, 2*** and ***3*** for details. Ca^{2+} signals (color-coded) were monitored by the confocal microscope with a live-cell imaging chamber to maintain the cell culture conditions (37ºC, 5% CO_2, 97-100% humidity) at different timepoints. (**B**) Representative traces of Ca^{2+} activities in cultured cortical neurons expressing GCaMP6m (upper) or GCaMP-X_C (lower) from DIV 3 to DIV 28. (**C-F**) Temporal profiles of key indices measured from spontaneous Ca^{2+}, including the average frequency (10^{-3} Hz or mHz, **C**) and peak amplitude ($\Delta F/F_0$, **D**); synchrony (quantified by the mean of correlation coefficient per view, **E**), and full width at half maximum (FWHM, **F**).

(**G**) Power spectral analyses by FFT (Fast Fourier Transformation) for Ca^{2+} traces of cortical neurons from DIV 3 to DIV 28. (**H**) Frequency components in percentage. By integrating the absolute amplitudes over each frequency band (**G**), three major bands are shown: <10 mHz (ultra-slow), 10-100 mHz (slow) and 100-300 mHz (fast), where the 10-100 mHz band indicates the major component. (**I**) Summary over 3 independent experiments with 3 independent culture preparations (see ***Figure 3—figure supplement 2*** for the other two experiments). Key indices of frequency (DIV 35), $\Delta F/F_0$ (DIV 28), correlation coefficient per view (DIV 28) and FWHM (DIV 28) were calculated and compared for GCaMP6m versus GCaMP6m-X_C.

Standard error of the mean (S.E.M) and the Student's *t*-test (two-tailed unpaired with criteria of significance: * $p<0.05$; ** $p<0.01$; *** $p<0.001$) were calculated when applicable.

Figure 4. The correlations between neuronal development and Ca^{2+} oscillations unveiled by GCaMP-X. (**A**) Time-lapse images with neurite tracing for cultured cortical neurons expressing GCaMP6m (upper two rows) or GCaMP6m-X_C (lower two rows). Enlarged fluorescence images are to show subcellular distributions of the probes, indicative of the nuclear accumulation of GCaMP6m versus GCaMP6m-X_C. (**B**) Temporal profiles of total neurite length per view (red) or soma size per neuron (pink) for neurons expressing GCaMP6m. (**C**) Temporal profiles of total neurite length per view (red) or soma size per neuron (pink) for neurons expressing GCaMP6m-X_C. (**D**) The temporal profiles of the average frequency of Ca^{2+} oscillations (blue) and the peak amplitude ($\Delta F/F_0$, green), adopted from ***Figure 3C*** and ***Figure 3D***. (**E**) Temporal profiles of the growth rates (μm/day) of neurite length (orange) or soma size (purple), respectively. Analyses were performed in parallel on both Ca^{2+} waveforms and neuronal morphology based on the data obtained from the same 3 independent culture preparations as in ***Figure 3*** (see ***Figure 4—figure supplement 1*** for details on morphology data).

Standard error of the mean (S.E.M) was calculated when applicable.

Figure 5. Chronic Ca^{2+} imaging for spontaneous Ca^{2+} activities *in vivo*. (**A** and **B**) *In vivo* two-photon fluorescence images (**A**) and spontaneous nuclear Ca^{2+} activities (**B**) of virus-infected neurons in S1 primary somatosensory cortex. Neurons expressing GCaMP6m-X_C or GCaMP6m (nucleus-filled and nucleus-excluded) within OTW (optimal time window, 4-8 weeks post injection) and beyond OTW (8-11 weeks post injection) were analyzed and compared. (**C**) N/C ratio summary of GCaMP6m and GCaMP6m-X_C *in vivo* beyond OTW. Neurons were divided into two groups: nucleus-excluded and nucleus-filled, by applying the criteria of N/C ratio (0.8). (**D**) Key parameters of spontaneous Ca^{2+} activities.

Standard error of the mean (S.E.M) and two-tailed unpaired Student's *t*-test (**C**) or one-way ANOVA followed by Bonferroni for post hoc tests (**D**) (criteria of significance: * $p<0.05$; ** $p<0.01$; *** $p<0.001$) were calculated when applicable.

Data were obtained from 3 or 2 mice for GCaMP6m and GCaMP6m-X_C, respectively.

Figure 6. Evaluation of neuronal morphology for long-term *in vivo* expression of GCaMP-X versus GCaMP. (**A**) Confocal brain-slice images for ALM (anterolateral motor cortex) or S1 (primary somatosensory cortex). For the same mouse, AAV-*Syn*-GCaMP6m or AAV-*Syn*-GCaMP6m-X_C (30 nl) of the indicated titers were injected into the left or right brain. Brain slices were dissected 3 weeks after virus injection. (**B**) N/C ratio (upper) and contrast of images (lower), summarized over 3 mice. (**C**) Confocal images of brain slices expressing

GCaMP6m or GCaMP6m-X_C acquired at different timepoints up to 92 days post virus injection. AAV-*Syn*-GCaMP6m or AAV-*Syn*-GCaMP6m-X_C (60 nl) viruses of the indicated titers were microinjected into the left or right S1BF (barrel field of S1) of the same mouse, respectively. (**D**) Summary of N/C ratio (left) and soma size (right) for the neurons expressing GCaMP6m or GCaMP6m-X_C (8 mice in total). Standard error of the mean (S.E.M) and one-way ANOVA followed by Bonferroni for post hoc tests (criteria of significance: * $p<0.05$; ** $p<0.01$; *** $p<0.001$) were calculated when applicable.

Figure 7. Chronic imaging for cultured cortical neurons of GCaMP transgenic mice. (**A**) Confocal brain-slice images of cortex layer II-III from 6-month old GCaMP6f-positive transgenic mice (Rasgrf2-2A-dCre x Ai148 mice). GCaMP6f was examined ~4 weeks after induction of expression by intraperitoneal injection of TMP. (**B**) The N/C ratio of layer II-III neurons of adult Ai148 mice. (**C**) Neurite growth of cultured cortical neurons from newborn Ai148 mice. Neurite tracing for GCaMP-positive neurons (upper two rows) versus GCaMP-negative neurons (infected by GFP virus, bottom row), both added with 10 μM TMP to induce transgene expression. Zoomed confocal images illustrate subcellular distributions of GCaMP (middle row). (**D** and **E**) Temporal profiles of total neurite length (**D**) or N/C ratio (**E**) for GCaMP-expressing Ai148 neurons, in comparison with GCaMP-negative GFP-infected neurons. (**F**) Time-laps images of single-neuron Ca^{2+} dynamics on DIV 28 from the nucleus-excluded and nucleus-filled subgroups. Color coding indicates fluorescence intensity. (**G**) Spontaneous Ca^{2+} activities of GCaMP-positive neurons in the nuclear-excluded and nuclear-filled subgroups from DIV 4 to DIV 28. (**H** and **I**) Temporal profiles of the peak amplitudes ($\Delta F/F_0$, **H**) and the integrated amplitudes (over the frequency band of 10-100 mHz, **I**) for Ai148 neurons, compared with GCaMP-X_C.

Data were based on 3 Ai148 mice (**A** and **B**), and 2 independent experiments from 2 independent culture preparations (**C-I**). Standard error of the mean (S.E.M) and two-tailed

unpaired Student's *t*-test (**D**) (criteria of significance: * $p<0.05$; ** $p<0.01$; *** $p<0.001$) were calculated when applicable.

SUPPLEMENTAL FIGURE LEGENDS

Figure 1—figure supplement 1. Expression levels of indicators in HEK293 cells. (**A-D**) jGCaMP7b, jGCaMP7b-X_C and jGCaMP7b-X_N were transiently transfected into HEK293 cells to examine the level of protein expression by western blot. Whole cell extracts (**A** and **B**) and cytosolic extracts (**C** and **D**) were separately examined. The anti-GFP bands and anti-GAPDH bands indicate the expression levels and the amount of inputs, respectively. The anti-Histone H3 bands served as the nuclear marker to confirm the efficacy of the fractionation. The relative expression levels were normalized to the jGCaMP7b control for the whole cell (**B**) or cytosol (**D**) proteins. (**E-G**) Comparison of protein expression of indicators in HEK293 cells by immunostaining. HEK cells expressing jGCaMP7b, jGCaMP7b-X_C and jGCaMP7b-X_N were stained with anti-GFP (red channel) and DAPI (blue channel) to measure the level of expression and illustrate the nuclear envelop, respectively. Confocal images in GFP channels indicate GCaMP fluorescence. The anti-GFP signals were normalized over jGCaMP7b to compare the expression levels. The cytosolic and nuclear levels of jGCaMP7b were compared with jGCaMP7b-X_C (**F**) and jGCaMP7b-X_N (**G**), respectively. (**H** and **I**) HEK293 cells expressing jGCaMP7b or jGCaMP7b-X_C were stimulated by 2.5 μM ionomycin (a potent calcium ionophore) to saturate the indicators (**H**). Indexed by cytosolic fluorescence intensity, the two indicators were compared at the basal or saturated state (**I**), suggesting that it is possible to use probe fluorescence to estimate the expression level if the conditions are carefully controlled.

3 independent experiments from 3 independent samples.

Standard error of the mean (S.E.M) and one-way ANOVA followed by Bonferroni for post hoc tests (**B**) or two-tailed unpaired Student's *t*-test (**D**, **F**, **G**, **I**) (criteria of significance: * $p<0.05$, ** $p<0.01$, *** $p<0.001$; *n.s.* represents "not significant") were applied.

Figure 1—figure supplement 2. Expression levels of indicators in cultured cortical neurons. (**A-C**) The indicators of jGCaMP7b, jGCaMP7b-X_C and jGCaMP7b-X_N expressed in cultured cortical neurons were examined by immunostaining. Similar to HEK293 cells,

cultured cortical neurons from newborn mice transiently-transfected by jGCaMP7b, jGCaMP7b-X_C or jGCaMP7b-X_N were stained by anti-GFP (red channel) and DAPI (blue channel) to measure the protein expression and illustrate the nuclear envelop, respectively. Confocal images in GFP channels pointed out the positive neurons. The anti-GFP signals were normalized over the jGCaMP7b groups. The cytosolic and nuclear levels of jGCaMP7b were compared with jGCaMP7b-X_C (**B**) and jGCaMP7b-X_N (**C**), respectively. (**D** and **E**) Cortical neurons expressing jGCaMP7b or jGCaMP7b-X_C were stimulated by 2.5 μM ionomycin (**D**). Indexed by cytosolic fluorescence intensity, the two indicators were compared at the basal or saturated state (**E**). (**F-H**) jGCaMP7b-X_C and jGCaMP7b-X_N were co-transfected into cortical neurons to compare with jGCaMP7b. Cultured cortical neurons expressing YFP served as the control. Anti-GFP and DAPI fluorescence images indicate the protein expression and the nuclear envelop, respectively (**F**). The total length of neurites was calculated and compared for the three groups of neurons (**G**). Indexed by normalized anti-GFP intensity (over jGCaMP7b) cells co-expressing jGCaMP7b-X_C and jGCaMP7b-X_N resulted in an even higher level of probe expression than jGCaMP7b.

3 independent experiments from 3 independent culture preparations.

Standard error of the mean (S.E.M) and two-tailed unpaired Student's *t*-test (**B, C, E, H**) or one-way ANOVA followed by Bonferroni for post hoc tests (**G**) (criteria of significance: * $p<0.05$, ** $p<0.01$, *** $p<0.001$; *n.s.* represents "not significant") were applied.

Figure 1—figure supplement 3. Differential interactions of GCaMP versus GCaMP-X with apoCaM-binding proteins. Coimmunoprecipitation results of His-tagged GCaMP or GCaMP-X_C with Flag-tagged apoCaM binding domain of α_{1DL} (CaMBD_α_{1DL}) **(A)**, or with Myc- and His-tagged Ng_S36A (**B**). HEK293 cell lysates were added with 5 mM EGTA; n = 3 replicates.

Figure 3—figure supplement 1. Spectral analysis for Ca^{2+} waveforms acquired by GCaMP-X.

(**A**) Representative FFT-based power spectra of individual neurons at different timepoints (DIV). Neurons from DIV 3 to DIV 10 exhibited low FFT amplitudes, whereas neurons from DIV 21 to DIV 28 showed significantly large amplitudes with the central frequency around 10-100 mHz. DIV 17 appeared to be the transition time for neurons to develop from weak oscillations (DIV 3 to DIV 10) to strong oscillations (DIV 21 to DIV 28). (**B**) Temporal profiles for the major frequency components of Ca^{2+} oscillations. Three frequency components including 100-300 mHz (fast), 10-100 mHz (slow) and <10 mHz (ultraslow) were summarized (n=3 individual experiments). Frequency components were evaluated by the amplitude integration over each frequency band in FFT spectra.

Figure 3—supplement 2. Ca^{2+} oscillations in long-term cultured cortical neurons expressing GCaMP6m or GCaMP6m-X_C *in vitro*. (**A-C**) Ca^{2+} activities in cultured cortical neurons expressing GCaMP6m (black) or GCaMP6m-X_C (red), respectively. Exemplar traces from DIV 3 to DIV 42 (**A**), summarized by peak amplitudes ($\Delta F/F_0$, **B**) and full width at half maximum (FWHM, **C**). Note that GCaMP6m on DIV 42 did not record any noticeable response. (**D-F**) Another set of Ca^{2+} oscillation data and analyses over multiple weeks similar to (**A-C**). Standard error of the mean (S.E.M) and Student's *t*-test (two-tailed unpaired with criteria of significance: * $p<0.05$, ** $p<0.01$, *** $p<0.001$) were calculated when applicable.

Figure 3—figure supplement 3. Ca^{2+} oscillations in cultured cortical neurons expressing jGCaMP7b or jGCaMP7b-X_C. (**A**) Representative Ca^{2+} fluorescence images (color-coded) of cultured cortical neurons expressing jGCaMP7b or jGCaMP7b-X_C on DIV 7 or DIV 35.

(**B**) Representative Ca^{2+} activity traces of cultured cortical neurons expressing jGCaMP7b (black) or jGCaMP7b-X_C (red) across 5 weeks (from DIV 7 to DIV 35). (**C**) Summarized peak amplitudes in time-dependent profiles ($\Delta F/F_0$).

3 independent experiments from 3 independent culture preparations.

Standard error of the mean (S.E.M) and Student's *t*-test (two-tailed unpaired with criteria of significance: * $p<0.05$, ** $p<0.01$, *** $p<0.001$) were calculated when applicable.

Figure 3—figure supplement 4. Ca^{2+} oscillations in cultured cortical neurons imaged by Fluo-4 AM. (**A**) Ca^{2+} signals of cultured cortical neurons on DIV 21. Neurons were infected with pLenti-*Syn*-mCherry virus to illustrate the cell body (left). Ca^{2+} fluorescence intensities from neurons loaded with Fluo-4 AM were color-coded (middle). A trace of Fluo-4 AM fluorescence represents the Ca^{2+} signals in a neuron (right). **(B-E)** Summary of the key indices: FWHM (in sec, **B**), on rate (in sec, **C**), off rate (in sec, **D**) and SNR (**E**) of Ca^{2+} signals acquired by jGCaMP7b, jGCaMP7b-X_C or Fluo-4 AM. (**F**) Temporal profiles of FWHM measured from spontaneous Ca^{2+} oscillations acquired by GCaMP6m, GCaMP6m-X_C or Fluo-4 AM.

Standard error of the mean (S.E.M) and one-way ANOVA followed by Bonferroni for post hoc tests (criteria of significance: * $p<0.05$, ** $p<0.01$, *** $p<0.001$; *n.s.* represents "not significant") were applied.

Figure 4—figure supplement 1. Indistinguishable neuronal morphology between GCaMP6m-X_C and GFP of long-term expression. (**A**) Representative neurite tracing of multiple neurons (left) and fluorescence images of individual neurons (right) for cultured cortical neurons expressing GCaMP6m-X_C, GCaMP6m or GFP on DIV 28, DIV 35 and DIV 42. (**B** and **C**) Temporal profiles of the total length of neurites (**B**) and the soma size from DIV 3 to DIV 42 (**C**). Compared on DIV 42, no significant difference exists between GCaMP6m-Xc and GFP control; and the differences between GCaMP6m-Xc and GCaMP6m

are significant. 3 independent experiments from 3 independent culture preparations.
Standard error of the mean (S.E.M) and one-way ANOVA followed by Bonferroni for post hoc tests (criteria of significance: * $p<0.05$, ** $p<0.01$, *** $p<0.001$; *n.s.* represents "not significant") were calculated when applicable.

Figure 4—figure supplement 2. Potential relationships between and neurite length and oscillation characteristics. The peak amplitude (**A**), the average frequency (**B**), or the level of synchrony (**C**) was examined for its potential correlation with the total length of neurites, based on the data acquired by GCaMP6m-X_C in ***Figure 3*** and ***Figure 4***. The linear correlation coefficient (R^2) was evaluated between each index and neurite length.

Figure 4—figure supplement 3. Morphological analysis to compare jGCaMP7b-X_C and jGCaMP7b in cultured cortical neurons. (**A**) Cortical neurons virally-expressing jGCaMP7b-X_C, jGCaMP7b and GFP control, respectively. For each group, neurite tracing of multiple neurons (upper rows) and representative confocal fluorescence images of individual neurons (lower rows) at the selected timepoints of DIV 7 to DIV 35. (**B**) Temporal profiles of the total length of neurites summarized for jGCaMP7b-X_C and jGCaMP7b versus GFP control. (**C**) N/C ratio of neurons expressing jGCaMP7b or jGCaMP7b-X_C.
3 independent experiments from 3 independent culture preparations.
Standard error of the mean (S.E.M) and one-way ANOVA followed by Bonferroni for post hoc tests (**B**) or two-tailed unpaired Student's *t*-test (**C**) (criteria of significance: * $p<0.05$; ** $p<0.01$; *** $p<0.001$; *n.s.* represents "not significant") were calculated.

Figure 4—figure supplement 4. The long-term effects of GCaMP-X with enhanced expression levels in cultured neurons. (**A** and **B**) Protein expression levels in whole-cell

extracts from cortical neurons infected with 1 μl AAV-*Syn*-jGCaMP7b (1.0×10^{12} v.g/ml) or 1 μl (low), 2 μl (middle), 3 μl (high) AAV-*Syn*-jGCaMP7b-X_C (1.0×10^{12} v.g/ml). By western blots, anti-GFP bands and anti-GAPDH bands indicated the level of probe expression and the amount of inputs, respectively. Statistical summary for whole-cell expression levels of low/middle/high-dose jGCaMP7b-X_C in comparison to jGCaMP7b. (**C-E**) Comparison between jGCaMP7b and high-dose jGCaMP7b-X_C in cultured cortical neurons. To compare neuritogenesis (**C**), neurons virally-expressing GFP served as the control. Representative Ca^{2+} waveforms (**D**) and images (**E**) are shown for cultured cortical neurons virally-expressing jGCaMP7b or jGCaMP7b-X_C (high) on DIV 21 and DIV 28. (**F**) Statistical summary of neurite growth and Ca^{2+} oscillation, to compare the three groups by the key indices including total neurite length per view, soma size of individual neurons, and peak amplitude and FWHM of Ca^{2+} waveform.

2 independent experiments from 2 independent culture preparations.

Standard error of the mean (S.E.M) and one-way ANOVA followed by Bonferroni for post hoc tests (criteria of significance: * $p<0.05$; ** $p<0.01$; *** $p<0.001$; *n.s.* represents "not significant") were applied.

Figure 5—figure supplement 1. Effects of virally-expressed GCaMP versus GCaMP-X on mature cortical neurons. (**A** and **B**) Cultured cortical neurons from newborn ICR mice were infected on DIV 21 with GFP, jGCaMP7b and jGCaMP7b-X_C viruses (2 μL of each), respectively. Then neurons were traced by confocal microscopy on DIV 28 and DIV 35 (**A**). Total length per view was summarized in (**B**). (**C** and **D**) Oscillatory Ca^{2+} waveforms associated with color-coded fluorescence images on DIV 28 and DIV 35. (**E**) The key indices with $\Delta F/F_0$ and FWHM measured from spontaneous Ca^{2+} in cultured neurons.

2 independent experiments from 2 independent culture preparations.

Standard error of the mean (S.E.M) and one-way ANOVA followed by Bonferroni for post hoc tests (**B**) or two-tailed unpaired Student's *t*-test (**E**) (criteria of significance: * $p<0.05$; ** $p<0.01$; *** $p<0.001$; *n.s.* represents "not significant") were calculated.

Figure 5—figure supplement 2. The critical timepoints of the protocols for both *in vitro* and *in vivo* experiments. Neurons at different timepoints exhibit diverse patterns of spontaneous Ca^{2+} fluctuations. In general, cultured neurons from neonatal mice around DIV 2-3 are considered to be immature with low and sparse oscillations (Isaev et al., 2018). Cultured neurons could enter into mature stage as early as ~DIV 7 (up to DIV 56), corresponding to 8-24 weeks old adult mice *in vivo* (Dutta and Sengupta, 2016), where periodical oscillations from multiple neurons emerge around DIV 12-16. Robust and synchronized oscillations are observed usually after DIV 16 (Murphy et al., 2020; Opitz et al., 2002), which correspond to neural network formation and synaptic maturation (Mori and Mook-Jung, 2015). Virus infection was conducted for both neonatal (DIV 0) and mature (DIV 21) neurons to culture further for *in vitro* experiments. For *in vivo* studies, adult mice (>8 weeks) were used for virus injection. One to two months (4-8 weeks) post injection and thereafter (8-13 weeks) are considered as within optimal time window (OTW) and beyond OTW, respectively (Chen et al., 2013; Resendez et al., 2016; Tian et al., 2009).

Figure 6—figure supplement 1. Long-term effects of GCaMP-X with high expression levels *in vivo*. (**A**) Immunostaining images of neurons infected by AAV-*Syn*-GCaMP6m ($5x10^{11}$ or $1.0x10^{12}$ v.g/ml, 60 nl) and AAV-*Syn*-GCaMP6m-X_C ($1.0x10^{13}$ v.g/ml, 60 nl) at left or right S1BF. 13 weeks after microinjection, brain slices of injected mice were stained with anti-GFP (Alexa Fluo 647 nm, red), NeuN (Alexa Fluo 568 nm, yellow) and DAPI (blue) to reflect the protein expression of the indicators, cell bodies and nuclear envelops, respectively. The GFP channel (green) was to indicate the positive neurons. Neurons without fluorescence in GFP channel and anti-GFP channel served as the blank cell control. (**B**) Cytosolic fluorescence intensity of anti-GFP of each neuron was normalized by that of low-dose GCaMP6m group ($5x10^{11}$ v.g/ml) then summarized and compared. (**C**) Soma size calculated for each neuron and summarized to compare. The group of high-dose

GCaMP6m-X_C had the highest level of expression whereas causing the least damage to neurons judged from its largest soma size among the three groups of neurons.

Standard error of the mean (S.E.M) and one-way ANOVA followed by Bonferroni for post hoc tests (criteria of significance: * $p<0.05$; ** $p<0.01$; *** $p<0.001$; *n.s.* represents "not significant") were applied.

Figure 7—figure supplement 1. Chronic evaluation of cultured cortical neurons from Ai148 mice with inducible GCaMP6f expression. (**A**) Representative neurite tracing and fluorescence images for cultured cortical neurons expressing GCaMP6f or GFP on DIV 7 and DIV 28, respectively. GCaMP6f expression was induced by 10 μM TMP from Rasgrf2-2A-dCre x Ai148 mice. GFP control neurons were also treated with the same dose of TMP. (**B-D**) Temporal profiles of N/C ratio (**B**), total neurite length (**C**), and soma size (**D**) for Ai148 neurons. (**E** and **F**) Spontaneous Ca^{2+} oscillations from the nucleus-excluded versus nucleus-filled (N/C ratio>0.8) subgroups of neurons from Ai148 mice. Time-laps color-coded Ca^{2+} fluorescence images on DIV 28 (**E**) and Ca^{2+} waveforms from DIV 7 to DIV 28 (**F**). (**G** and **H**) Temporal profiles of peak amplitude ($\Delta F/F_0$, **G**) and oscillation frequency (mHz, **H**). Standard error of the mean (S.E.M) and Student's *t*-test (two-tailed unpaired with criteria of significance: * $p<0.05$; ** $p<0.01$; *** $p<0.001$) were calculated when applicable.

Figure 7—figure supplement 2. Neuritogenesis of cortical neuron from transgenic mice with TMP-inducible GCaMP. (**A**) Neurite tracings for Ai148 GCaMP6f positive neurons (Rasgrf2-2A-dCre x Ai148 mice) versus Ai140 GFP positive neurons (Rasgrf2-2A-dCre x Ai140 mice) on DIV 21 and DIV 28, both induced by 10 μM TMP. Ai140 GFP negative neurons and ICR mouse neurons serves as additional controls, both infected GFP viruses, and also added with 10 μM TMP. (**B**) Statistical summary of total neurite length per view. No significant difference was found among ICR control, Ai140 GFP negative and Ai140 GFP

positive neurons, thus ruling out the potential biases or artifacts due to tTA toxicity, different strains of mice, or virus effects. The total length of neurites was significantly reduced in Ai148 GCaMP6f positive neurons, as compared with Ai140 GFP positive neurons.

Standard error of the mean (S.E.M) and one-way ANOVA followed by Bonferroni for post hoc tests (criteria of significance: * $p<0.05$; ** $p<0.01$; *** $p<0.001$; *n.s.* represents "not significant") were applied.

Figure 7—figure supplement 3. Effects on cortical neurons by transgenic GCaMP6f expression induced at the mature stage. (**A** and **B)** GCaMP6f was induced in cultured cortical neurons from Rasgrf2-2A-dCre x Ai148 mice by 10 μM TMP on DIV 14, then imaged by confocal microscopy on DIV 21 and DIV 28. Neurons from ICR mice treated with TMP treatment and infected by GFP virus served as the control. Based on neurite tracings (**A**), the total length per view (**B**) was summarized. Fluorescence images were zoomed in to show single neurons. (**C** and **D)** Oscillatory Ca^{2+} waveforms associated with color-coded fluorescence images on DIV 21and DIV 28. (**E**) Statistical summary for the key indices of $\Delta F/F_0$ (from each neuron) and correlation coefficient (from each view).

2 independent experiments were performed with 2 independent culture preparations.

Standard error of the mean (S.E.M) and two-tailed unpaired Student's *t*-test (criteria of significance: * $p<0.05$; ** $p<0.01$; *** $p<0.001$; *n.s.* represents "not significant") were applied.

SUPPLEMENTAL VIDEO LEGENDS

Figure 3—video 1. Spontaneous Ca^{2+} oscillation of cultured cortical neurons virally-expressing GCaMP6m-X_C on DIV 28. Neurons exhibited highly synchronized Ca^{2+} oscillations with robust spikes and complicated neurite connections. Video plays at 60x speed.

Figure 3—video 2. Spontaneous Ca^{2+} oscillation of cultured cortical neurons virally-expressing GCaMP6m on DIV 17. Neurons exhibited ultralong lasting Ca^{2+} signals which may be associated with apoptotic death of neurons. Video plays at 60x speed.

Figure 3—video 3. Spontaneous Ca^{2+} oscillation of cultured cortical neurons virally-expressing GCaMP6m on DIV 28. Most of the neurons were broken and no longer exhibited Ca^{2+} oscillation. Video plays at 60x speed.

Figure 5—video 1. *In vivo* two-photon imaging of spontaneous Ca^{2+} oscillation of neurons virally-expressing GCaMP6m-Xc in S1 primary somatosensory cortex without optimal time window (11 weeks post virus). Enlarged images (512 x 512 pixels, 300 x 300 μm^2) of L2/3 cells (150-250 μm under the pia) in S1BF were collected at 7.4 Hz frame rate. Video plays at 6x speed.

Figure 5—video 2. *In vivo* two-photon imaging of spontaneous Ca^{2+} oscillation of neurons virally-expressing GCaMP6m in S1 primary somatosensory cortex without optimal time window (8 weeks post virus). Enlarged images (512 x 512 pixels, 300 x 300 μm^2) of L2/3 cells (150-250 μm under the pia) in S1BF were collected at 7.4 Hz frame rate. Neurons with nucleus-filled GCaMP6m barely fired. Video plays at 6x speed.

SOURCE DATA LEGENDS

Figure 1—figure supplement 1—source data 1.

Source data for **Figure 1—figure supplement 1A**. Original uncropped western blotting gels with indication of the cropped areas.

Figure 1—figure supplement 1—source data 2.

Source data for **Figure 1—figure supplement 1C**. Original uncropped western blotting gels with indication of the cropped areas.

Figure 1—figure supplement 3—source data 1.

Source data for **Figure 1—figure supplement 3A, B**. Original uncropped western blotting gels with indication of the cropped areas.

Figure 4—figure supplement 4—source data 1.

Source data for **Figure 4—figure supplement 4A.** Original uncropped western blotting gels with indication of the cropped areas.

A

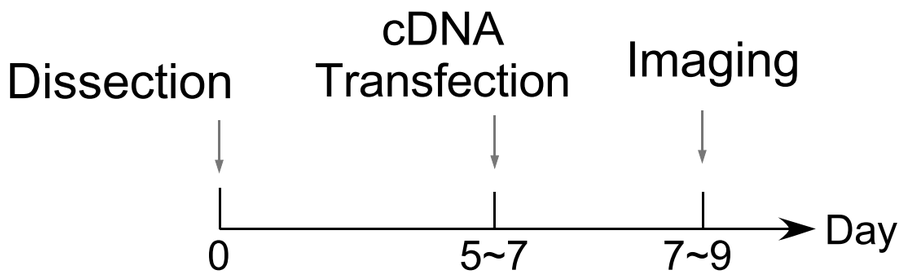
Dissection
cDNA Transfection
Imaging
0
5~7
7~9
Day

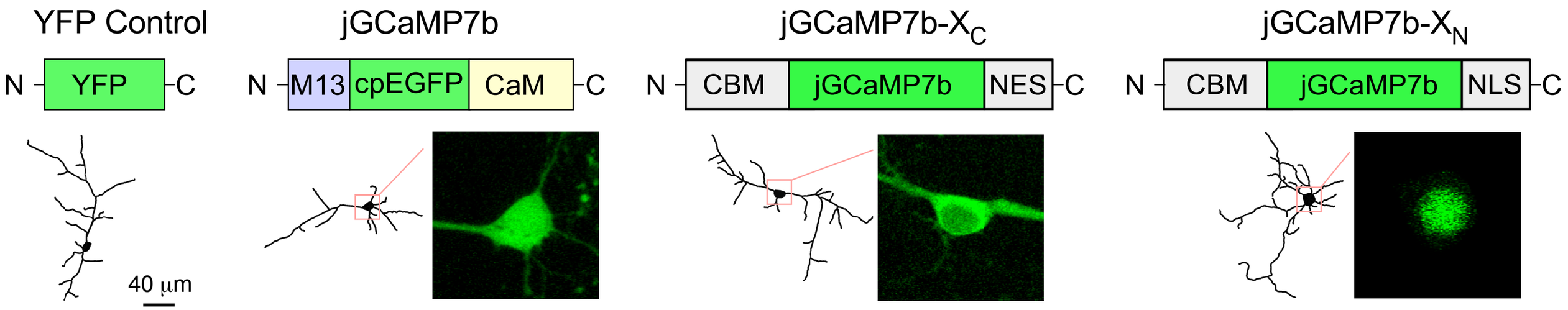
YFP Control
jGCaMP7b
jGCaMP7b-X$_C$
jGCaMP7b-X$_N$
N
YFP
C
M13
cpEGFP
CaM
CBM
jGCaMP7b
NES
NLS
40 μm

B

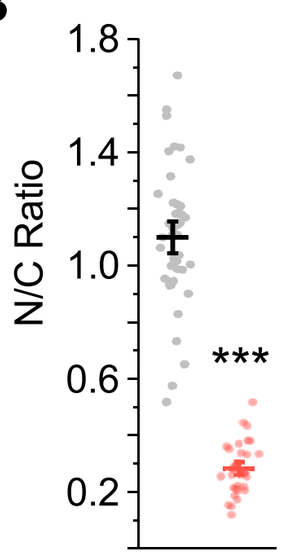
N/C Ratio
1.8
1.4
1.0
0.6
0.2
***
jGCaMP7b
jGCaMP7b-X$_C$

C

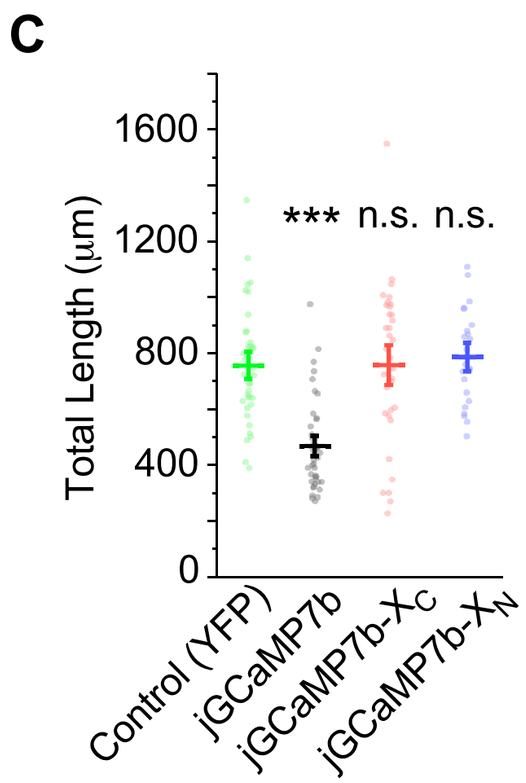
Total Length (μm)
1600
1200
800
400
0
*** n.s. n.s.
Control (YFP)
jGCaMP7b
jGCaMP7b-X$_C$
jGCaMP7b-X$_N$

D

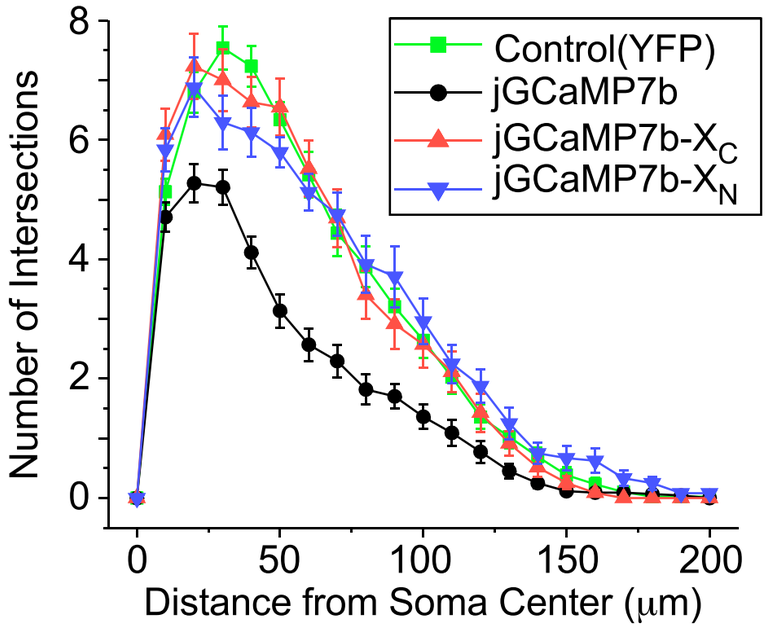
Number of Intersections
Distance from Soma Center (μm)
Control(YFP)
jGCaMP7b
jGCaMP7b-X$_C$
jGCaMP7b-X$_N$

E

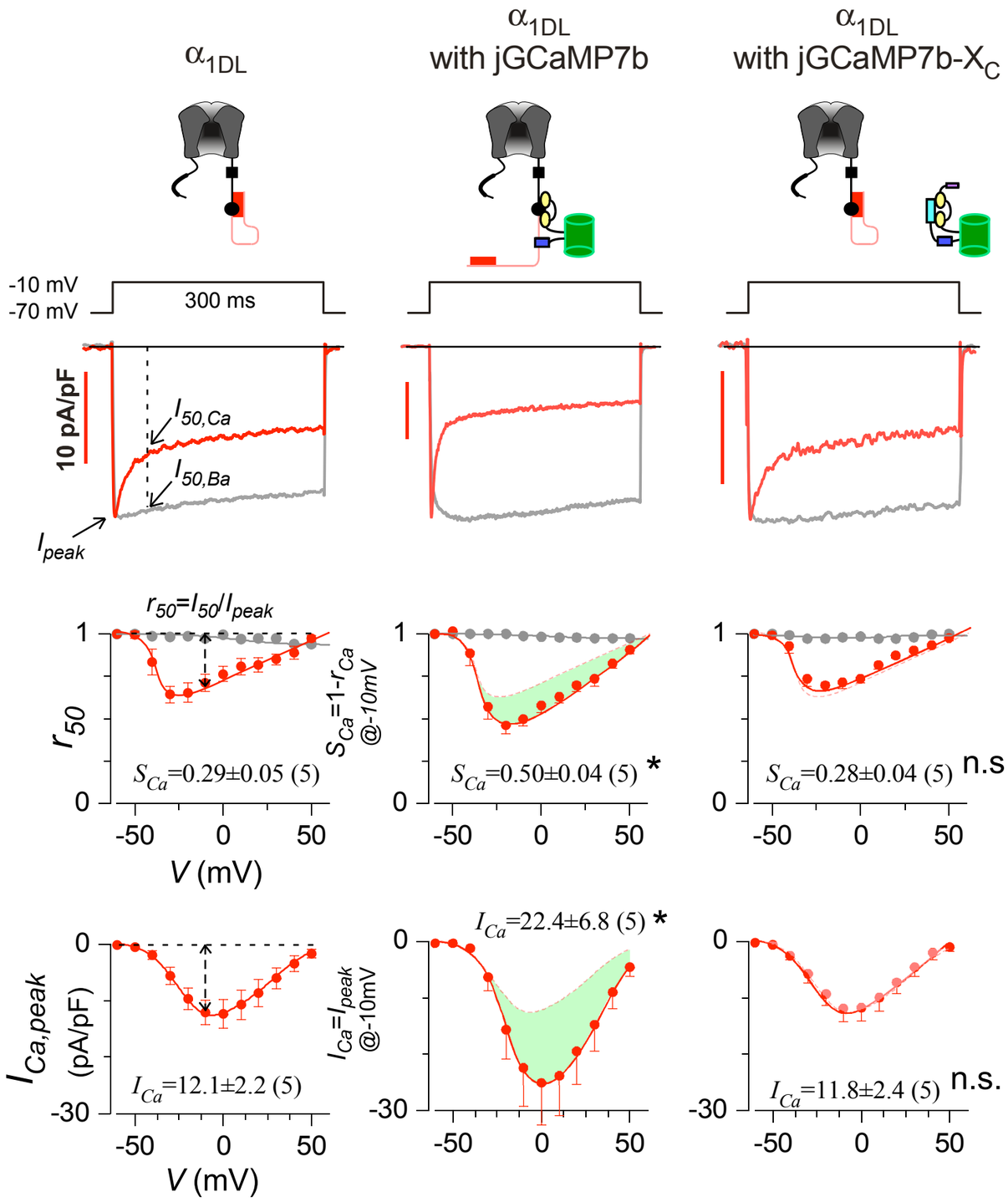
α_{1DL}
α_{1DL} with jGCaMP7b
α_{1DL} with jGCaMP7b-X$_C$
-10 mV
-70 mV
300 ms
10 pA/pF
$I_{50,Ca}$
$I_{50,Ba}$
I_{peak}
$r_{50}=I_{50}/I_{peak}$
r_{50}
S_{Ca}=1-r_{Ca} @-10mV
S_{Ca}=0.29±0.05 (5)
S_{Ca}=0.50±0.04 (5) *
S_{Ca}=0.28±0.04 (5) n.s.
V (mV)
$I_{Ca,peak}$ (pA/pF)
I_{Ca}=12.1±2.2 (5)
I_{Ca}=22.4±6.8 (5) *
I_{Ca}=11.8±2.4 (5) n.s.
I_{Ca}=I_{peak} @-10mV

A

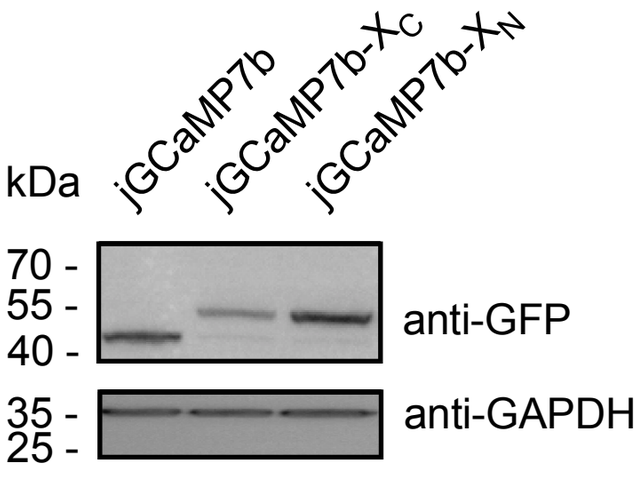
HEK 293 Whole-cell
jGCaMP7b
jGCaMP7b-XC
jGCaMP7b-XN
kDa
70 -
55 -
40 -
35 -
25 -
anti-GFP
anti-GAPDH

B

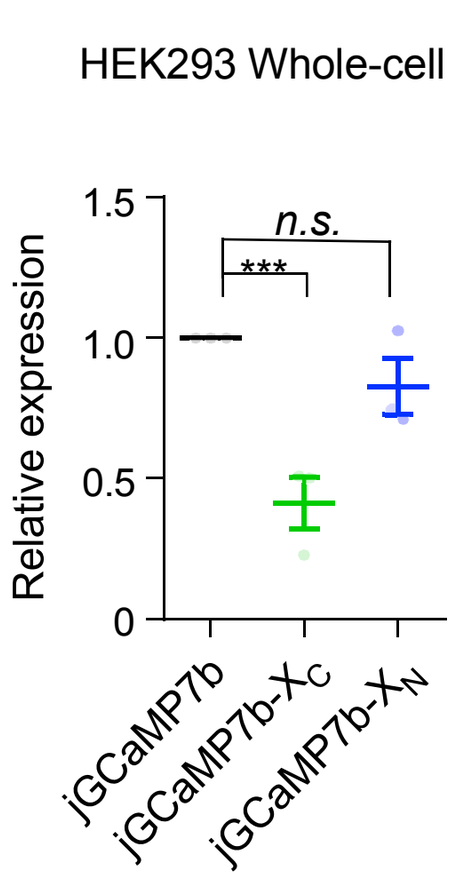
HEK293 Whole-cell
Relative expression
1.5
1.0
0.5
0
n.s.
***
jGCaMP7b
jGCaMP7b-XC
jGCaMP7b-XN

C

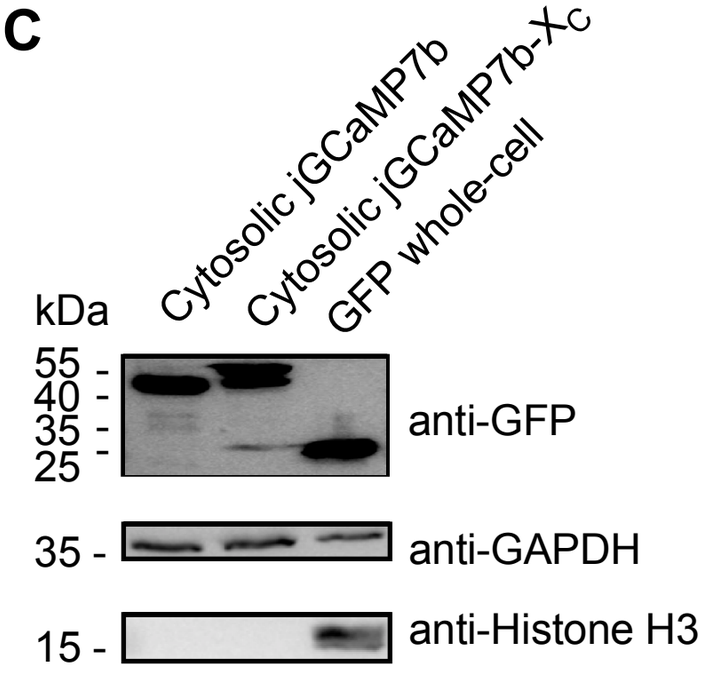
Cytosolic jGCaMP7b
Cytosolic jGCaMP7b-XC
GFP whole-cell
kDa
55 -
40 -
35 -
25 -
anti-GFP
35 -
anti-GAPDH
15 -
anti-Histone H3

D

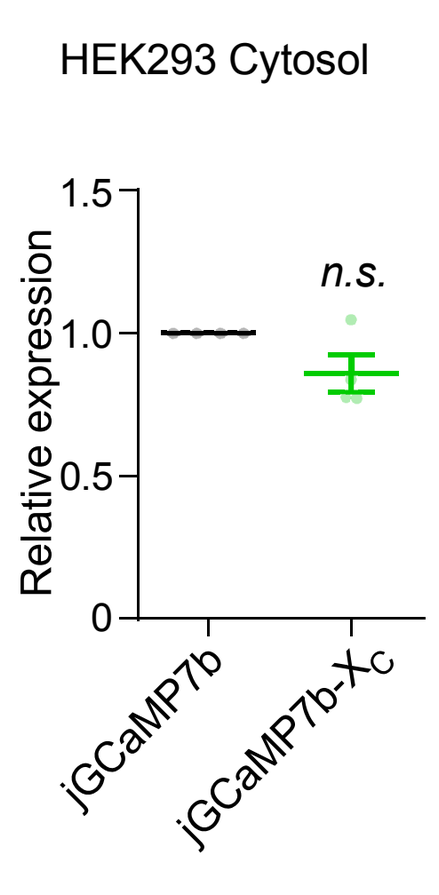
HEK293 Cytosol
Relative expression
1.5
1.0
0.5
0
n.s.
jGCaMP7b
jGCaMP7b-XC

E

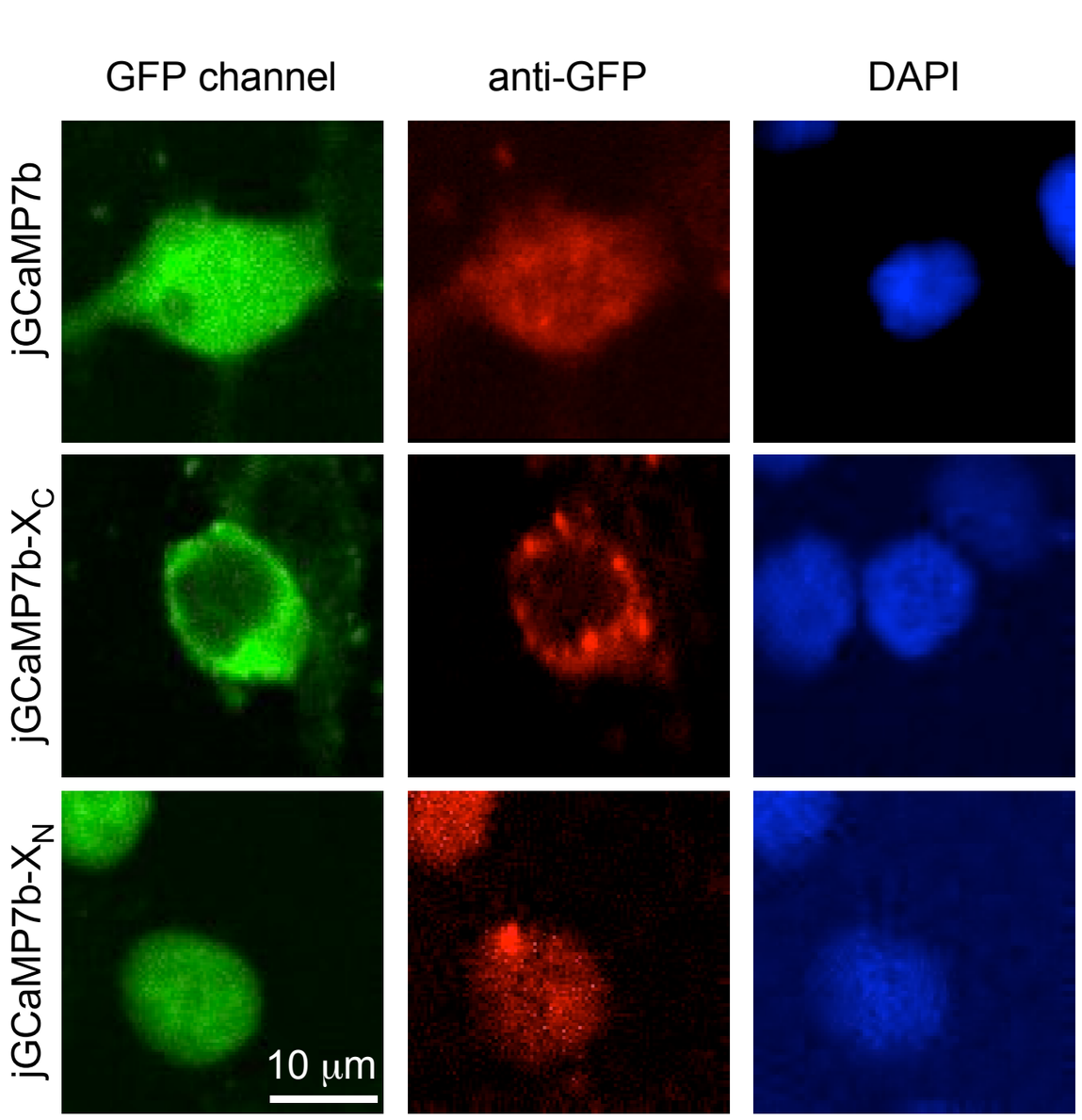
GFP channel
anti-GFP
DAPI
jGCaMP7b
jGCaMP7b-XC
jGCaMP7b-XN
10 μm

F

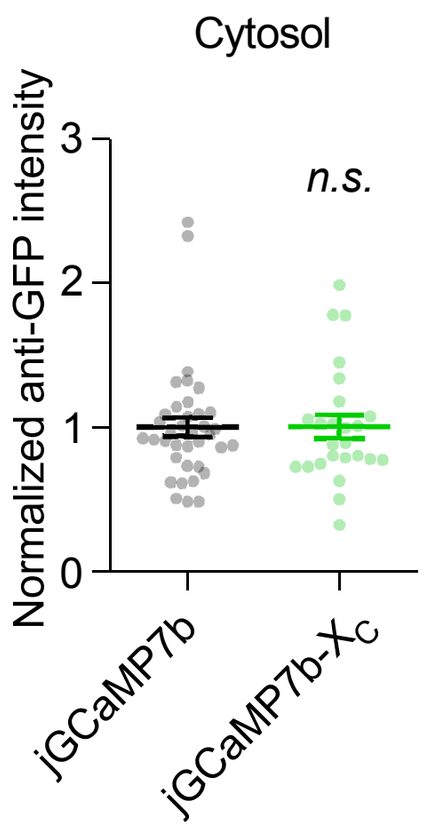
Cytosol
Normalized anti-GFP intensity
3
2
1
0
n.s.
jGCaMP7b
jGCaMP7b-XC

G

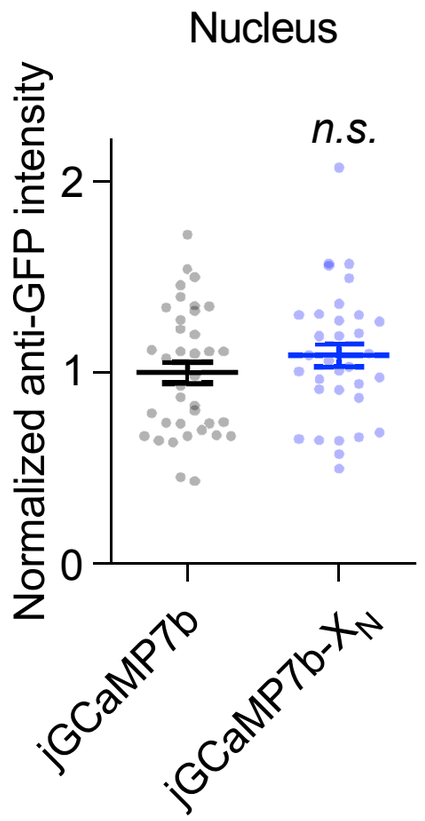
Nucleus
Normalized anti-GFP intensity
2
1
0
n.s.
jGCaMP7b
jGCaMP7b-XN

H

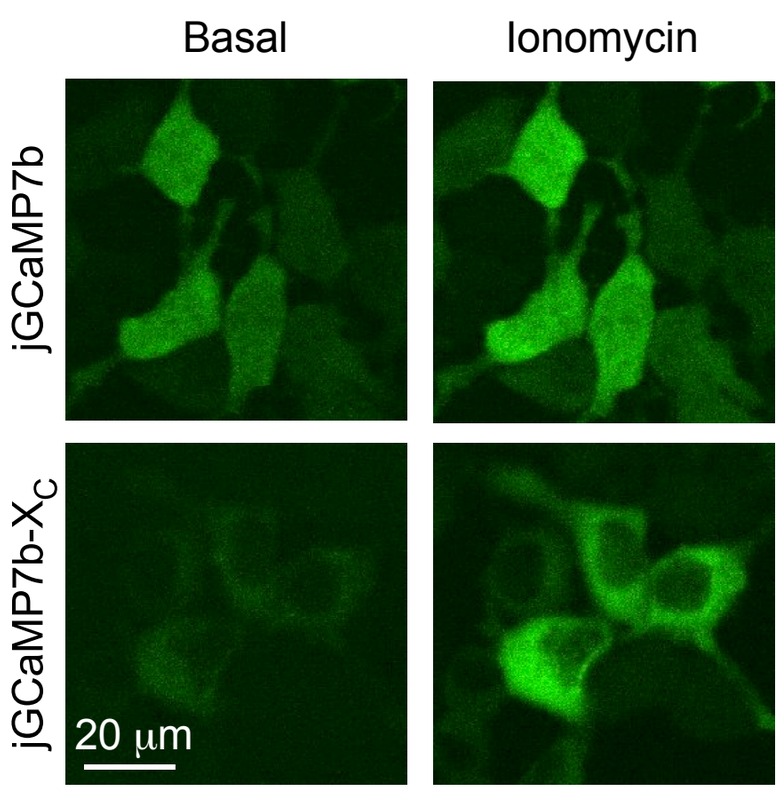
Basal
Ionomycin
jGCaMP7b
jGCaMP7b-XC
20 μm

I

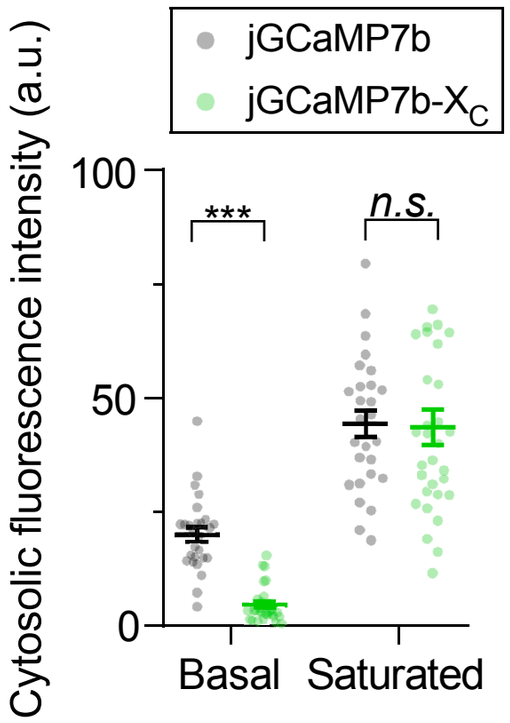
jGCaMP7b
jGCaMP7b-XC
Cytosolic fluorescence intensity (a.u.)
100
50
0
***
n.s.
Basal
Saturated

A

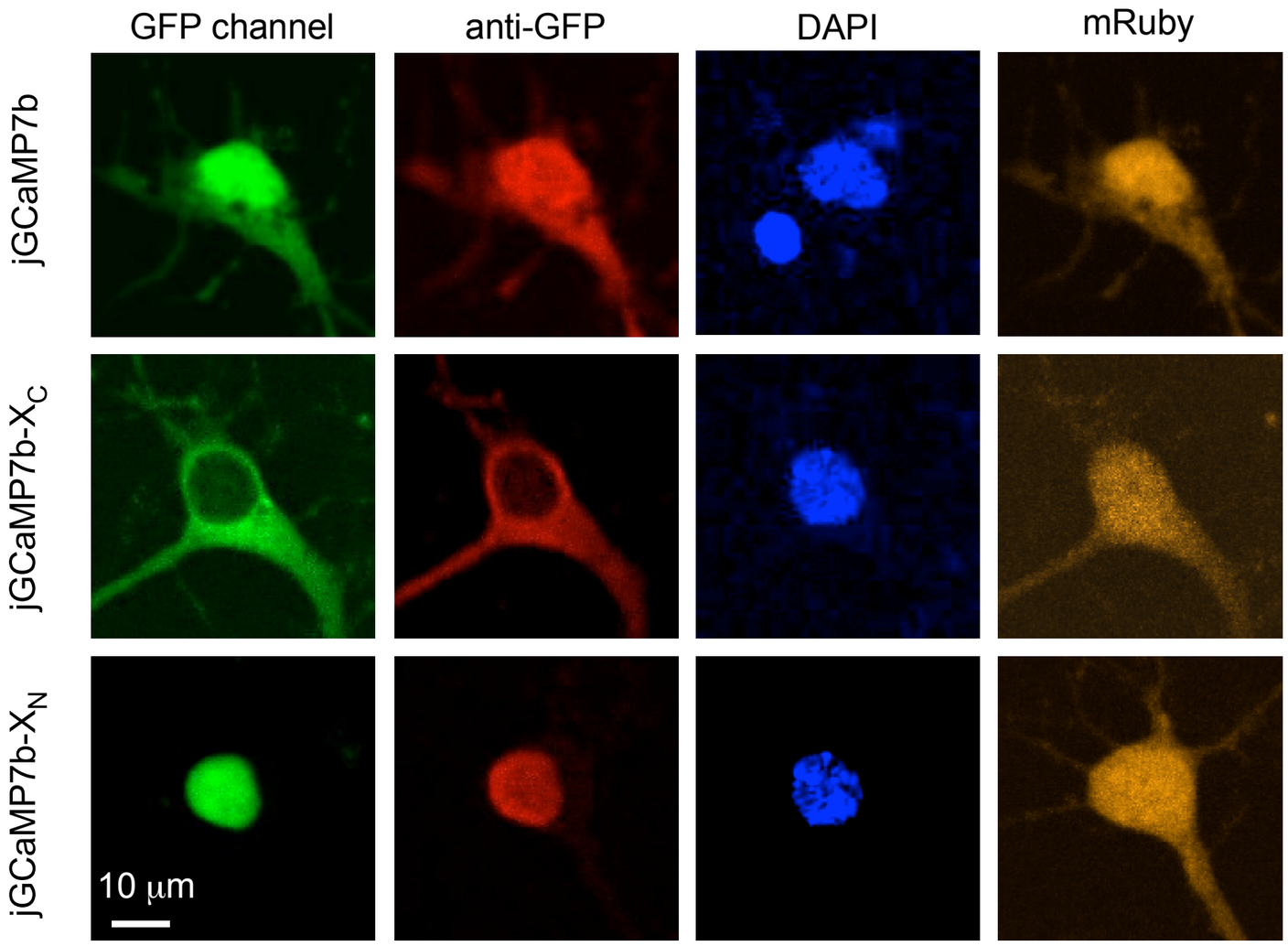
GFP channel
anti-GFP
DAPI
mRuby
jGCaMP7b
jGCaMP7b-X_C
jGCaMP7b-X_N
10 μm

B

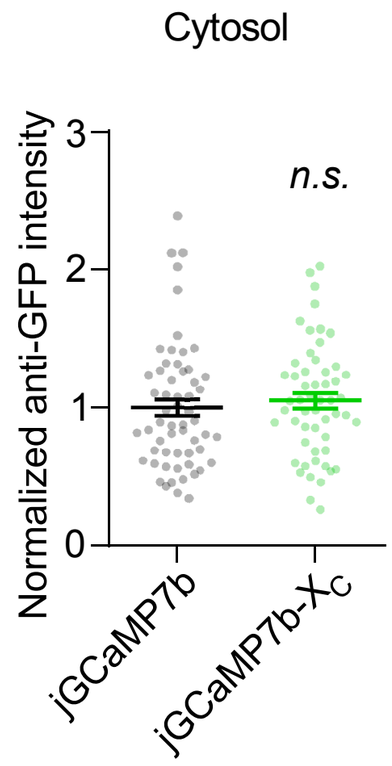
Cytosol
Normalized anti-GFP intensity
n.s.
jGCaMP7b
jGCaMP7b-X_C

C

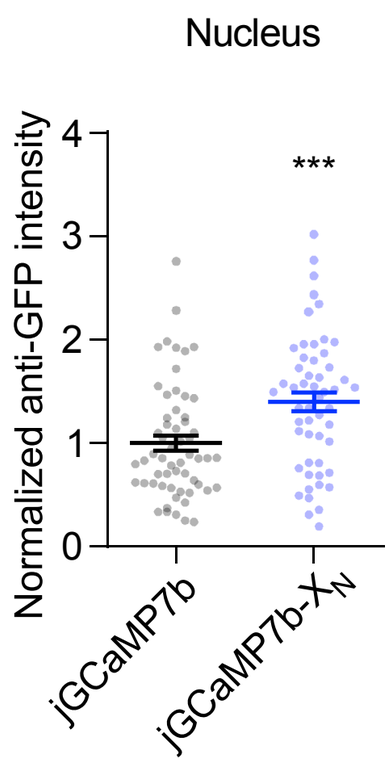
Nucleus
Normalized anti-GFP intensity
***
jGCaMP7b
jGCaMP7b-X_N

D

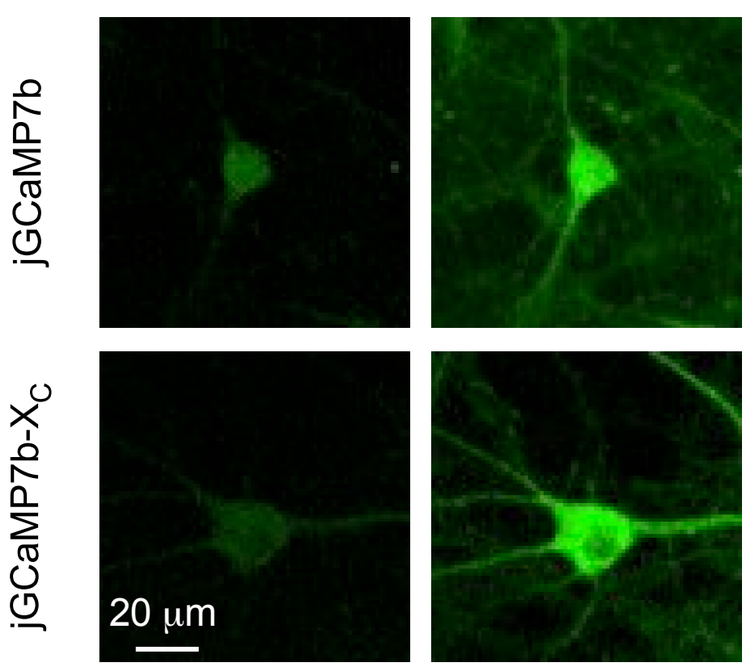
Basal
Ionomycin
jGCaMP7b
jGCaMP7b-X_C
20 μm

E

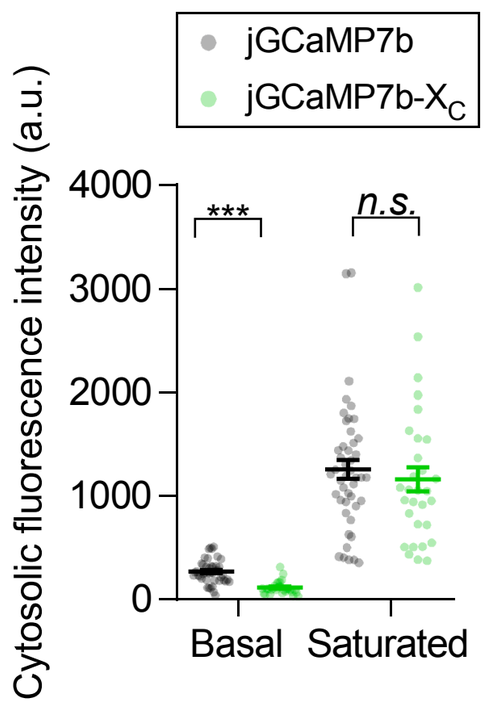
jGCaMP7b
jGCaMP7b-X_C
Cytosolic fluorescence intensity (a.u.)
***
n.s.
Basal
Saturated

F

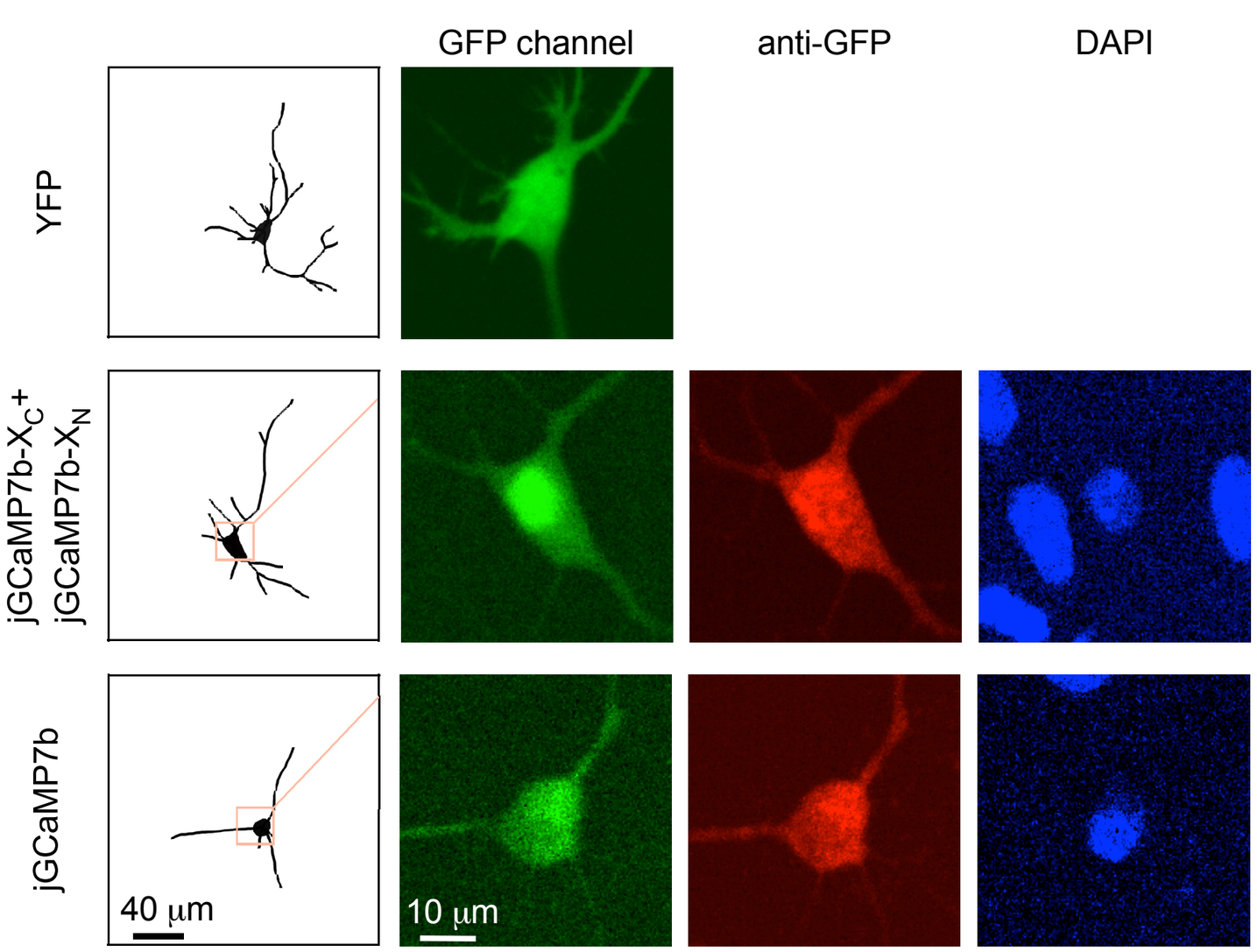
GFP channel
anti-GFP
DAPI
YFP
jGCaMP7b-X_C+ jGCaMP7b-X_N
jGCaMP7b
40 μm
10 μm

G

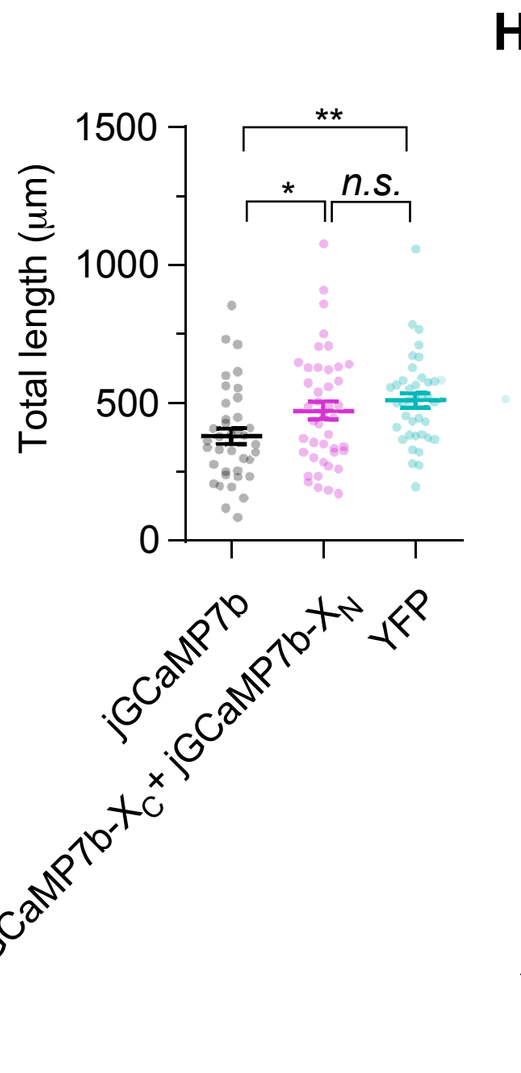
Total length (μm)
**
*
n.s.
jGCaMP7b
jGCaMP7b-X_C+ jGCaMP7b-X_N
YFP

H

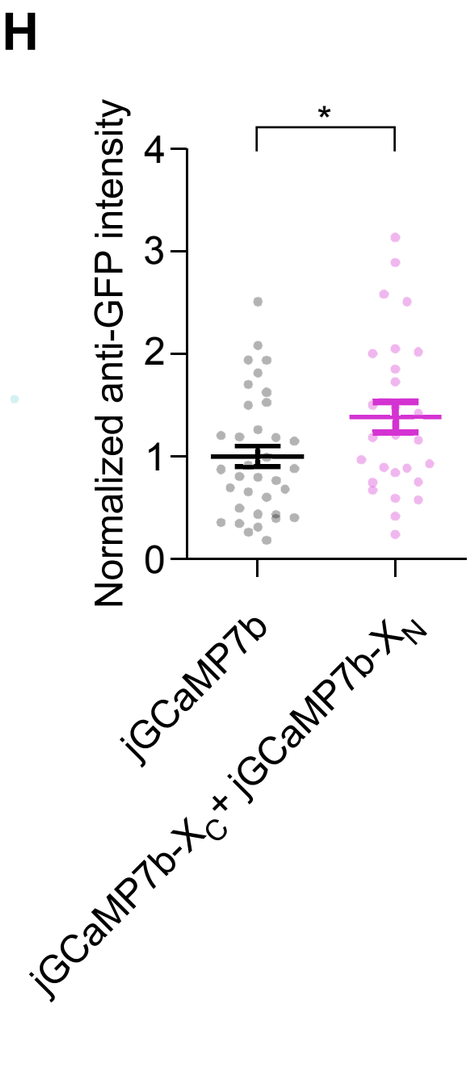
Normalized anti-GFP intensity
*
jGCaMP7b
jGCaMP7b-X_C+ jGCaMP7b-X_N

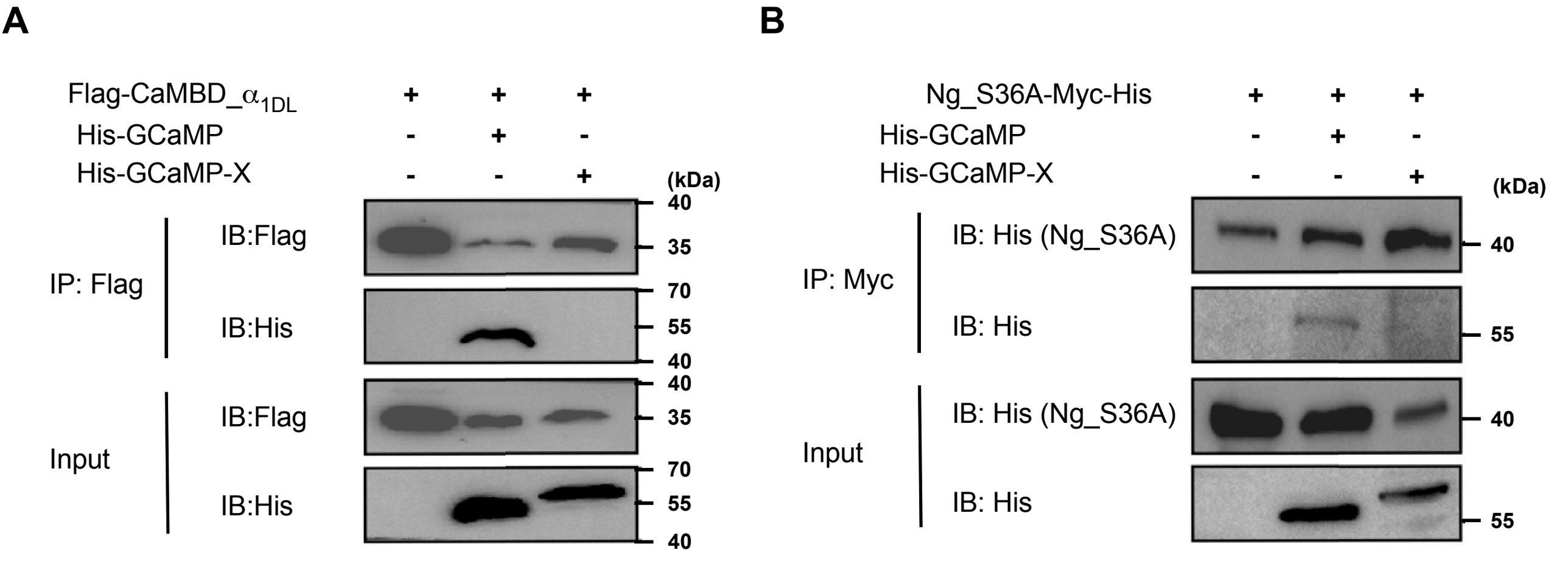
A
Flag-CaMBD_α1DL + + +
His-GCaMP - + -
His-GCaMP-X - - +
(kDa)
IP: Flag
IB:Flag
IB:His
Input
IB:Flag
IB:His
40
35
70
55
40
40
35
70
55
40
B
Ng_S36A-Myc-His + + +
His-GCaMP - + -
His-GCaMP-X - - +
(kDa)
IP: Myc
IB: His (Ng_S36A)
IB: His
Input
IB: His (Ng_S36A)
IB: His
40
55
40
55

A

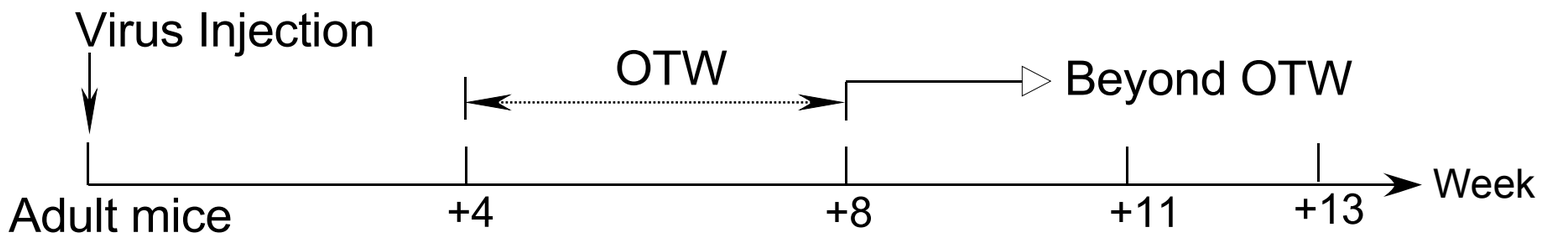
Virus Injection
OTW
Beyond OTW
Adult mice
+4
+8
+11
+13
Week

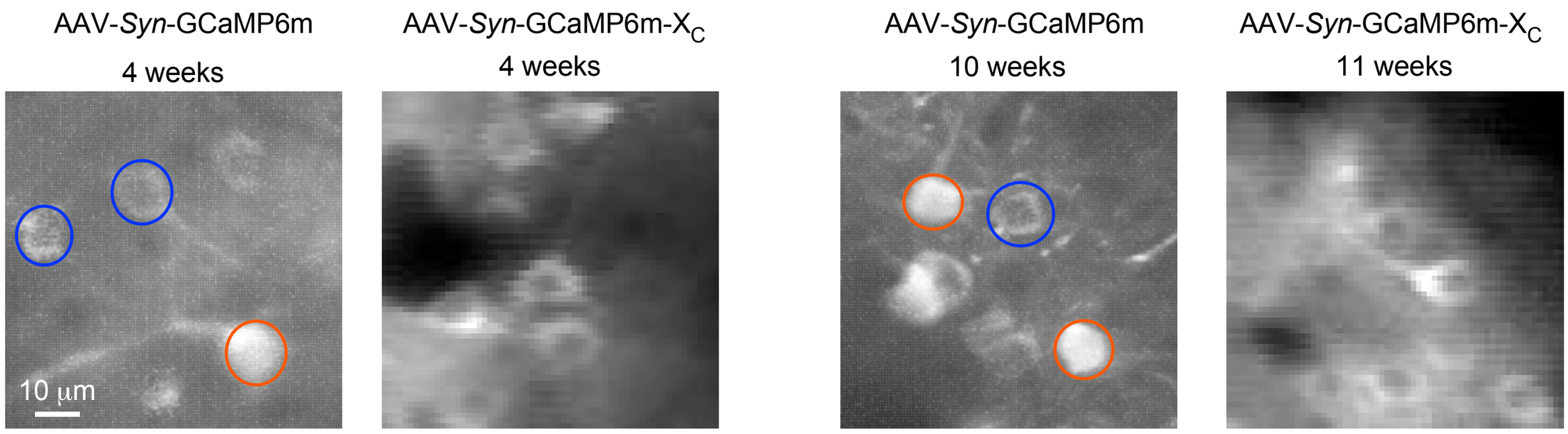
AAV-Syn-GCaMP6m
4 weeks
AAV-Syn-GCaMP6m-XC
4 weeks
AAV-Syn-GCaMP6m
10 weeks
AAV-Syn-GCaMP6m-XC
11 weeks
10 μm

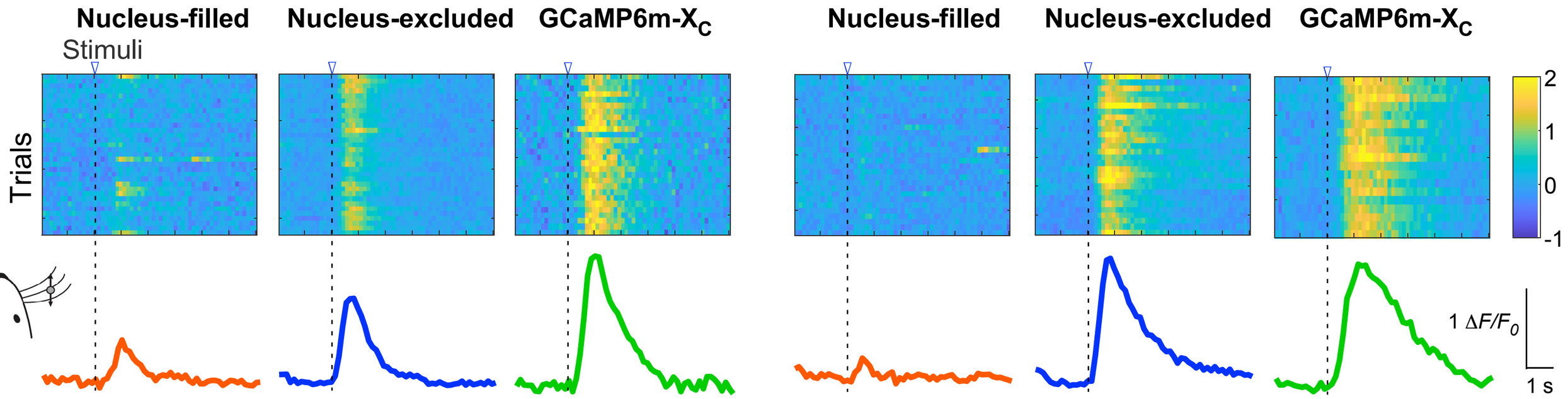
Nucleus-filled
Nucleus-excluded
GCaMP6m-XC
Nucleus-filled
Nucleus-excluded
GCaMP6m-XC
Stimuli
Trials
1 ΔF/F0
1 s

B

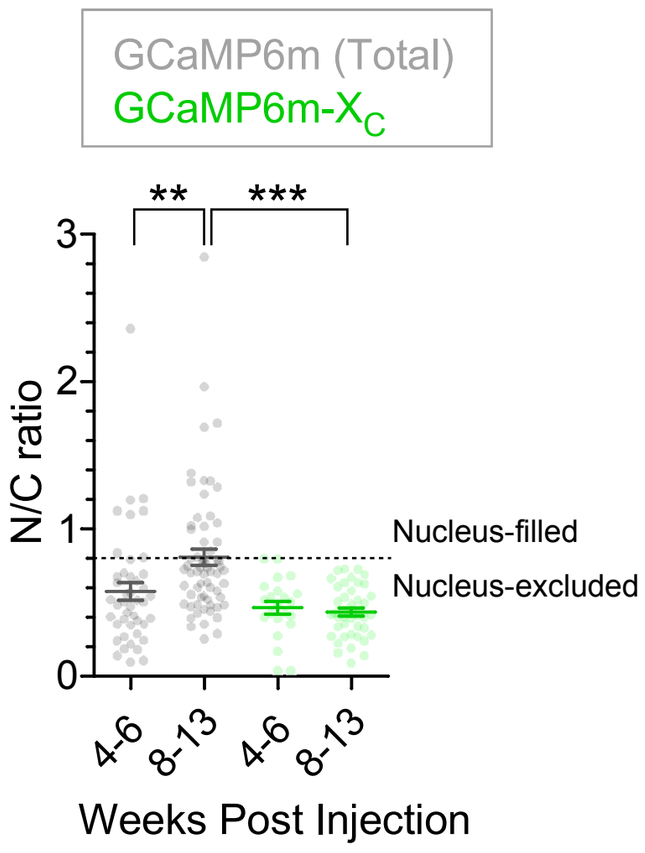
GCaMP6m (Total)
GCaMP6m-XC
**
***
N/C ratio
Nucleus-filled
Nucleus-excluded
4-6
8-13
4-6
8-13
Weeks Post Injection

C

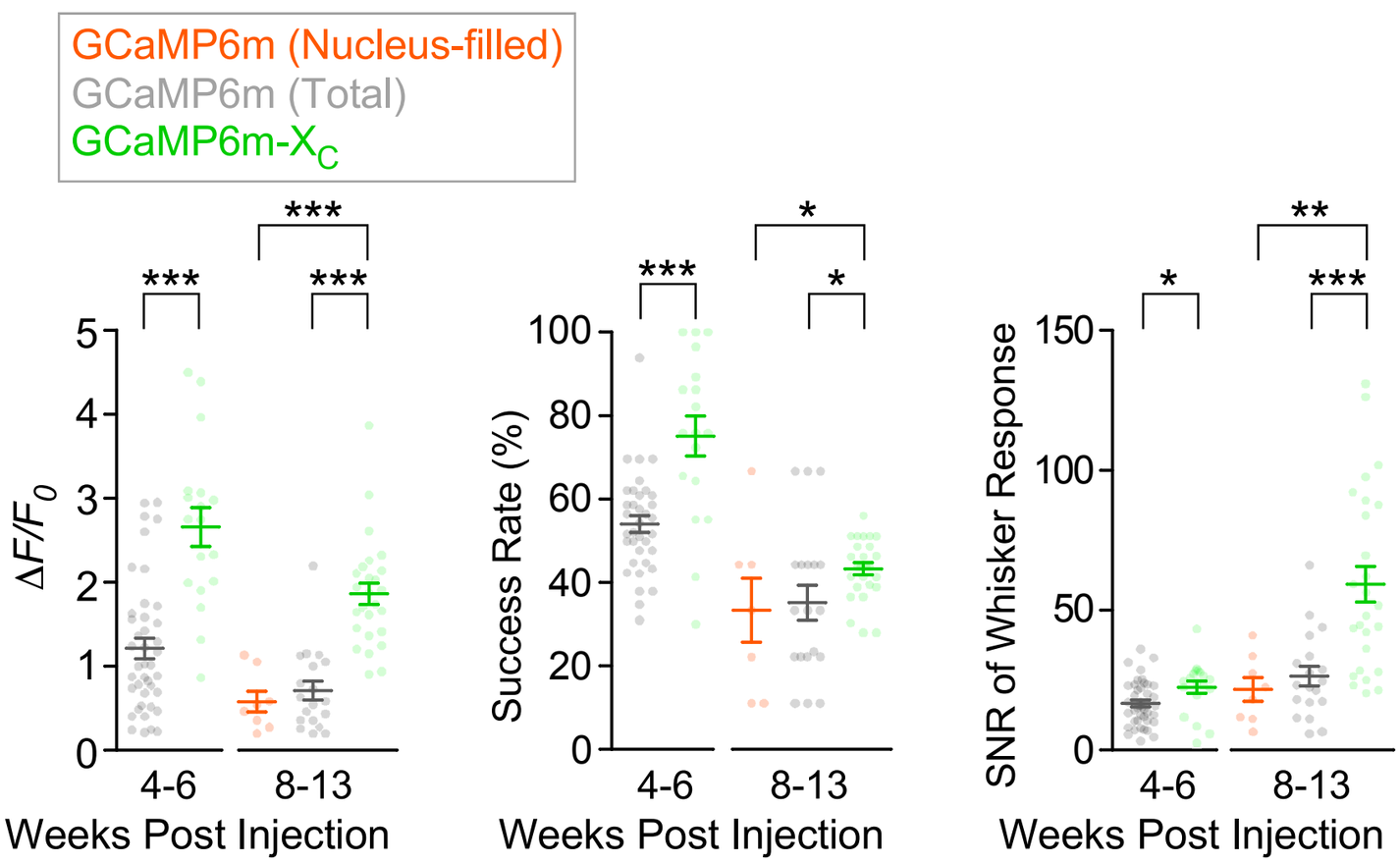
GCaMP6m (Nucleus-filled)
GCaMP6m (Total)
GCaMP6m-XC
ΔF/F0
Success Rate (%)
SNR of Whisker Response
4-6
8-13
Weeks Post Injection

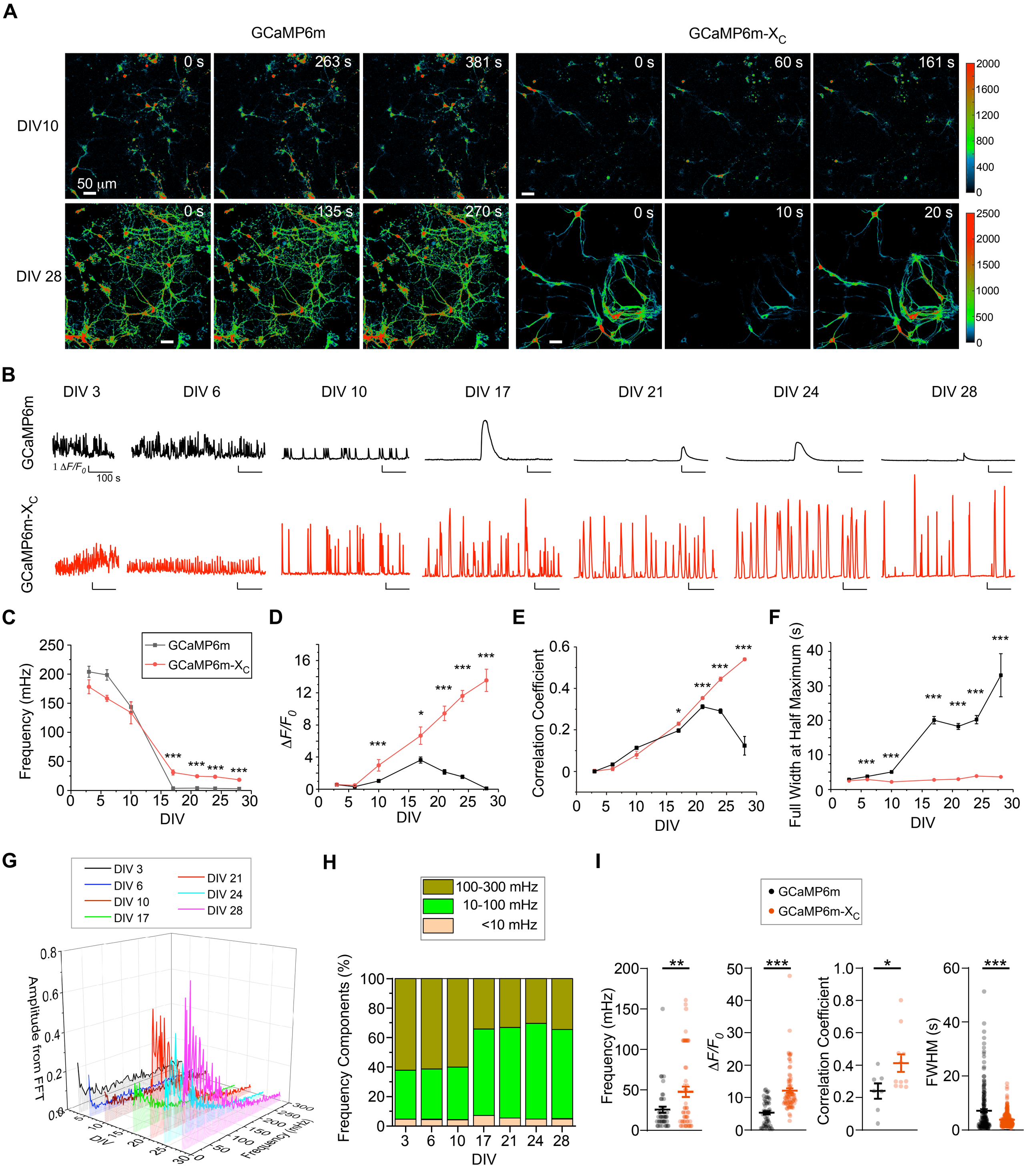
A
GCaMP6m
GCaMP6m-X_C
DIV10
DIV 28
0 s
263 s
381 s
60 s
161 s
135 s
270 s
10 s
20 s
50 μm
2000
1600
1200
800
400
0
2500
2000
1500
1000
500
0
B
DIV 3
DIV 6
DIV 10
DIV 17
DIV 21
DIV 24
DIV 28
GCaMP6m
GCaMP6m-X_C
1 ΔF/F_0
100 s
C
Frequency (mHz)
DIV
GCaMP6m
GCaMP6m-X_C
D
ΔF/F_0
E
Correlation Coefficient
F
Full Width at Half Maximum (s)
G
Amplitude from FFT
Frequency (mHz)
H
100-300 mHz
10-100 mHz
<10 mHz
Frequency Components (%)
I
Frequency (mHz)
ΔF/F_0
Correlation Coefficient
FWHM (s)

A

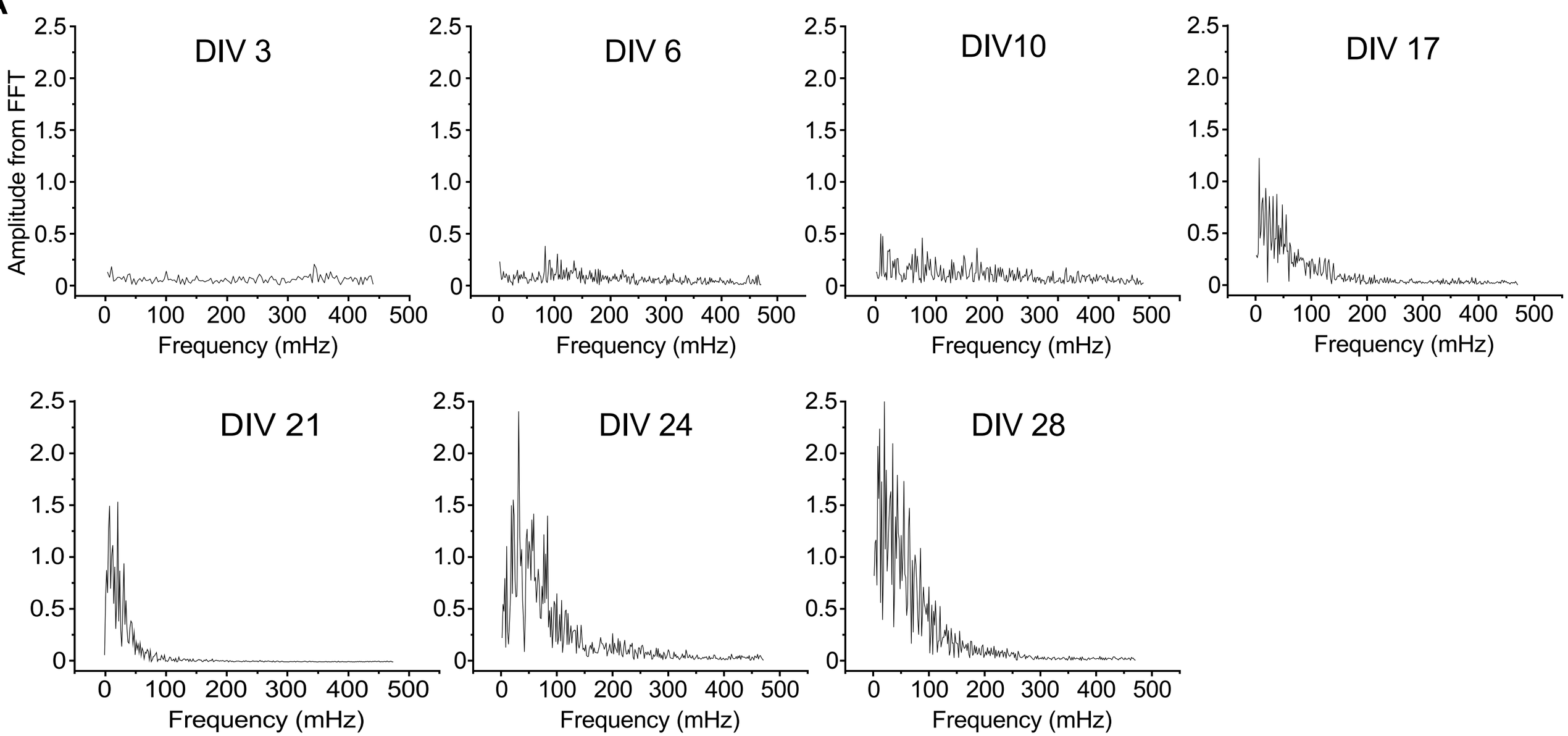
DIV 3
DIV 6
DIV10
DIV 17
DIV 21
DIV 24
DIV 28
Amplitude from FFT
Frequency (mHz)
0
0.5
1.0
1.5
2.0
2.5
0
100
200
300
400
500

B

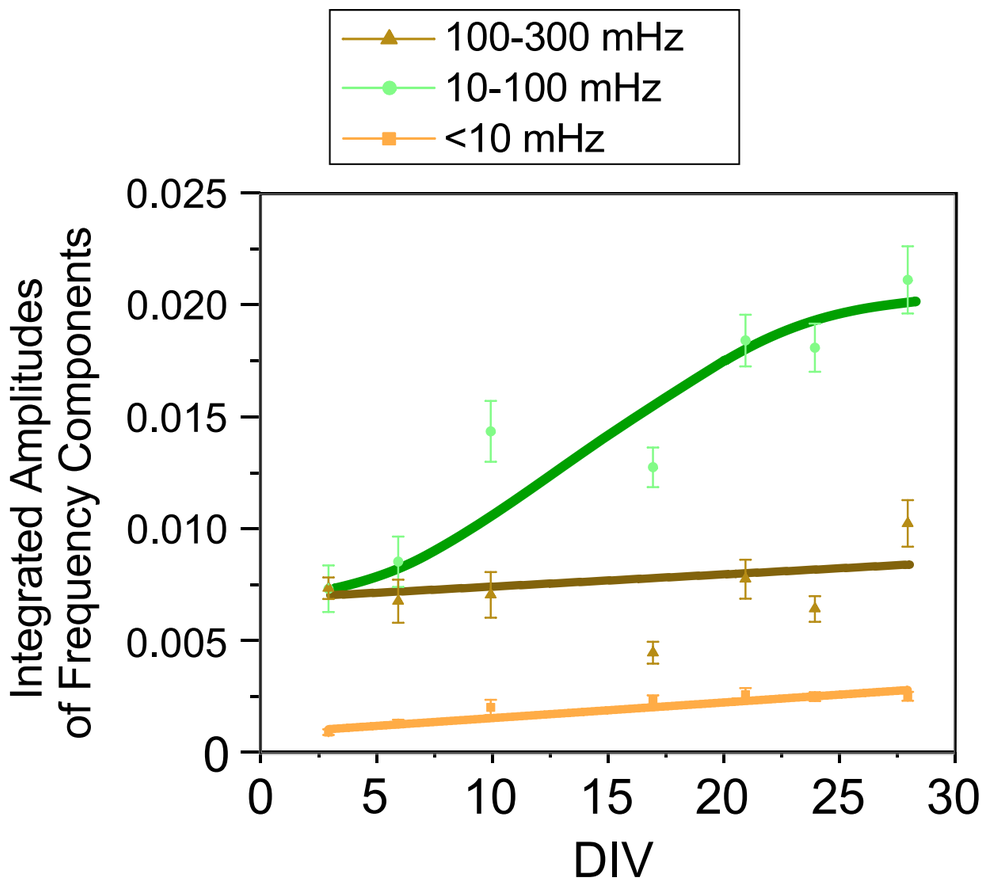
100-300 mHz
10-100 mHz
<10 mHz
Integrated Amplitudes
of Frequency Components
DIV
0
0.005
0.010
0.015
0.020
0.025
0
5
10
15
20
25
30

A

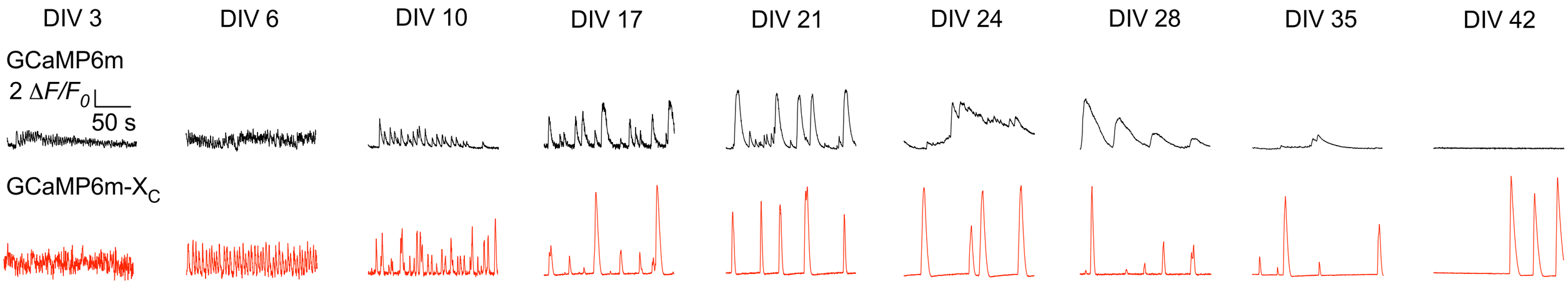
DIV 3
DIV 6
DIV 10
DIV 17
DIV 21
DIV 24
DIV 28
DIV 35
DIV 42
GCaMP6m
2 ΔF/F0
50 s
GCaMP6m-XC

B

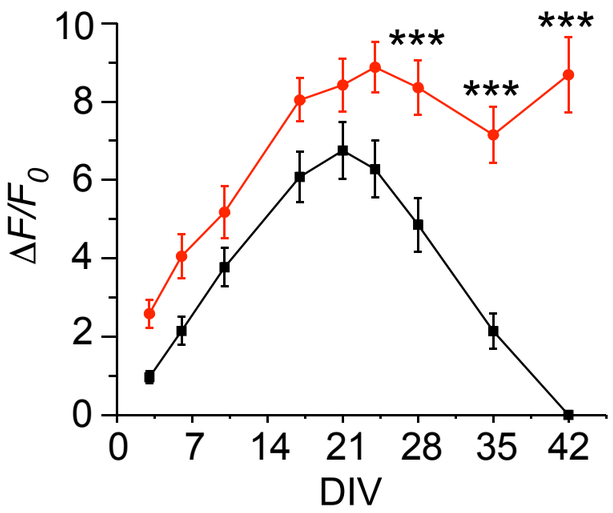
ΔF/F0
DIV
***
***
***

C

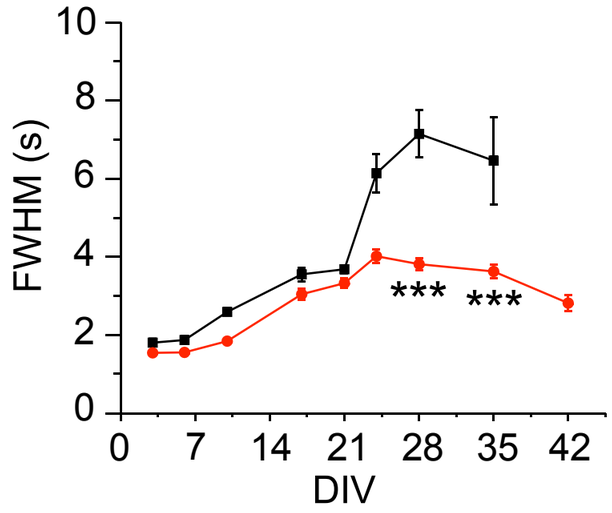
FWHM (s)
DIV
***
***

D

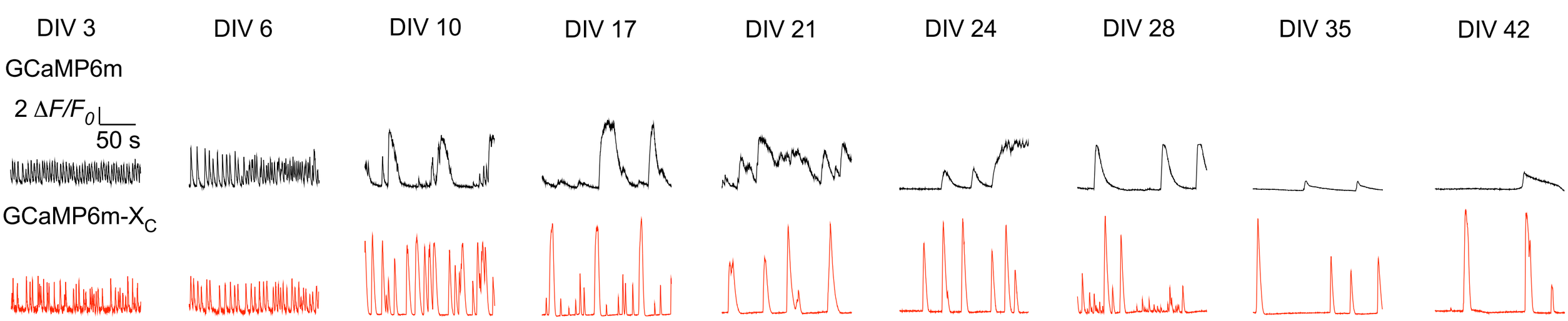
DIV 3
DIV 6
DIV 10
DIV 17
DIV 21
DIV 24
DIV 28
DIV 35
DIV 42
GCaMP6m
2 ΔF/F0
50 s
GCaMP6m-XC

E

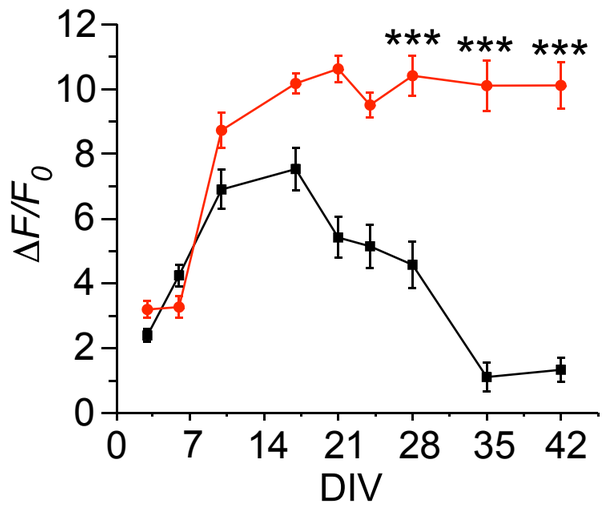
ΔF/F0
DIV
***
***
***

F

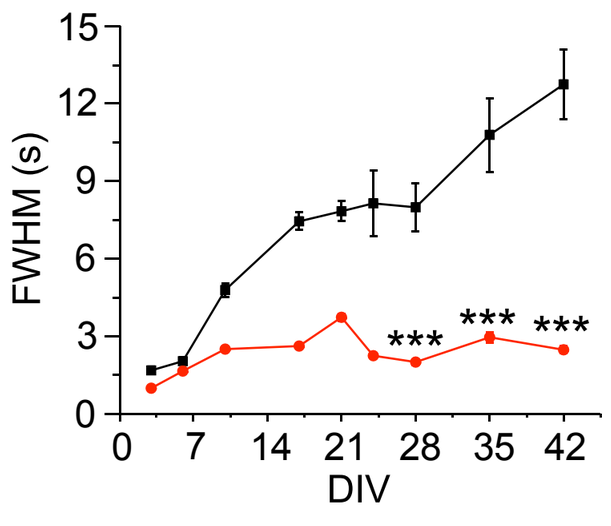
FWHM (s)
DIV
***
***
***

A

jGCaMP7b

jGCaMP7b-X_C

DIV 7

DIV 35

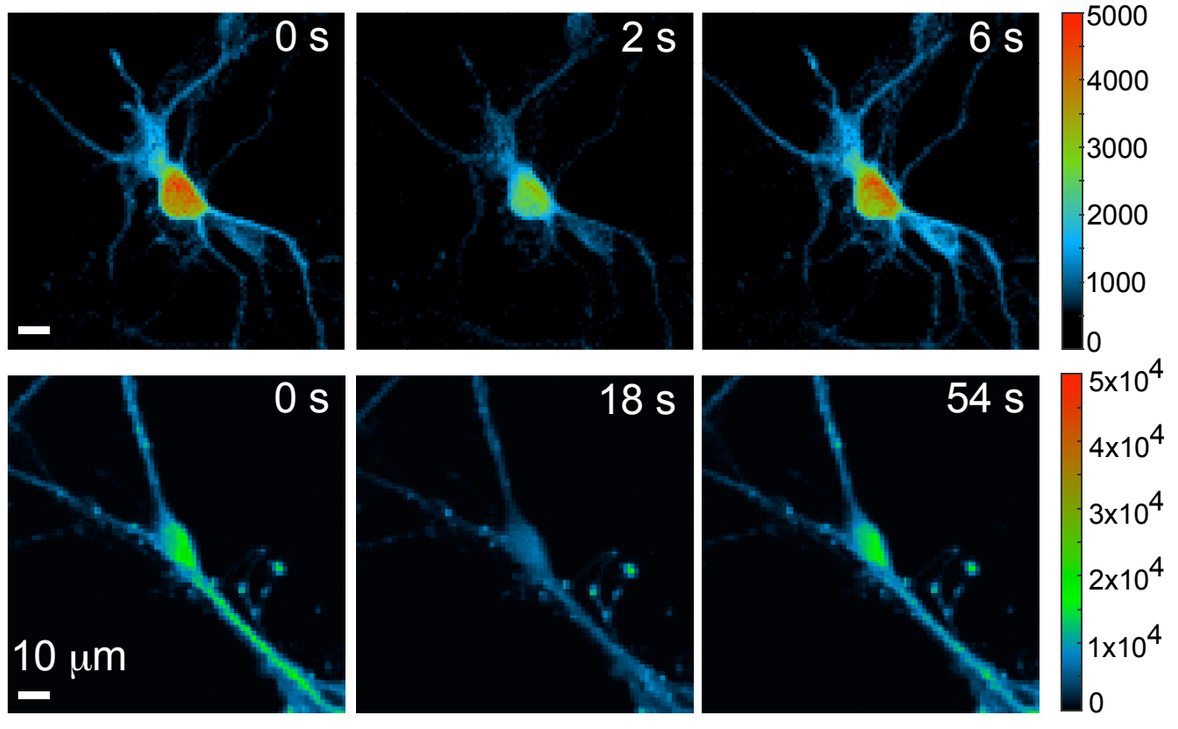

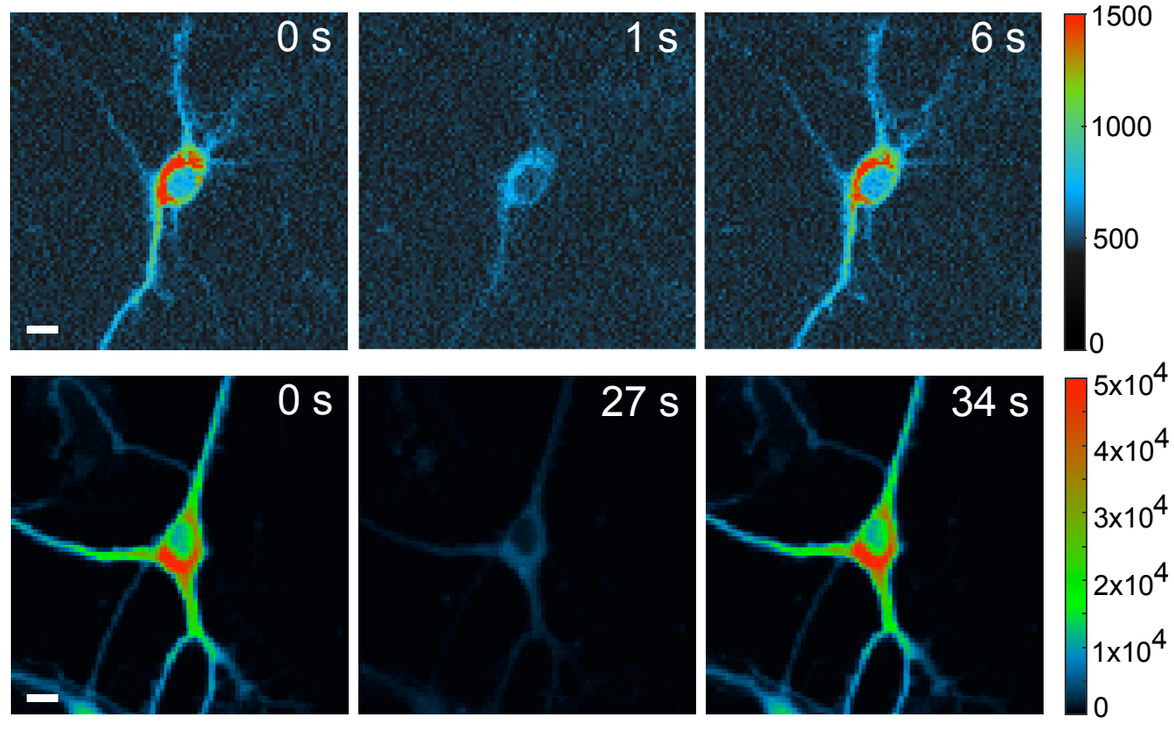

B

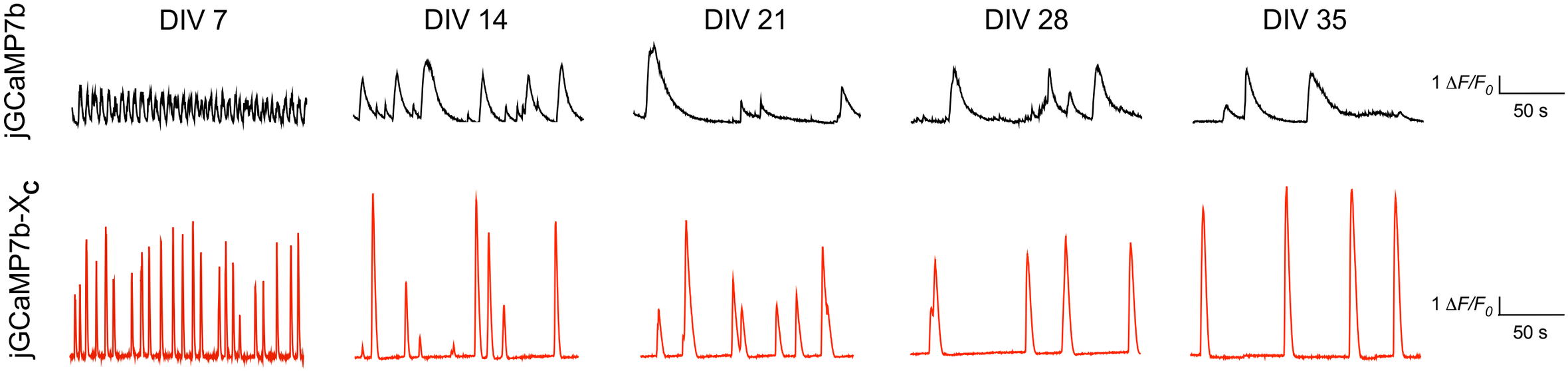

C

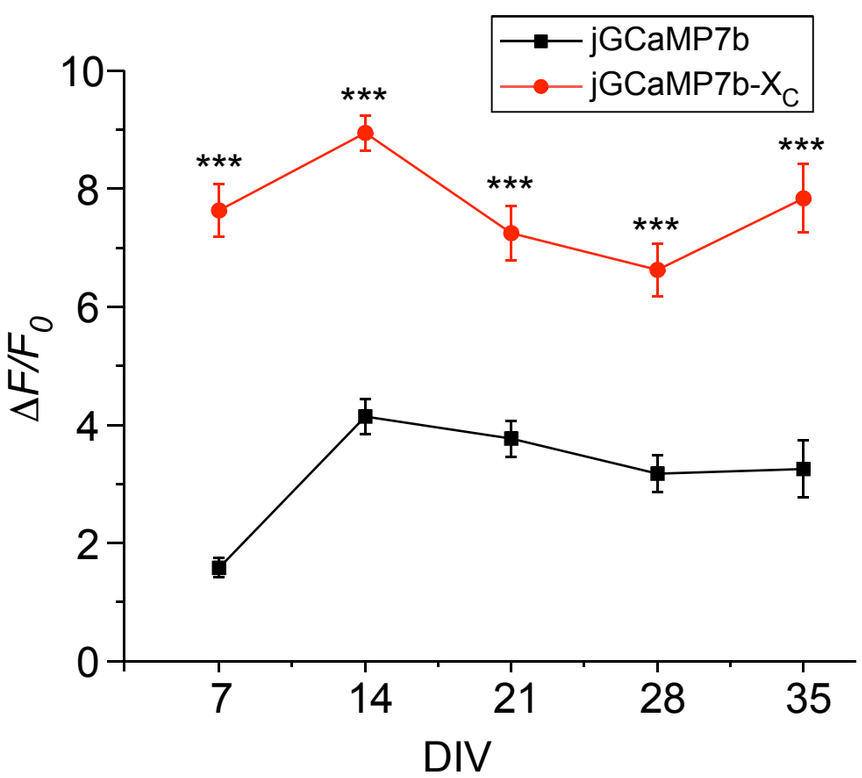

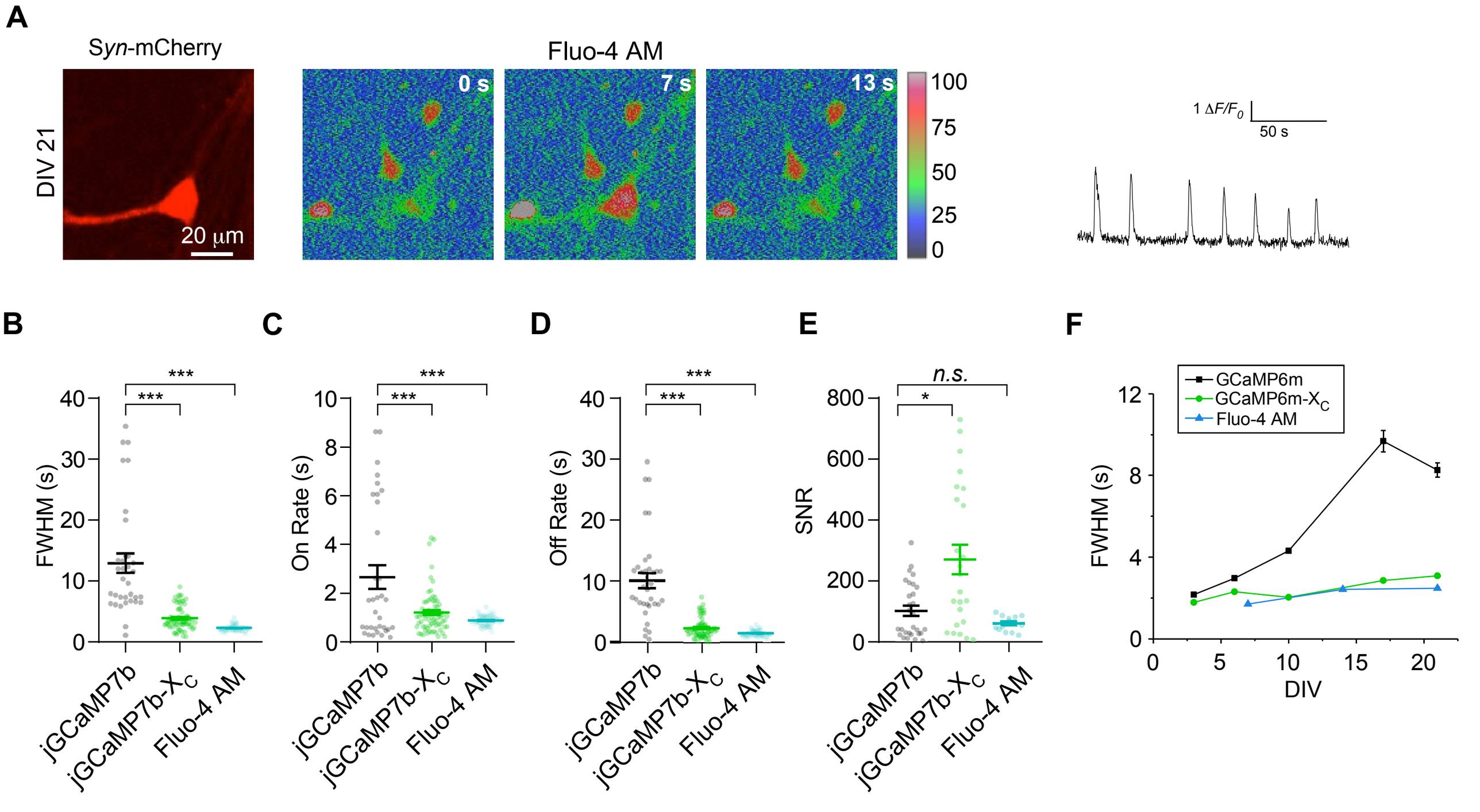
A
Syn-mCherry
DIV 21
20 μm
Fluo-4 AM
0 s
7 s
13 s
100
75
50
25
0
1 ΔF/F0
50 s
B
FWHM (s)
jGCaMP7b
jGCaMP7b-XC
Fluo-4 AM
C
On Rate (s)
D
Off Rate (s)
E
SNR
n.s.
F
GCaMP6m
GCaMP6m-XC
Fluo-4 AM
DIV

A

GCaMP6m

DIV 3 DIV 6 DIV 10 DIV 17 DIV 21 DIV 24 DIV 28

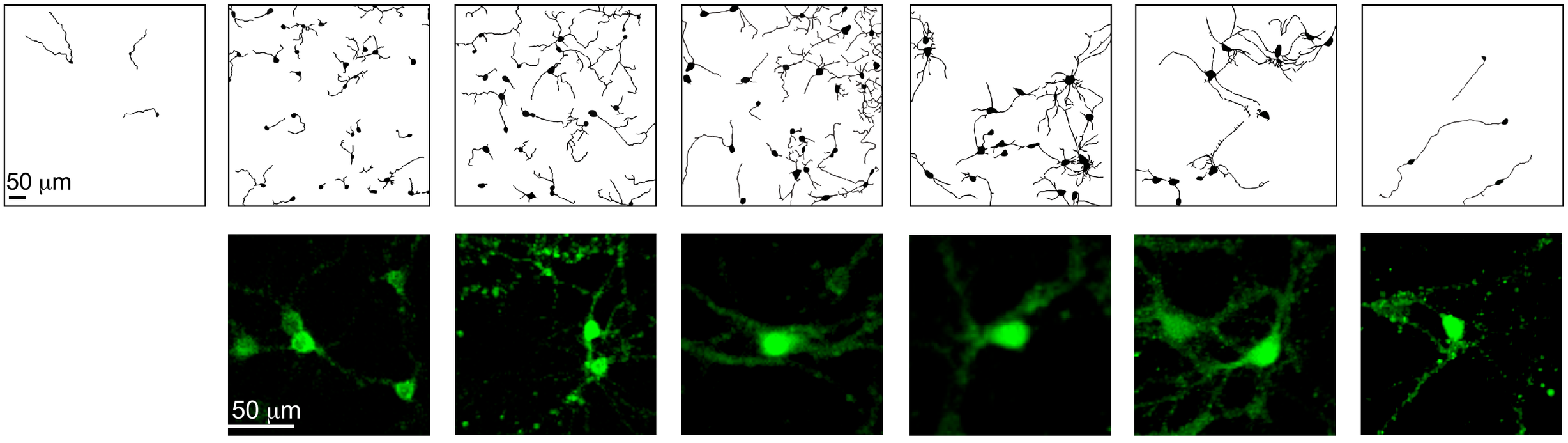

GCaMP6m-X_C

DIV 3 DIV 6 DIV 10 DIV 17 DIV 21 DIV 24 DIV 28

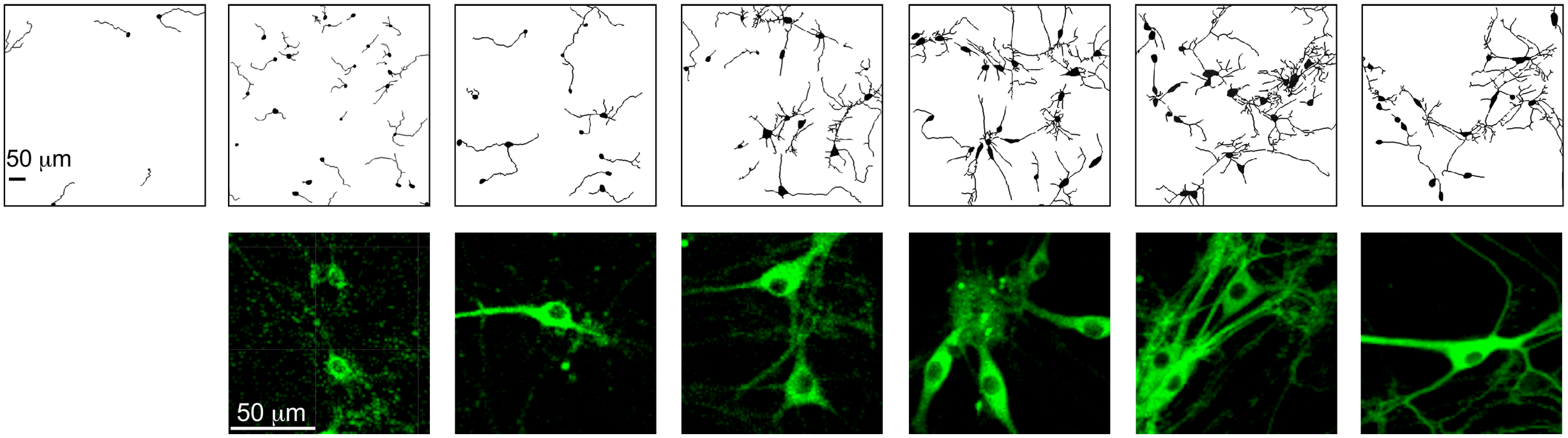

B

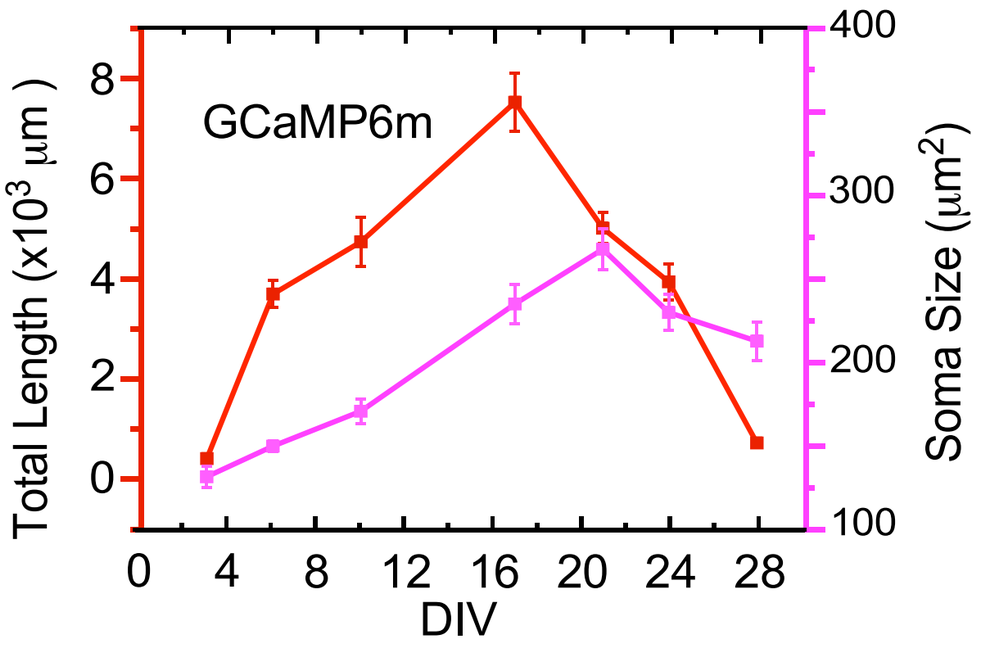

C

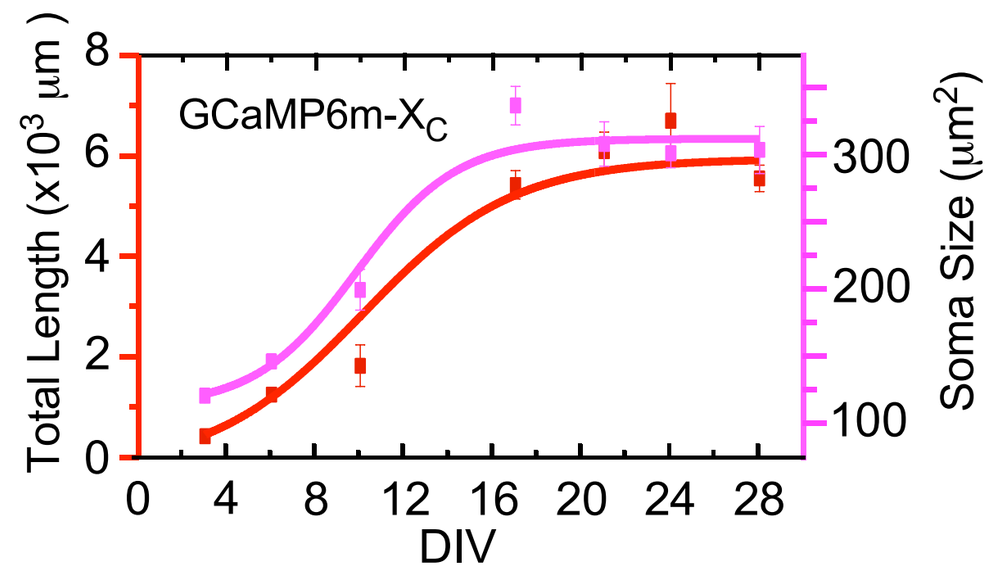

D

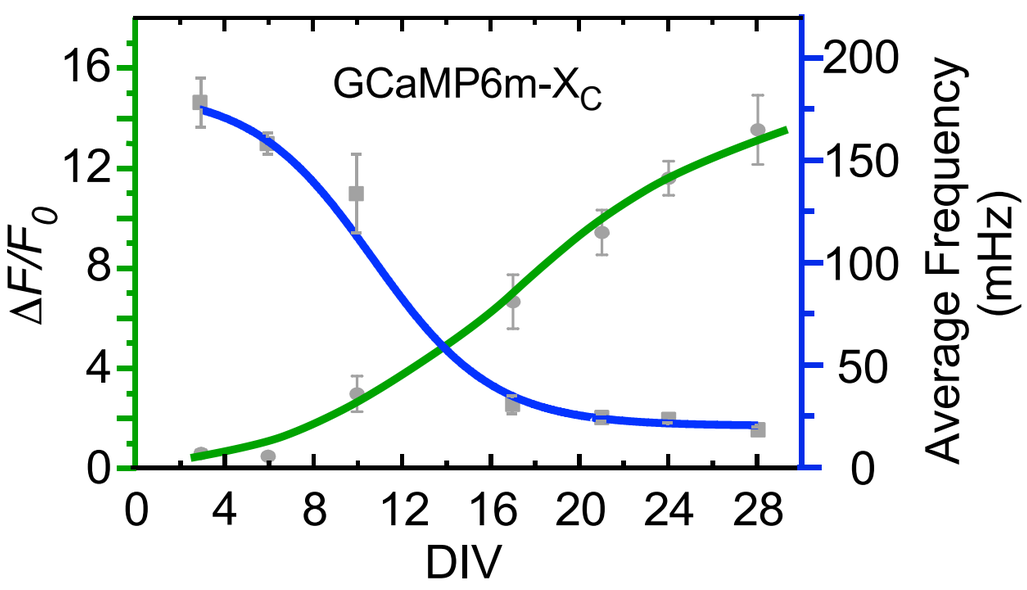

E

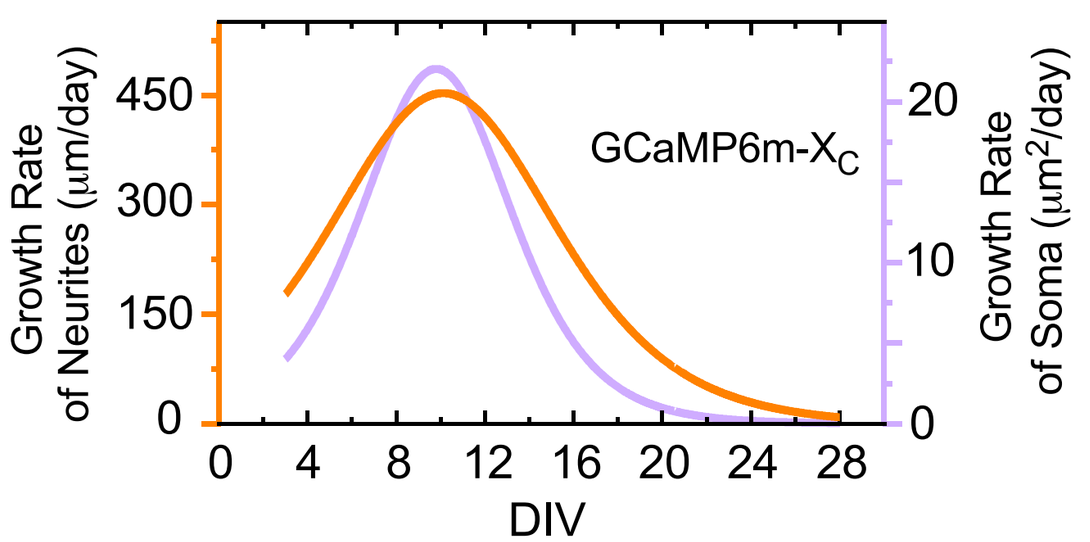

A

DIV 28 DIV 35 DIV 42

DIV 28 DIV 35 DIV 42

AAV-*Syn*-GFP

AAV-*Syn*-GCaMP6m

AAV-*Syn*-GCaMP6m-X_c

100 μm

20 μm

B

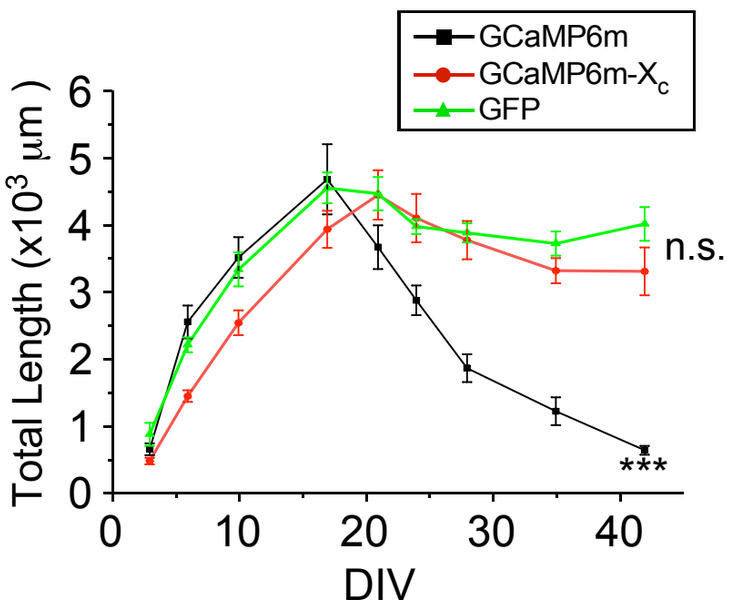

C

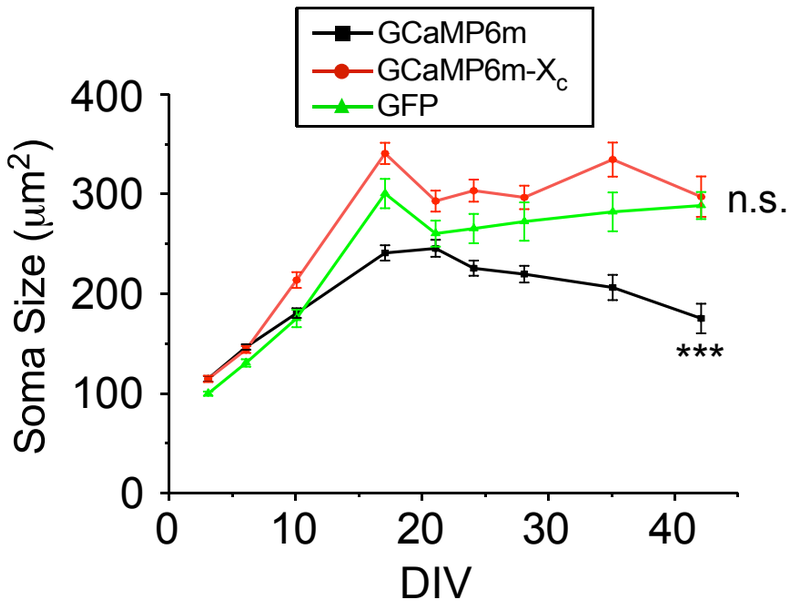

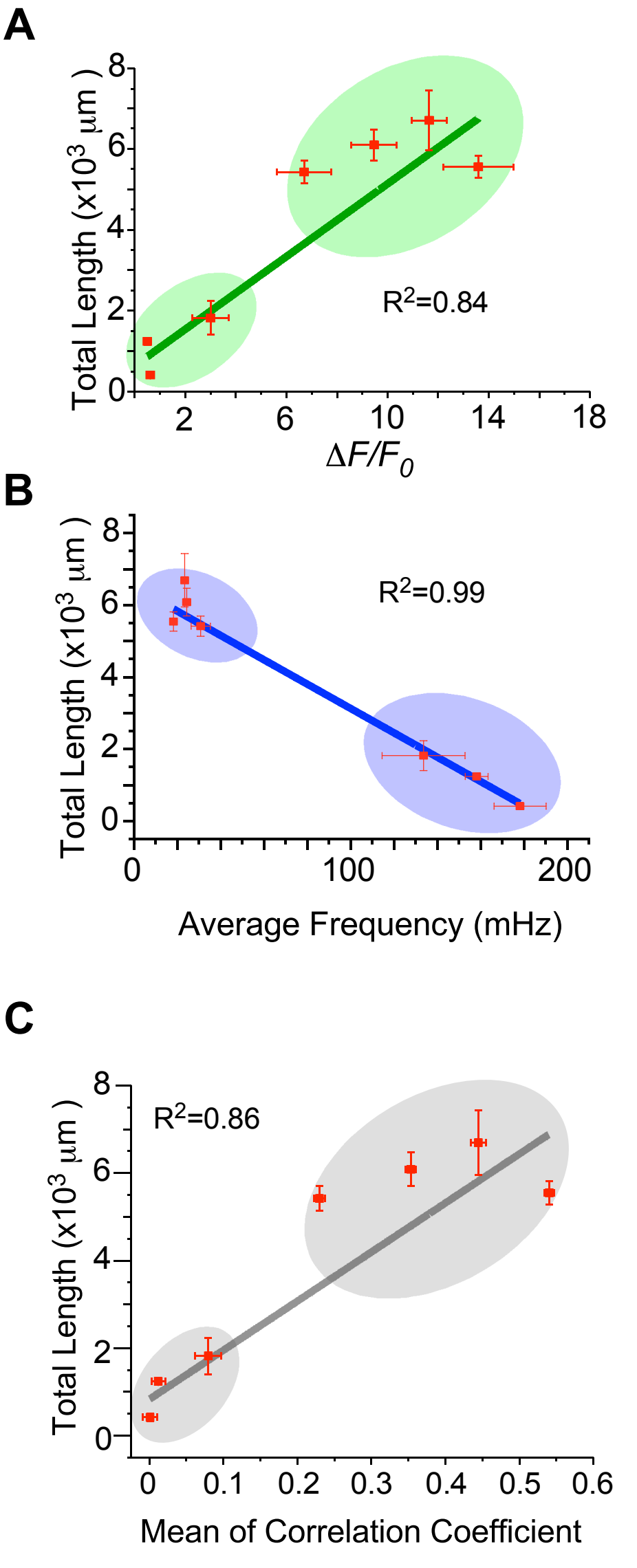
A
Total Length (x10^3 μm)
8
6
4
2
0
2
6
10
14
18
$\Delta F/F_0$
R^2=0.84
B
Total Length (x10^3 μm)
8
6
4
2
0
0
100
200
Average Frequency (mHz)
R^2=0.99
C
Total Length (x10^3 μm)
8
6
4
2
0
0
0.1
0.2
0.3
0.4
0.5
0.6
Mean of Correlation Coefficient
R^2=0.86

A

DIV 7 DIV 14 DIV 21 DIV 28 DIV 35

GFP

100 μm

jGCaMP7b

10 μm

jGCaMP7b-X_C

B

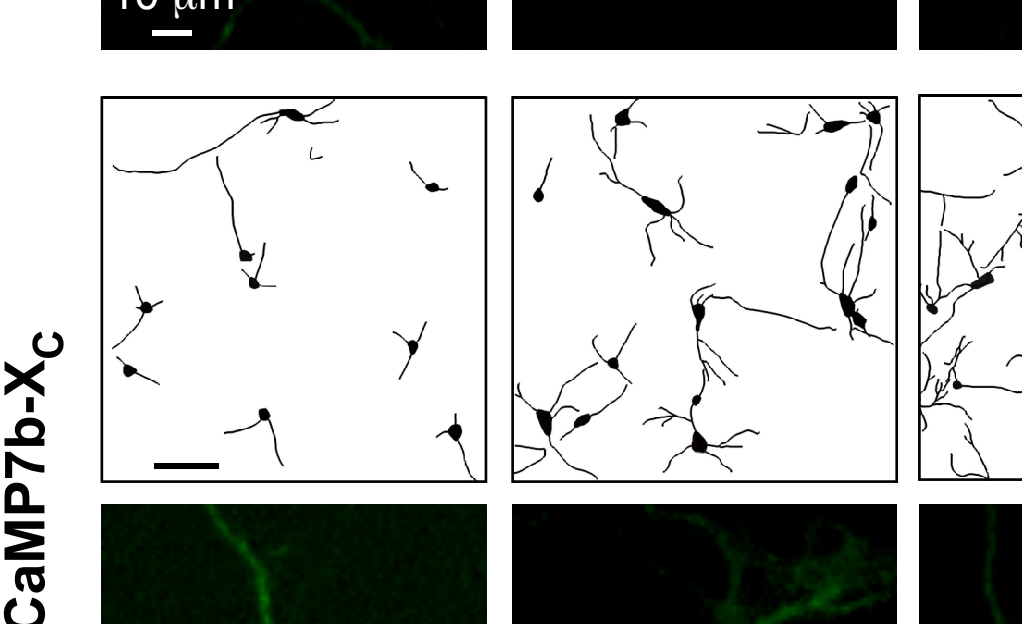

C

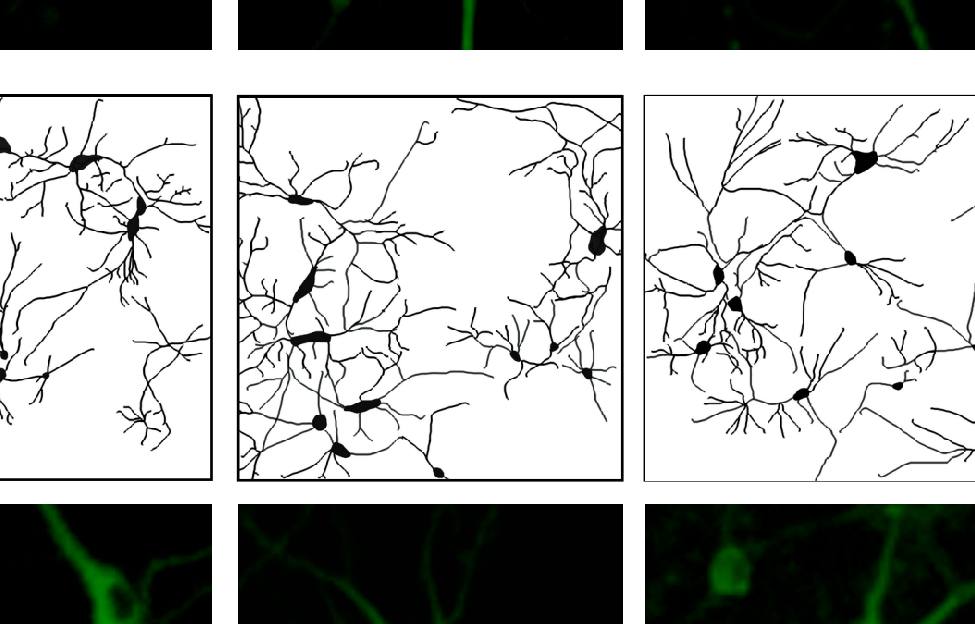

A

Cortical neuron

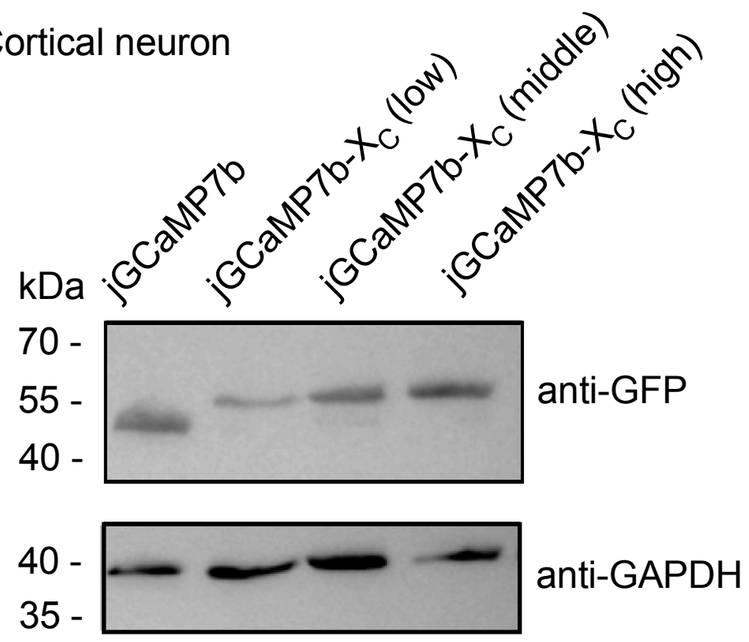

B

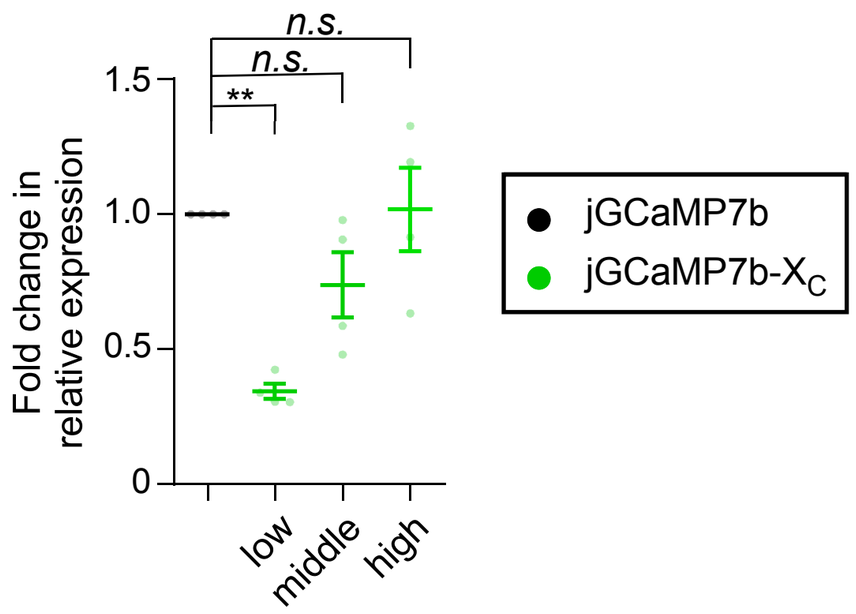

C

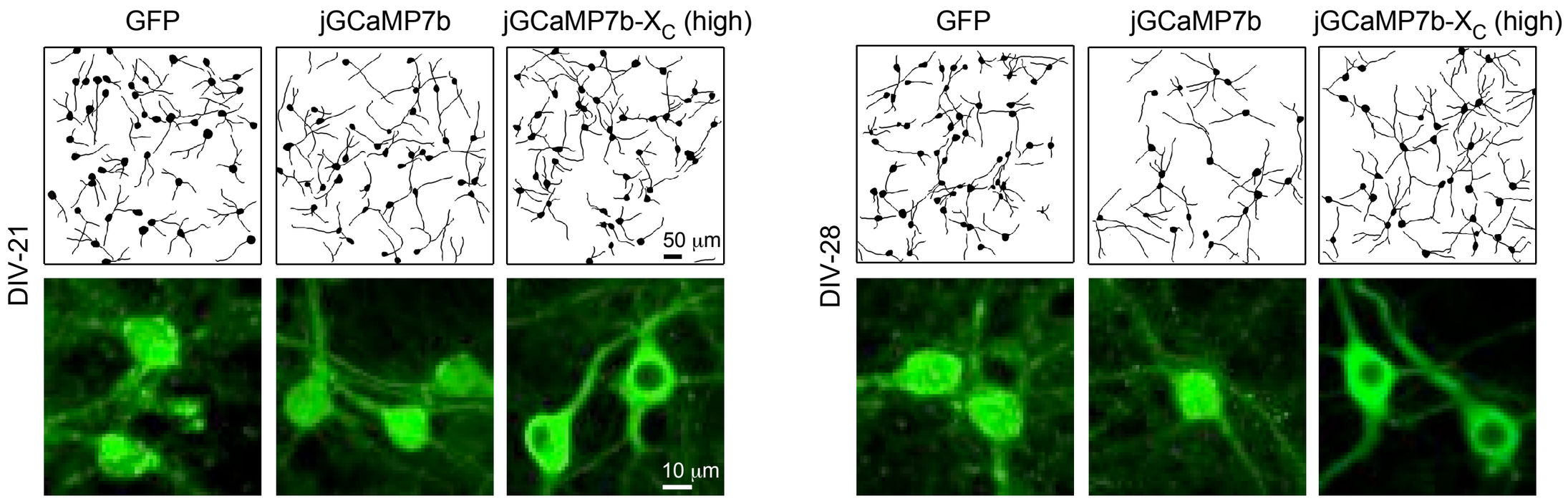

D

E

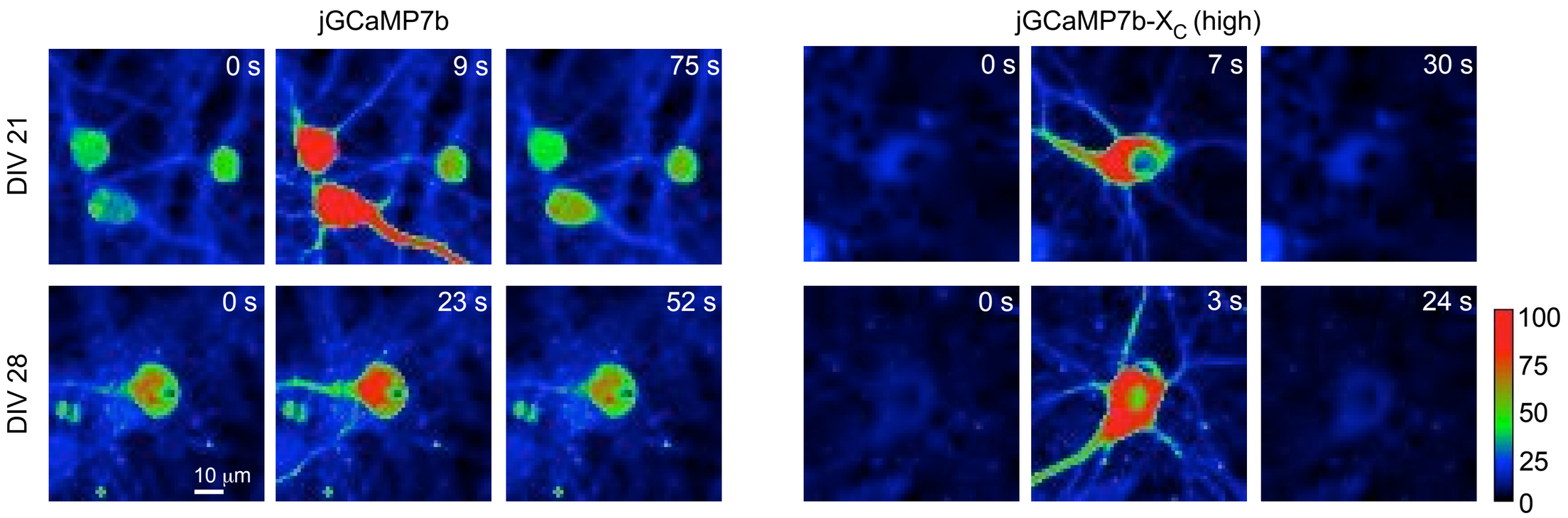

F

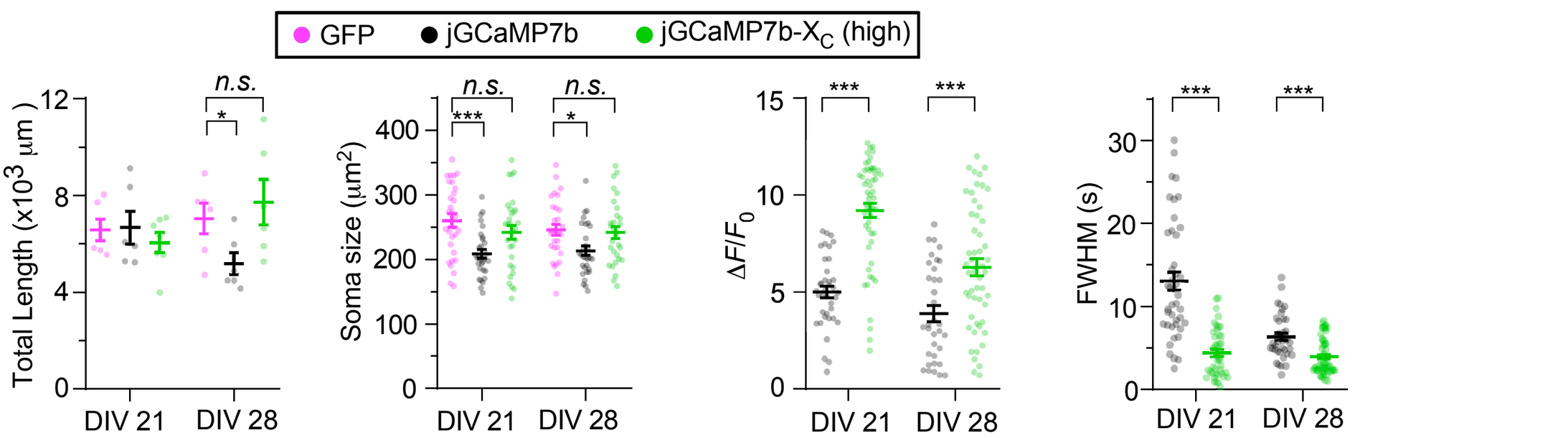

A

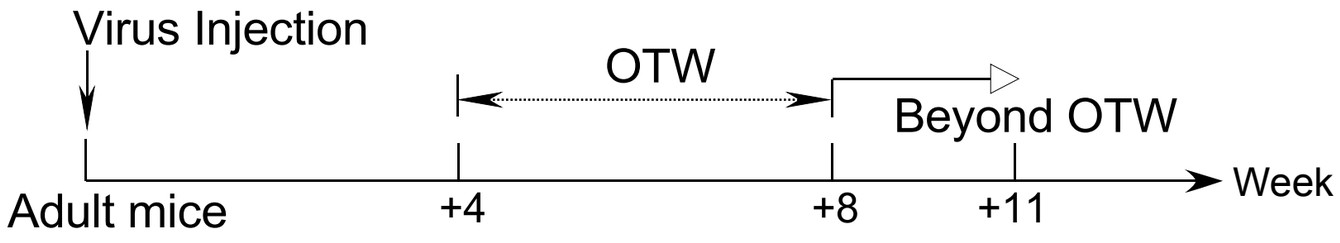

AAV-*Syn*-GCaMP6m
4 weeks

AAV-*Syn*-GCaMP6m-X_C
4 weeks

AAV-*Syn*-GCaMP6m
8 weeks

AAV-*Syn*-GCaMP6m-X_C
11 weeks

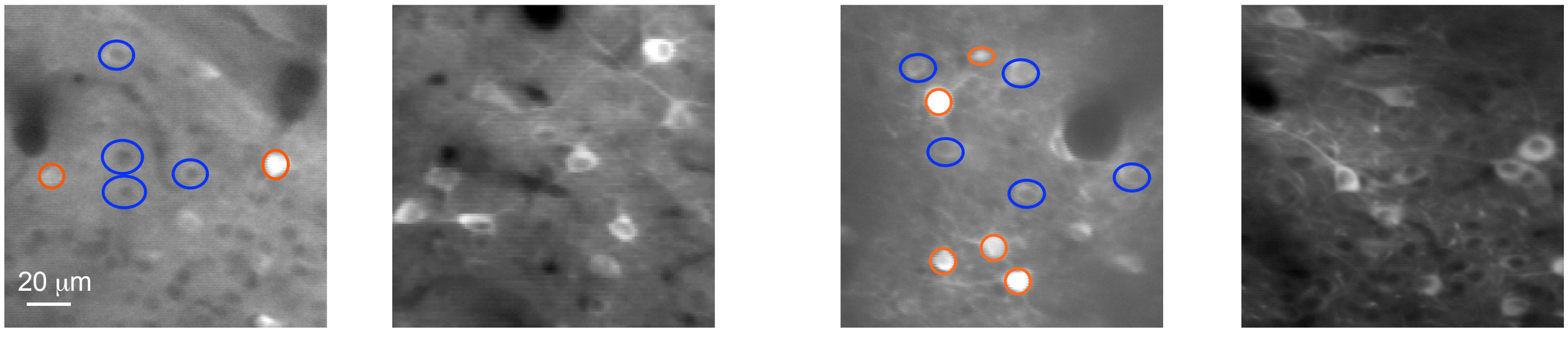

B

Nucleus-filled **Nucleus-excluded** **GCaMP-X** **Nucleus-filled** **Nucleus-excluded** **GCaMP-X**

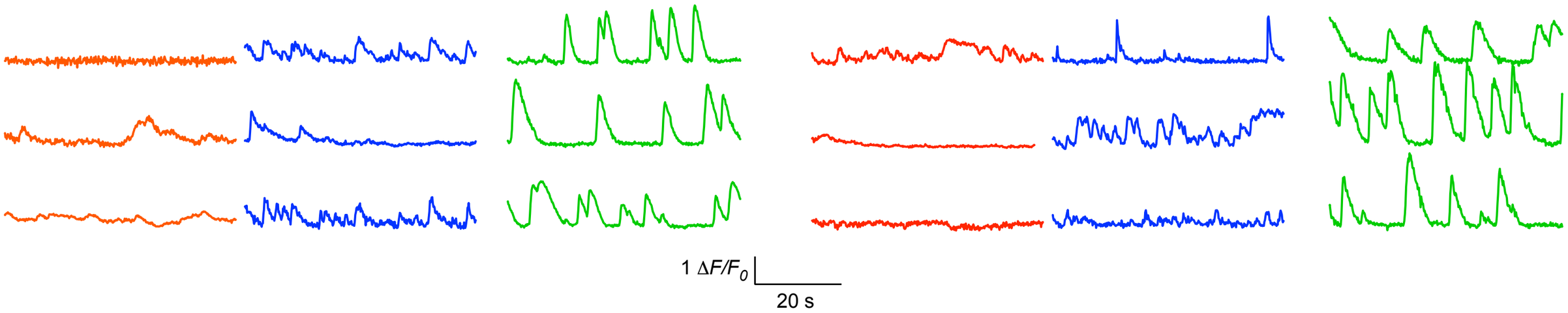

C

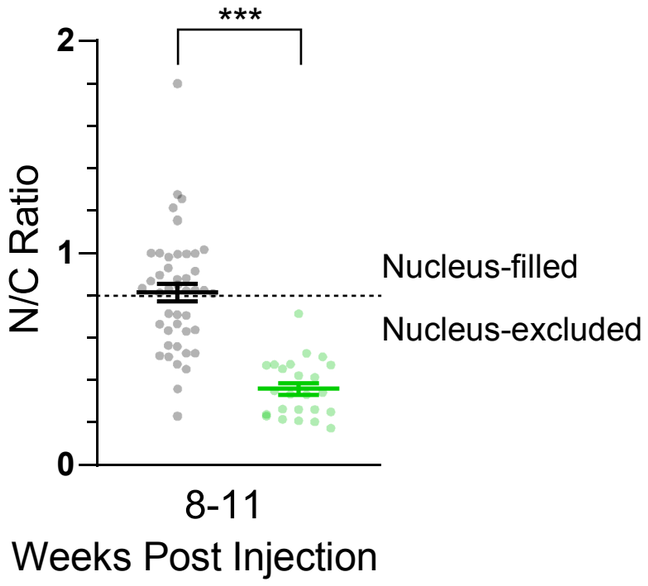

D

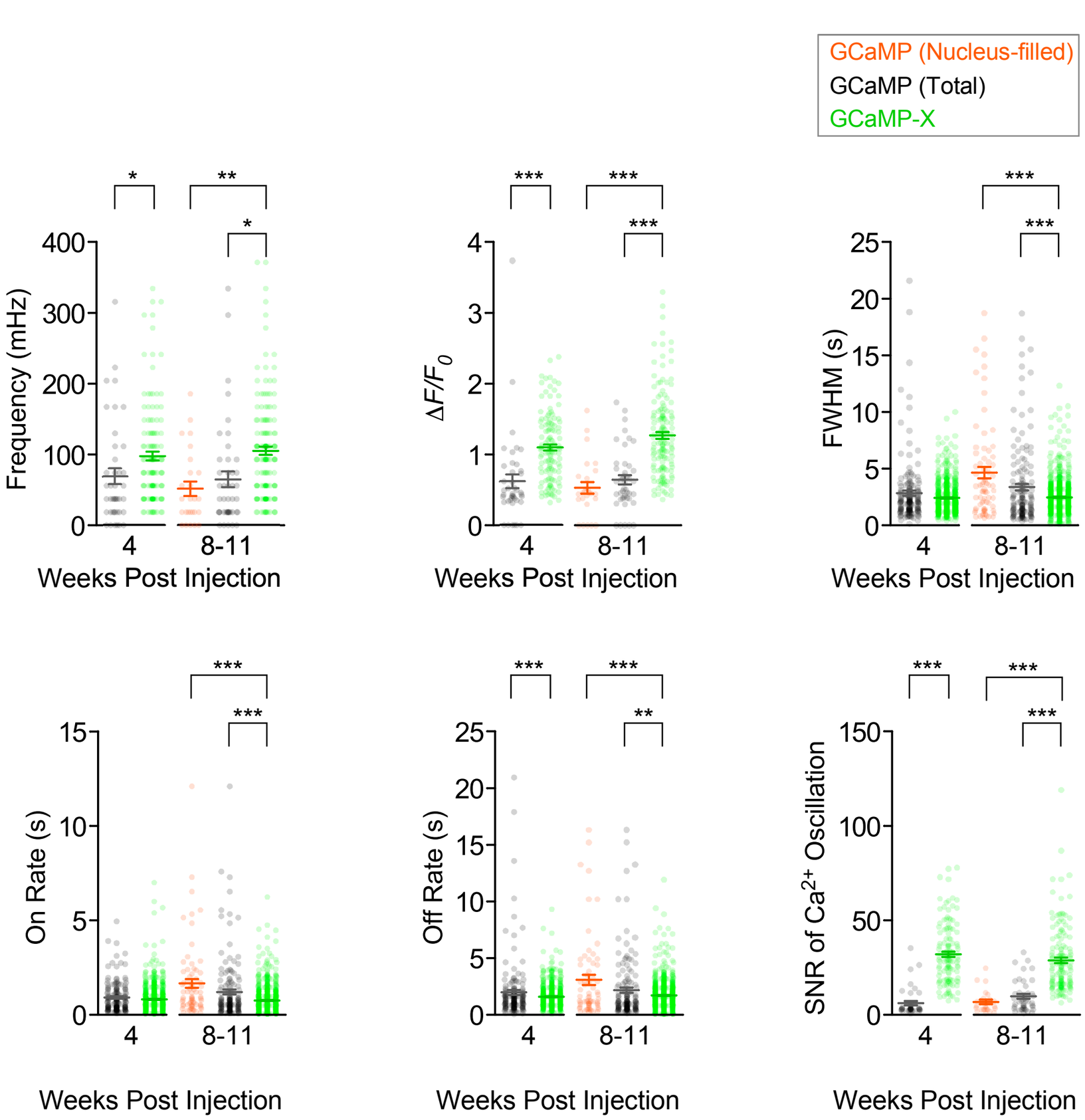

A

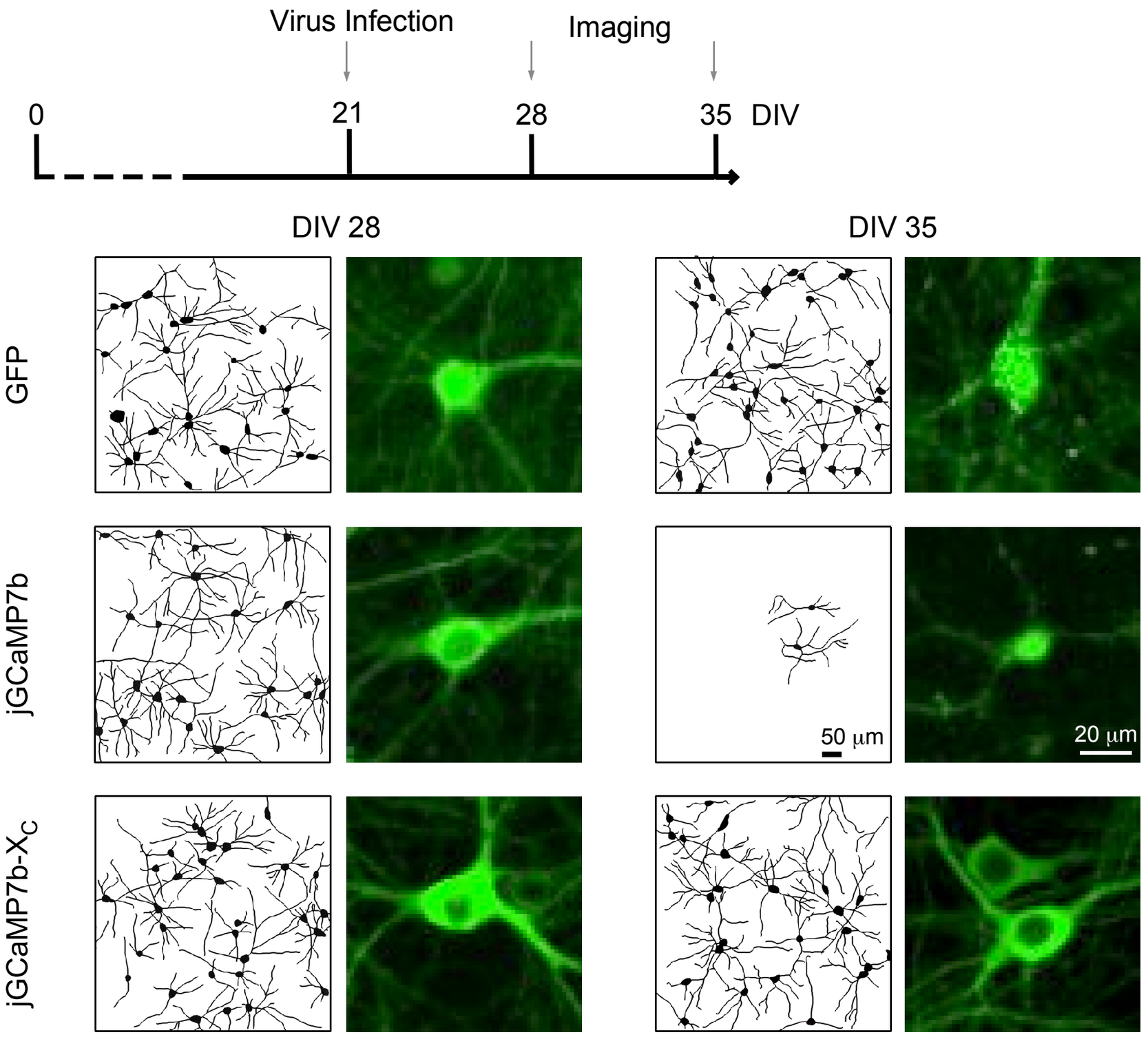
Virus Infection
Imaging
0
21
28
35 DIV
DIV 28
DIV 35
GFP
jGCaMP7b
jGCaMP7b-X_C
50 μm
20 μm

B

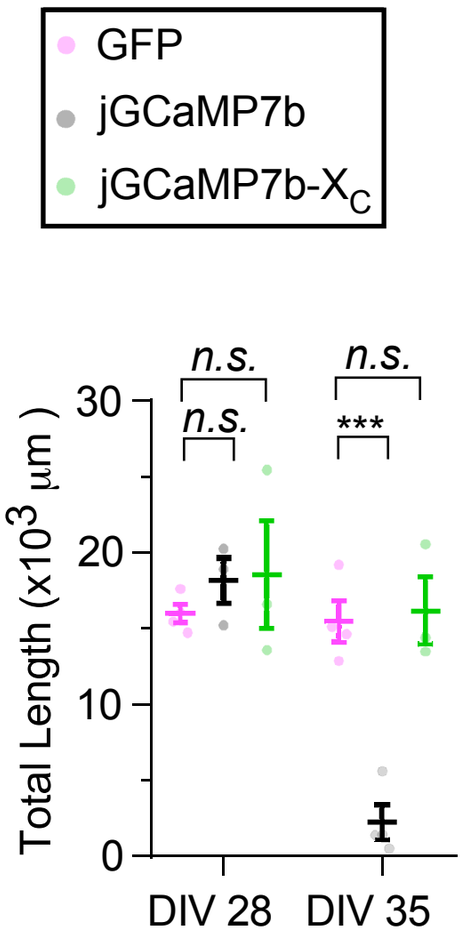
GFP
jGCaMP7b
jGCaMP7b-X_C
n.s.
n.s.
n.s.
***
Total Length (x10^3 μm)
30
20
10
0
DIV 28
DIV 35

C

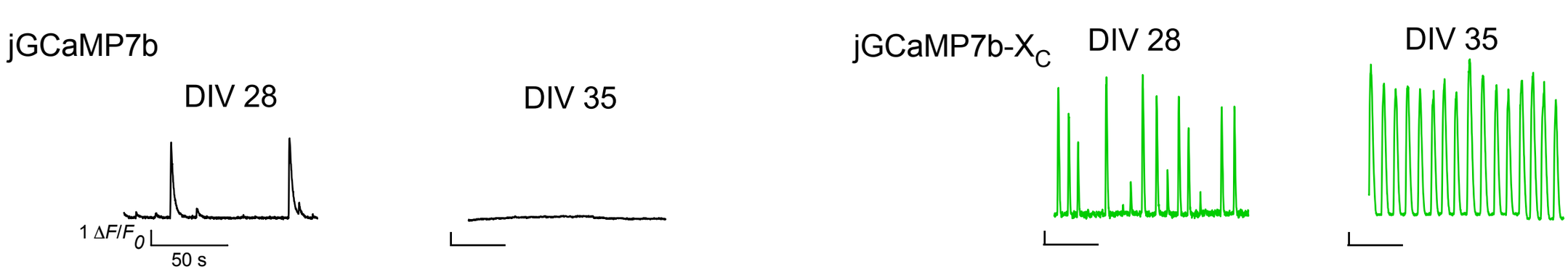
jGCaMP7b
DIV 28
DIV 35
jGCaMP7b-X_C
DIV 28
DIV 35
1 ΔF/F_0
50 s

D

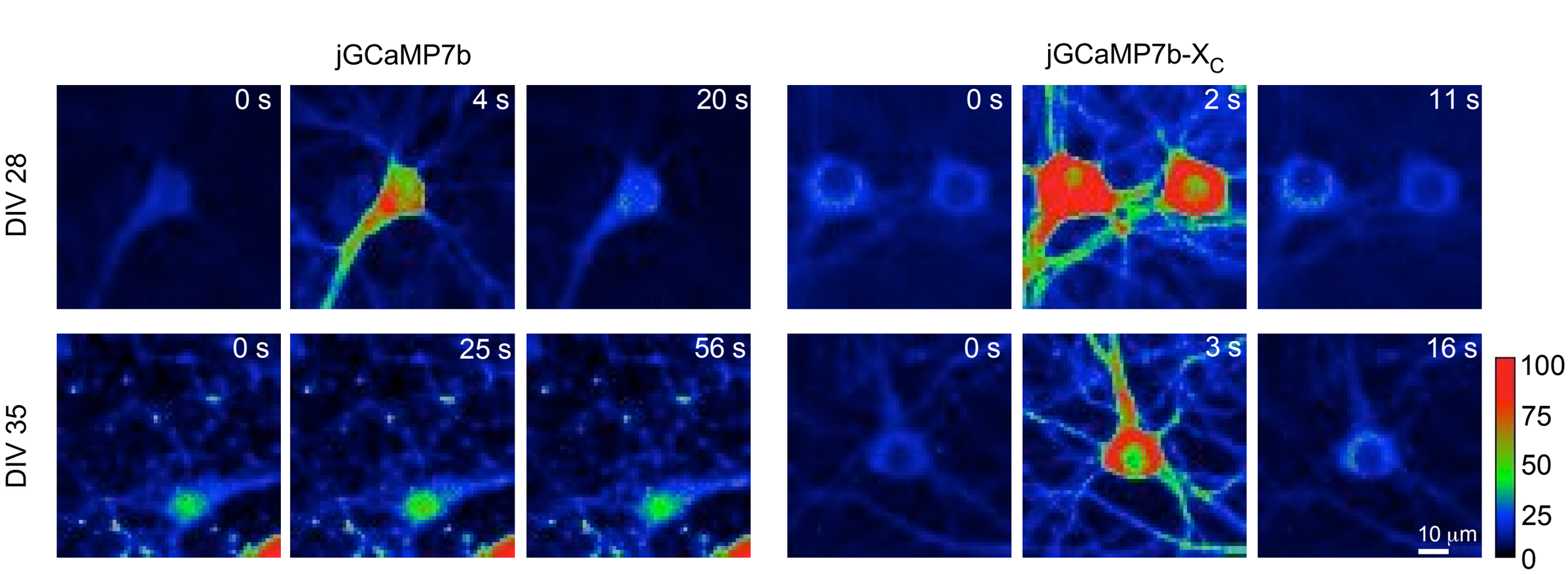
jGCaMP7b
jGCaMP7b-X_C
DIV 28
DIV 35
0 s
4 s
20 s
0 s
2 s
11 s
0 s
25 s
56 s
0 s
3 s
16 s
10 μm
100
75
50
25
0

E

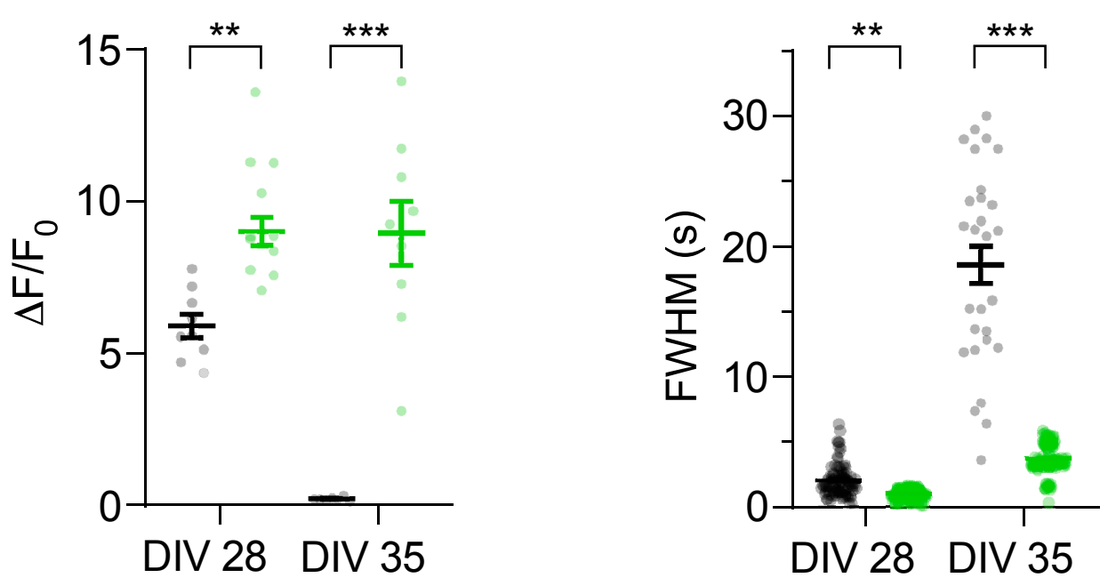
**
***
ΔF/F_0
15
10
5
0
DIV 28
DIV 35
**
***
FWHM (s)
30
20
10
0
DIV 28
DIV 35

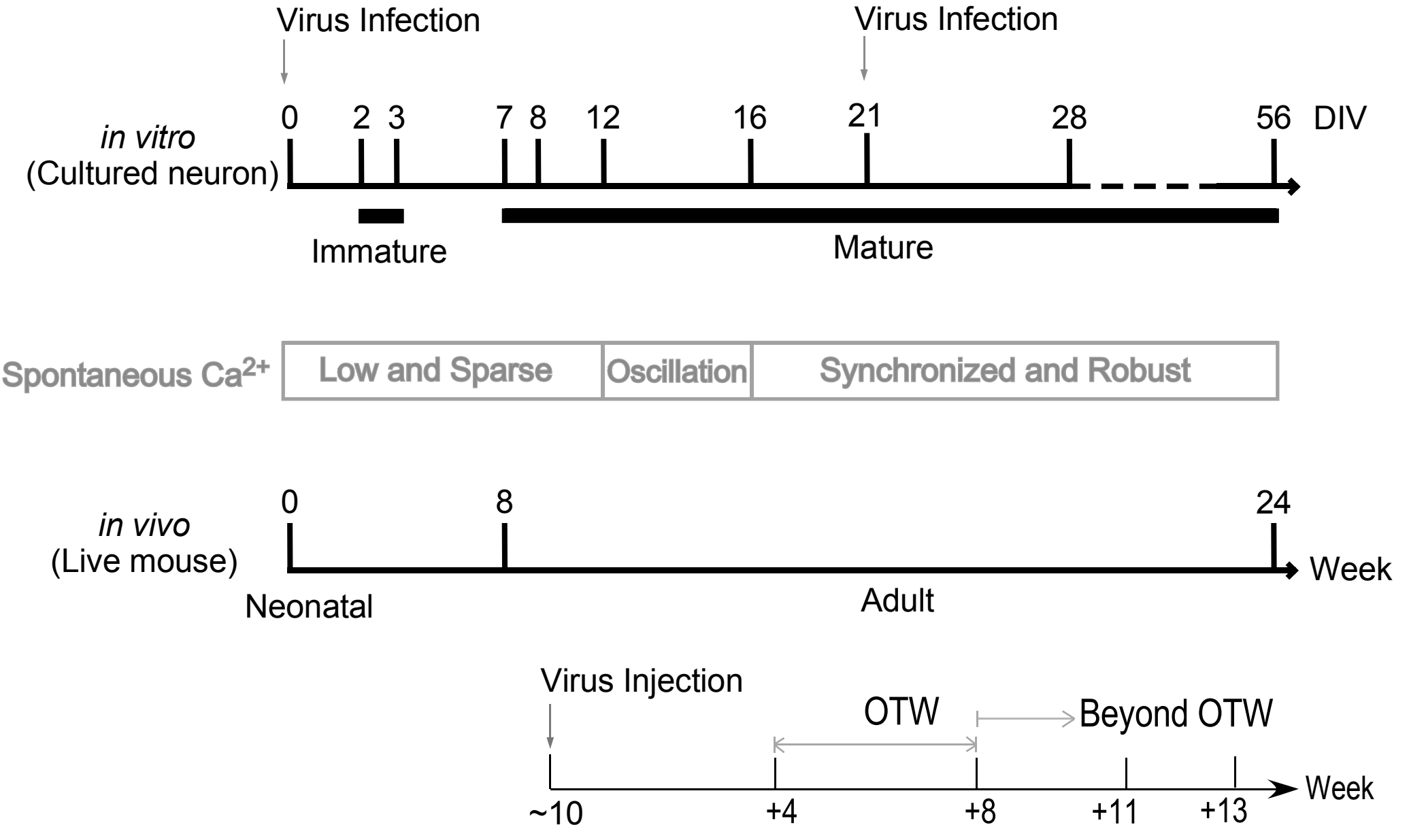
Virus Infection
Virus Infection
in vitro
(Cultured neuron)
0
2
3
7
8
12
16
21
28
56
DIV
Immature
Mature
Spontaneous Ca2+
Low and Sparse
Oscillation
Synchronized and Robust
in vivo
(Live mouse)
0
8
24
Week
Neonatal
Adult
Virus Injection
OTW
Beyond OTW
Week
~10
+4
+8
+11
+13

A

3 Weeks Post Injection

GCaMP6m
$1x10^{11}$ v.g/ml
(ALM Area, Left Brain)

GCaMP6m
$5x10^{11}$ v.g/ml
(S1 Area, Left Brain)

GCaMP6m
$1x10^{12}$ v.g/ml
(ALM Area, Right Brain)

GCaMP6m-X_C
$1x10^{12}$ v.g/ml
(S1 Area, Right Brain)

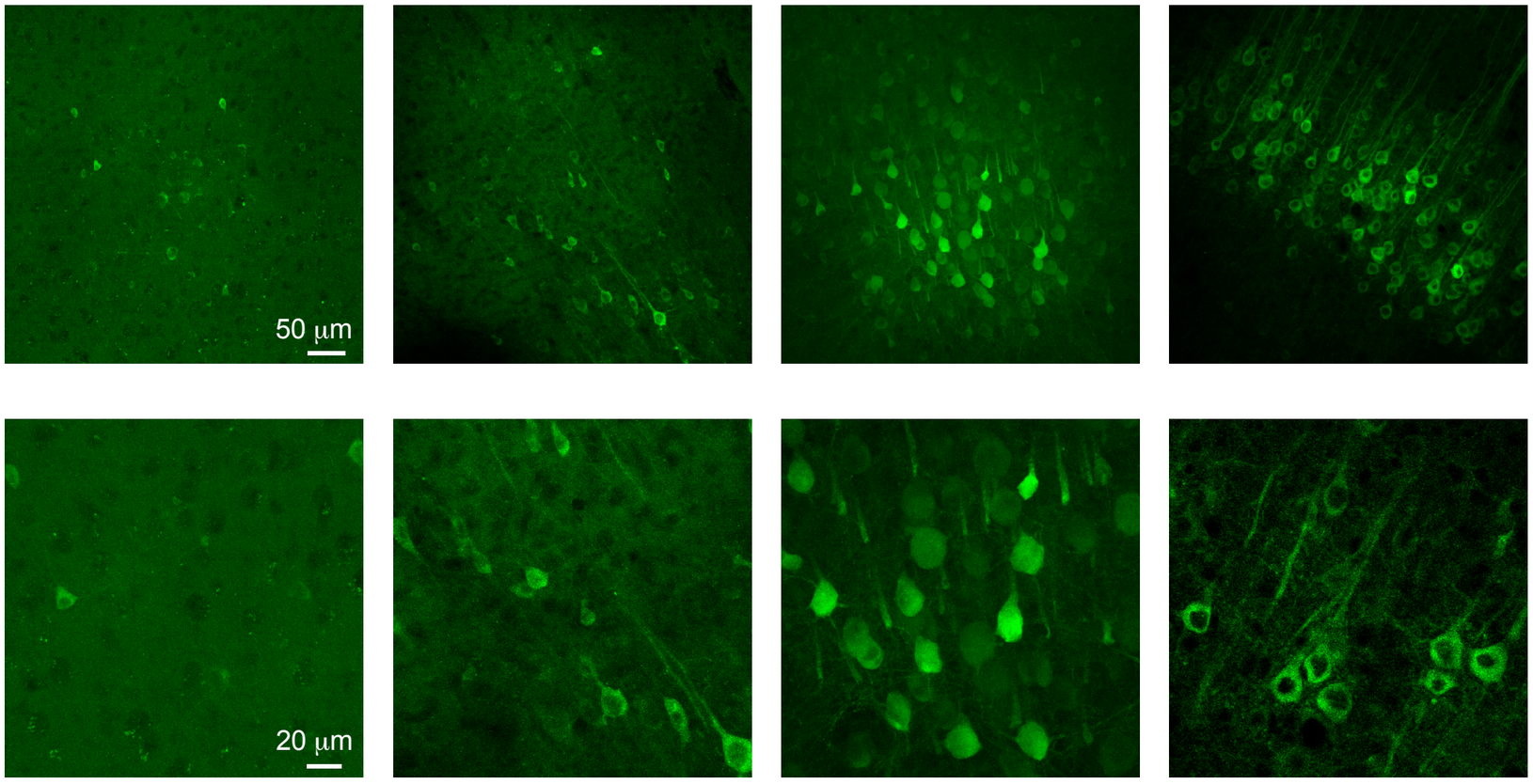

B

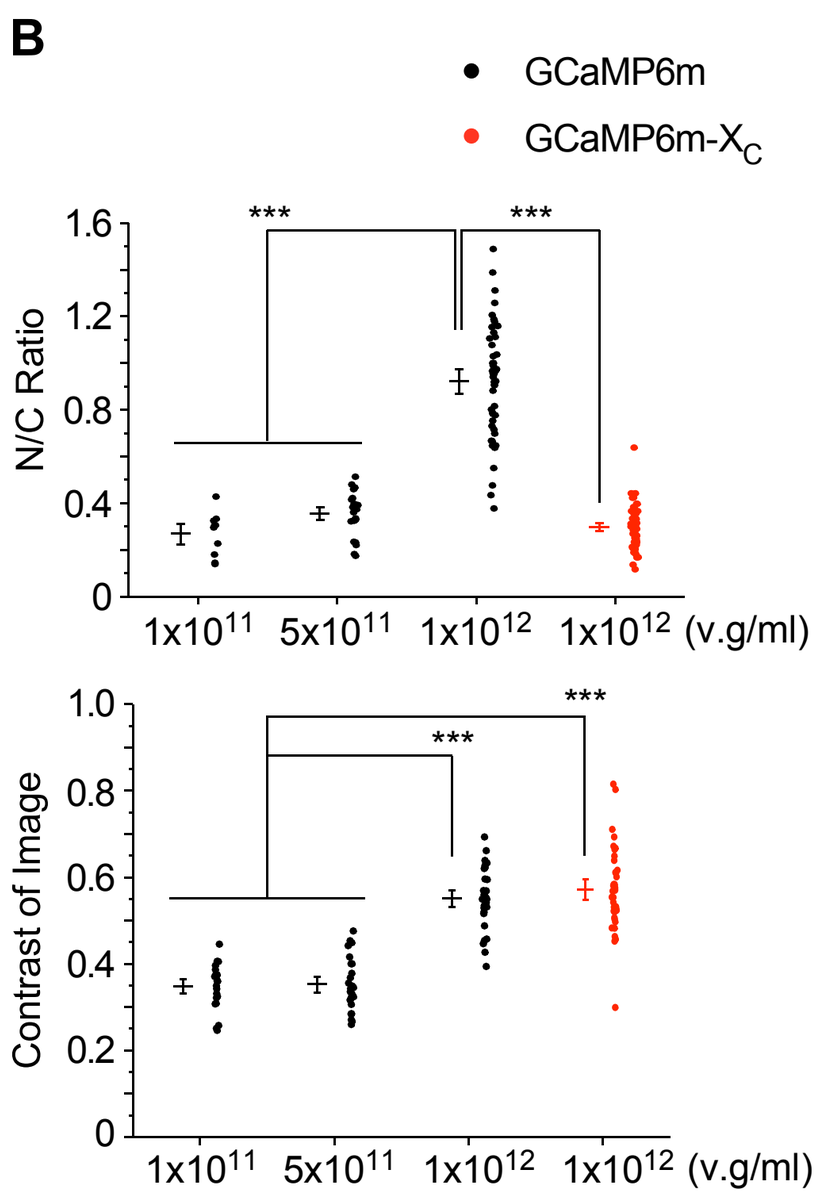

C

17 Days | 55 Days | 70 Days | 92 Days

GCaMP6m S1BF
$1x10^{12}$ v.g/ml

GCaMP6m-X_C S1BF
$1x10^{13}$ v.g/ml

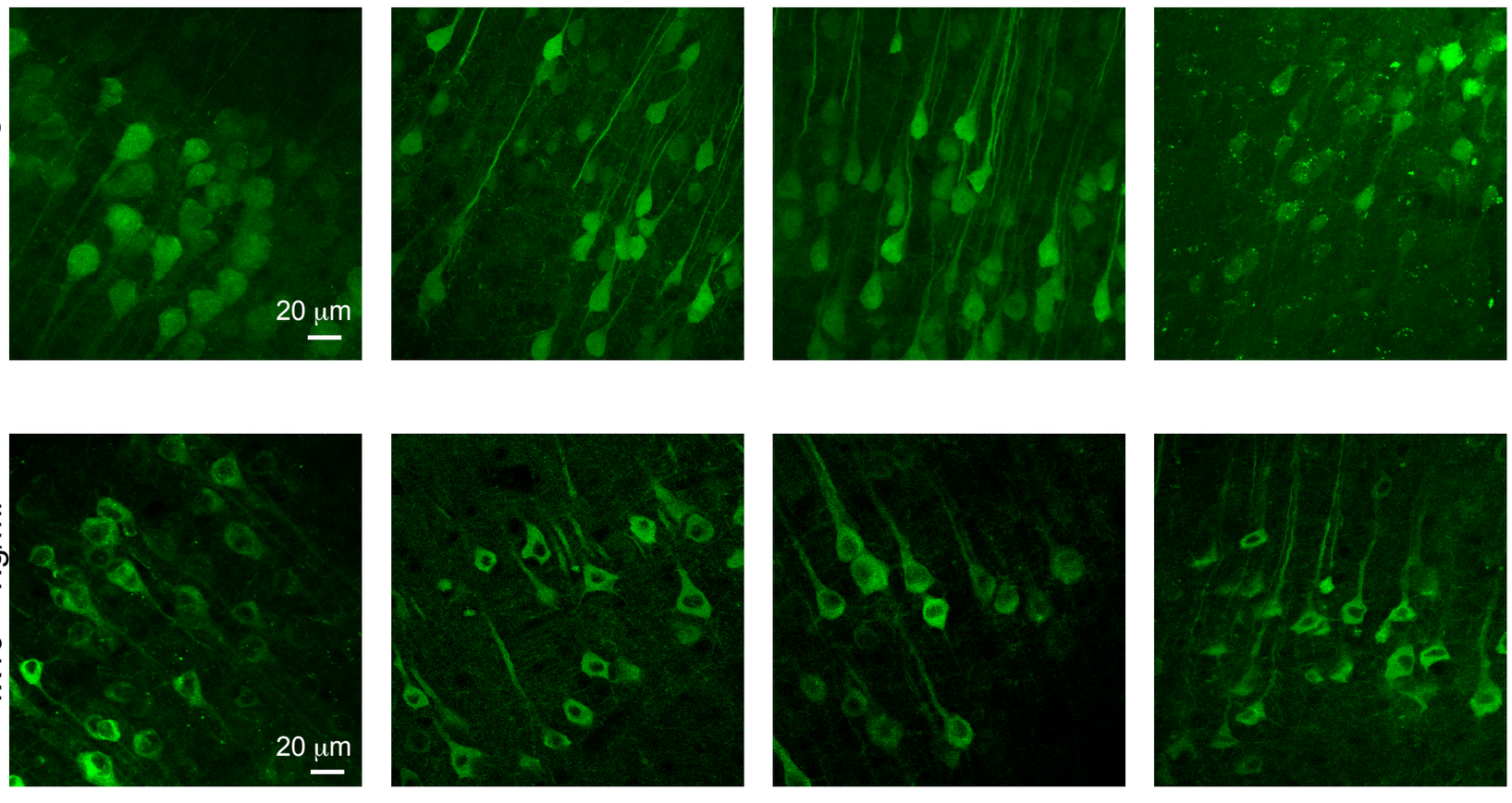

D

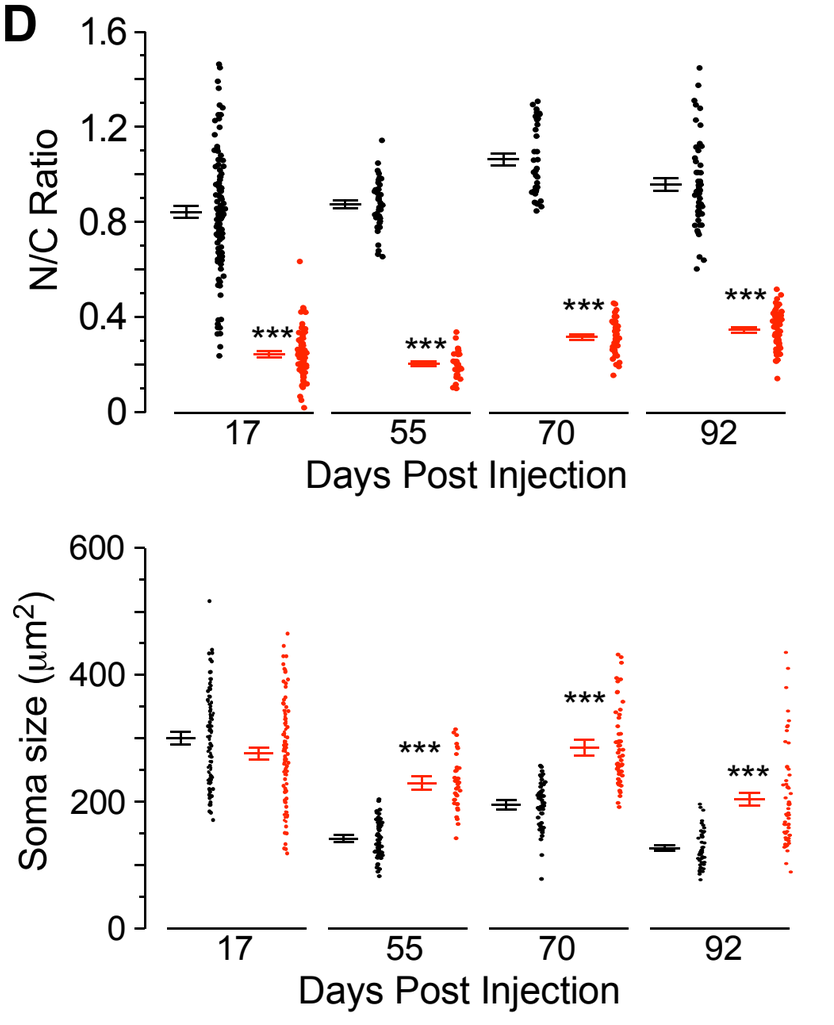

A

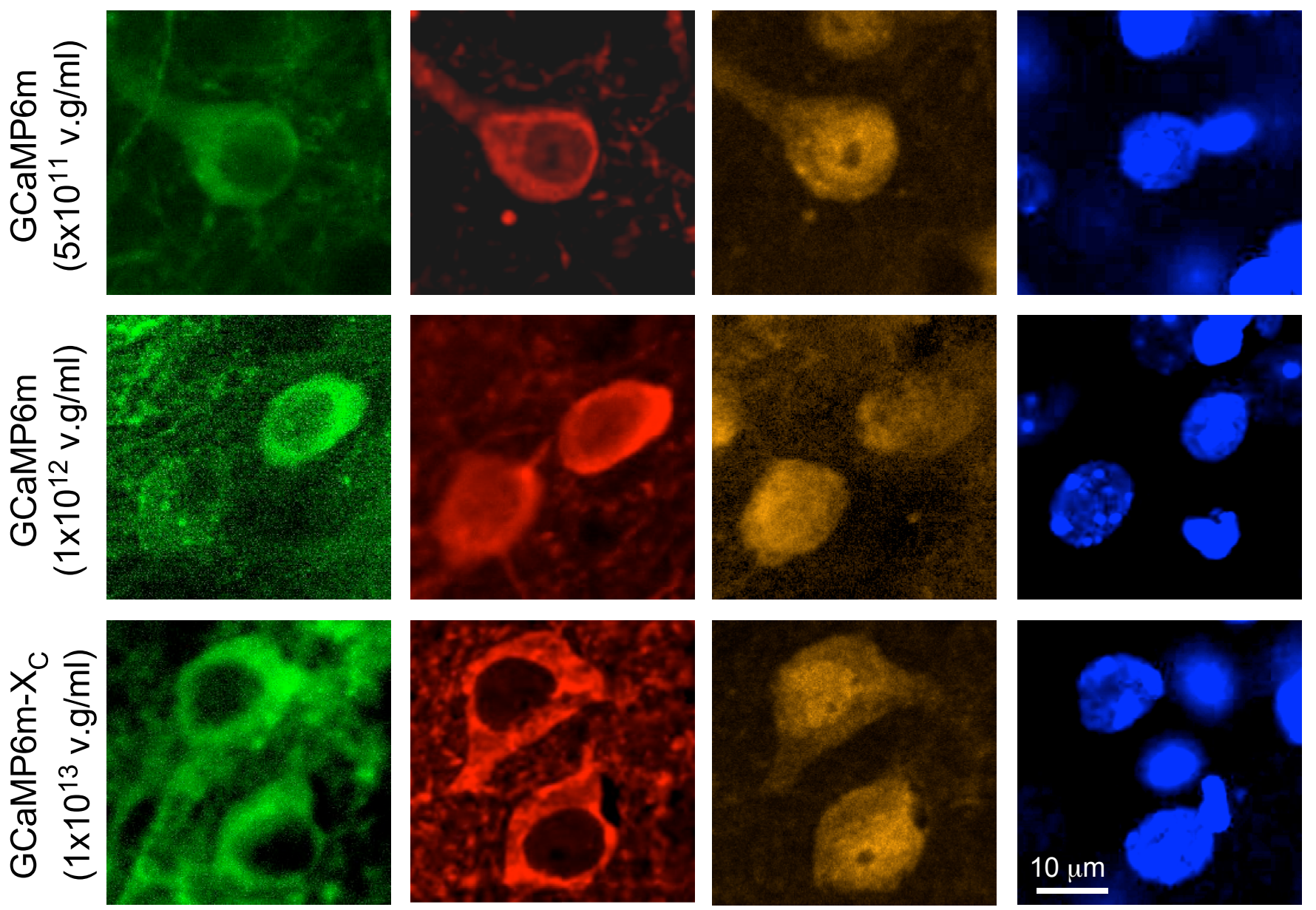
GFP-Channel
Alexa647/
anti-GFP
Alexa568/
NeuN
DAPI
GCaMP6m
(5x10^11 v.g/ml)
GCaMP6m
(1x10^12 v.g/ml)
GCaMP6m-X_C
(1x10^13 v.g/ml)
10 μm

B

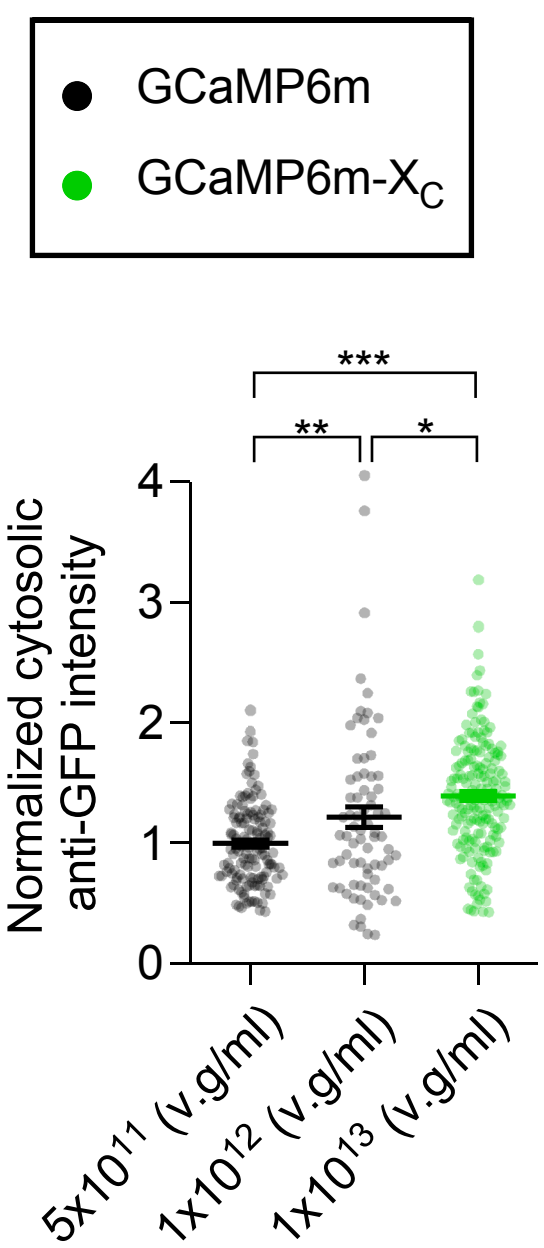
GCaMP6m
GCaMP6m-X_C
***
**
*
Normalized cytosolic
anti-GFP intensity
0
1
2
3
4
5x10^11 (v.g/ml)
1x10^12 (v.g/ml)
1x10^13 (v.g/ml)

C

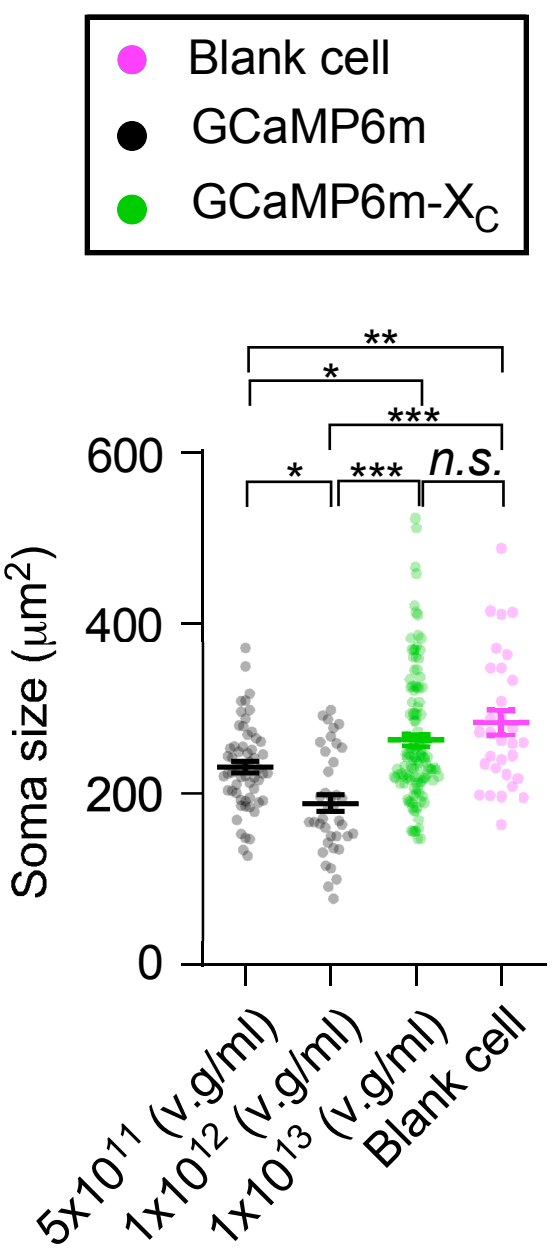
Blank cell
GCaMP6m
GCaMP6m-X_C
**
*
***
*
***
n.s.
Soma size (μm^2)
0
200
400
600
5x10^11 (v.g/ml)
1x10^12 (v.g/ml)
1x10^13 (v.g/ml)
Blank cell

A

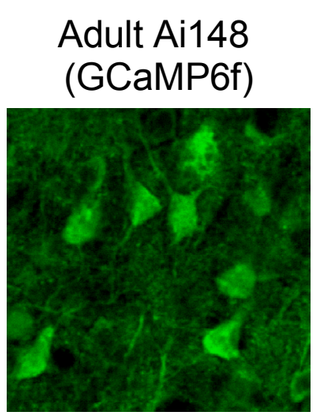
Adult Ai148
(GCaMP6f)

B

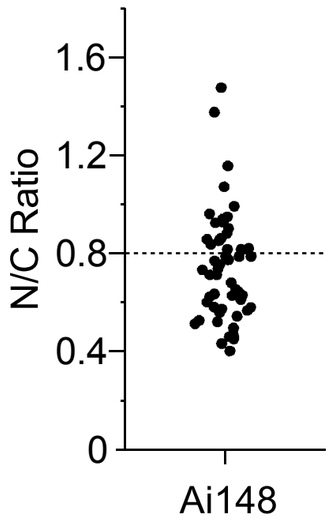
N/C Ratio
1.6
1.2
0.8
0.4
0
Ai148

C

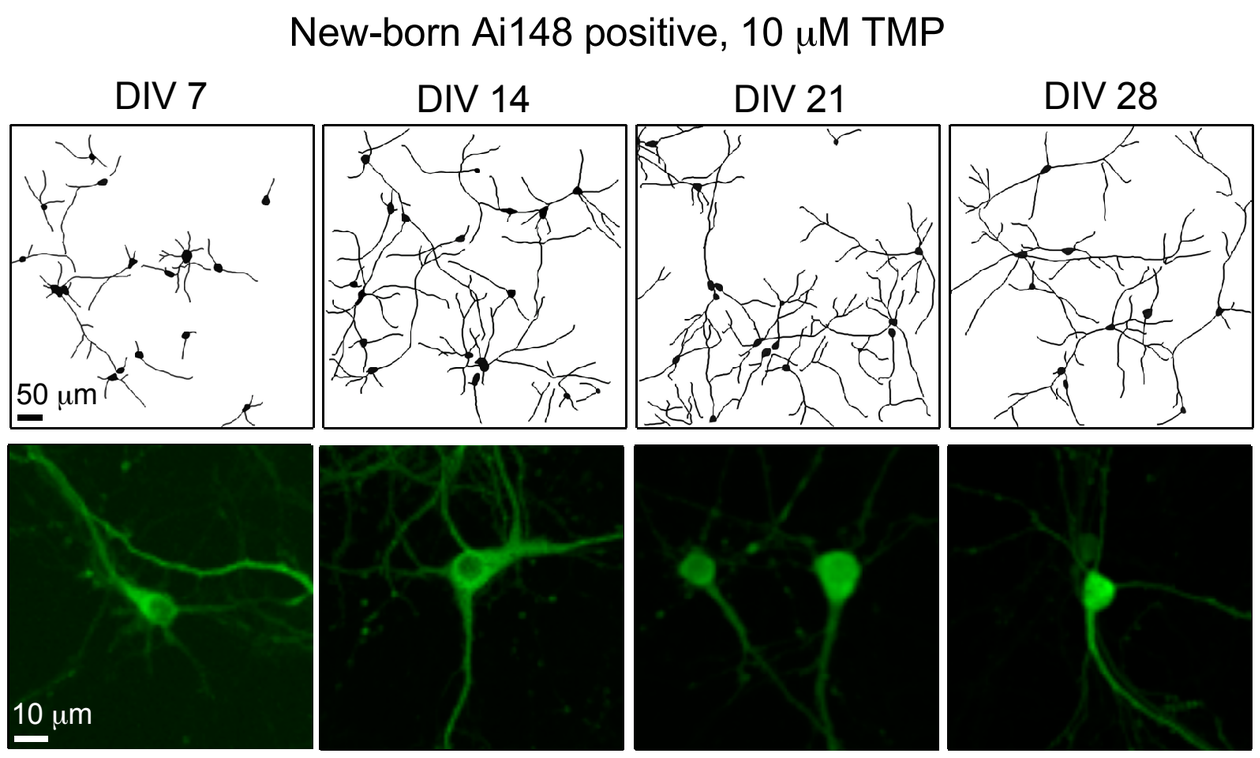
New-born Ai148 positive, 10 μM TMP
DIV 7
DIV 14
DIV 21
DIV 28
50 μm
10 μm

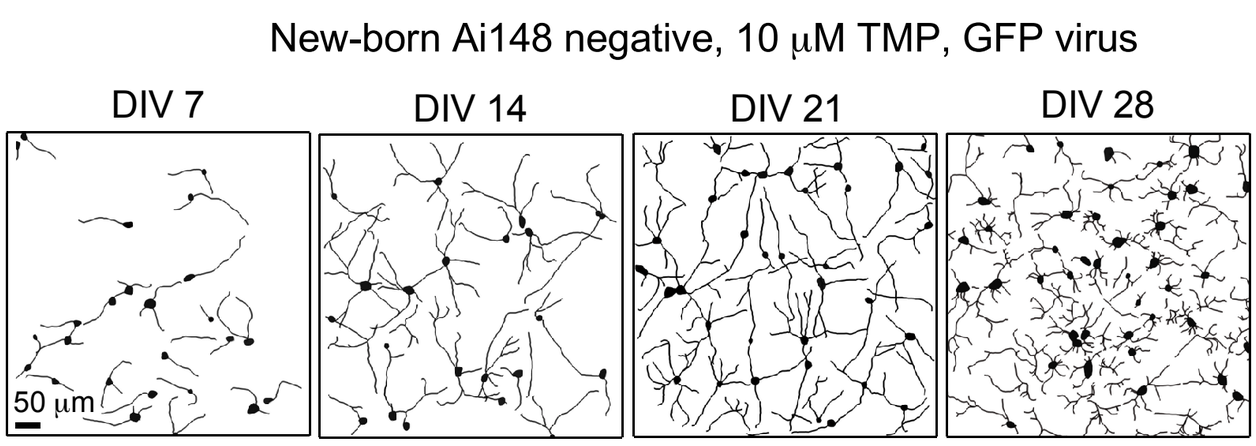
New-born Ai148 negative, 10 μM TMP, GFP virus
DIV 7
DIV 14
DIV 21
DIV 28
50 μm

D

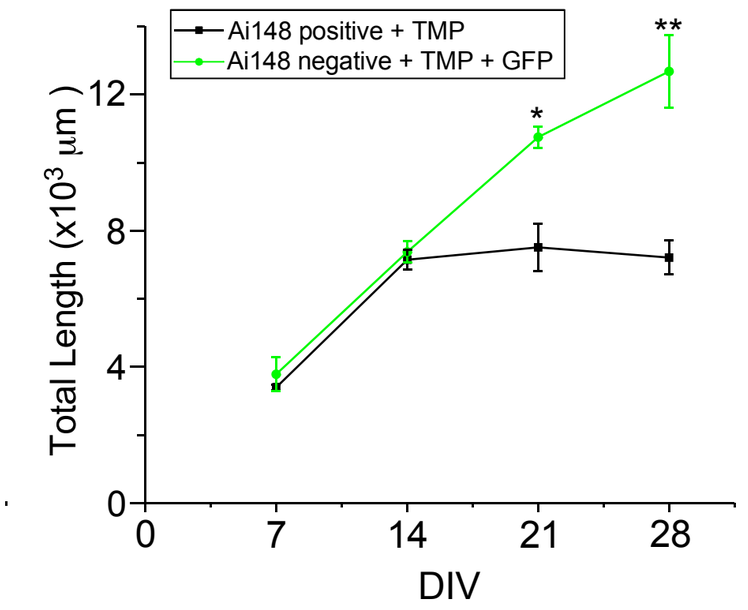
Ai148 positive + TMP
Ai148 negative + TMP + GFP
Total Length (x10³ μm)
12
8
4
0
*
**
0
7
14
21
28
DIV

E

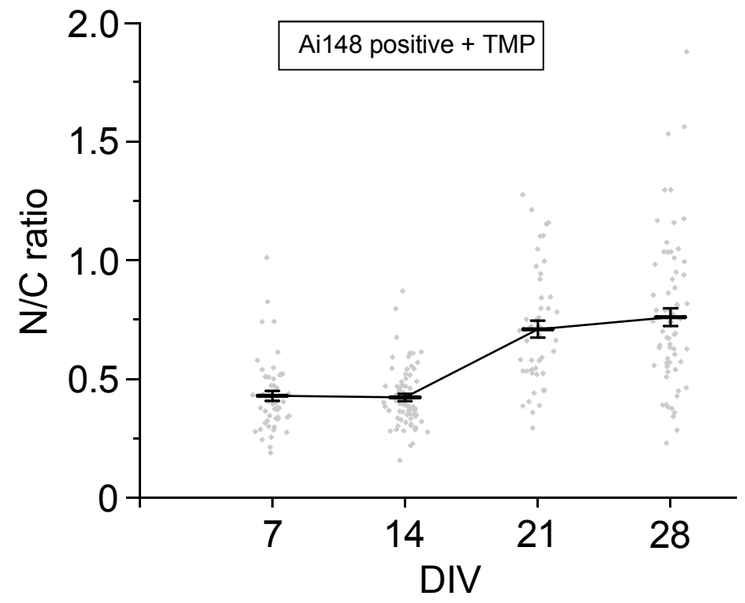
Ai148 positive + TMP
N/C ratio
2.0
1.5
1.0
0.5
0
7
14
21
28
DIV

F

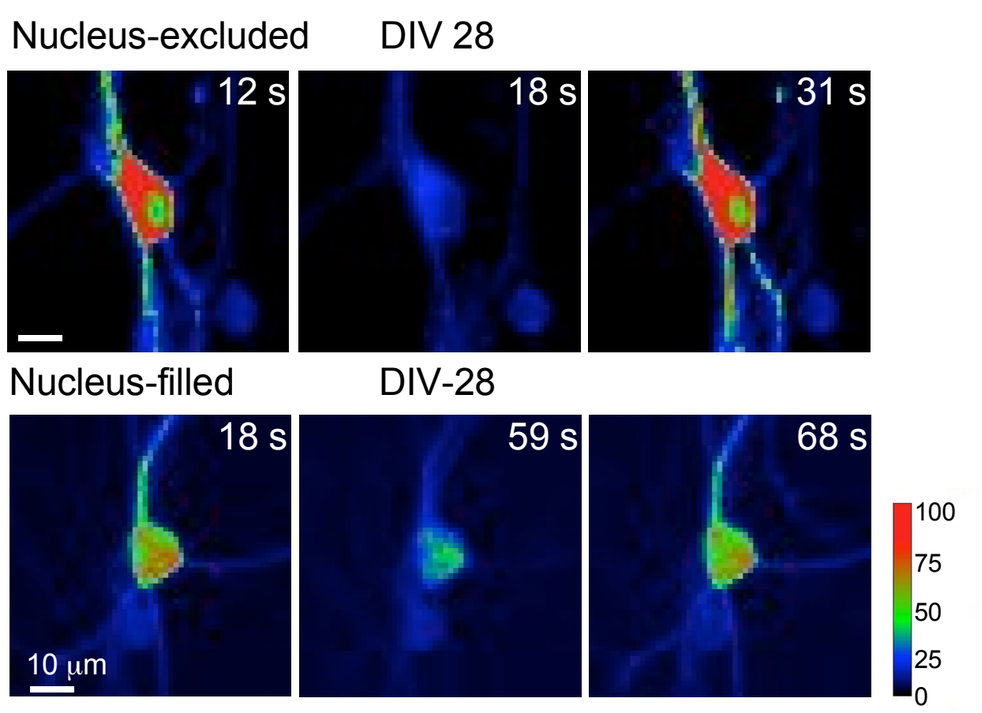
Nucleus-excluded
DIV 28
12 s
18 s
31 s
Nucleus-filled
DIV-28
18 s
59 s
68 s
10 μm
100
75
50
25
0

H

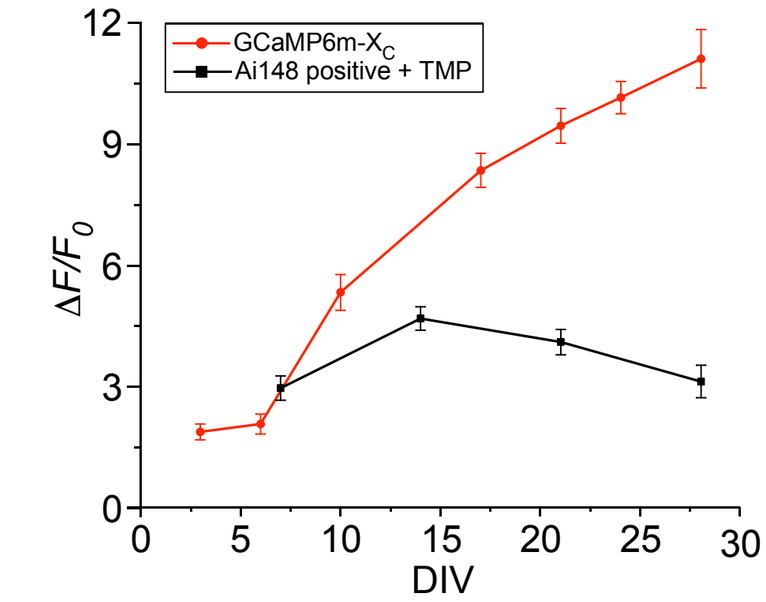
GCaMP6m-X_C
Ai148 positive + TMP
ΔF/F0
12
9
6
3
0
0
5
10
15
20
25
30
DIV

G

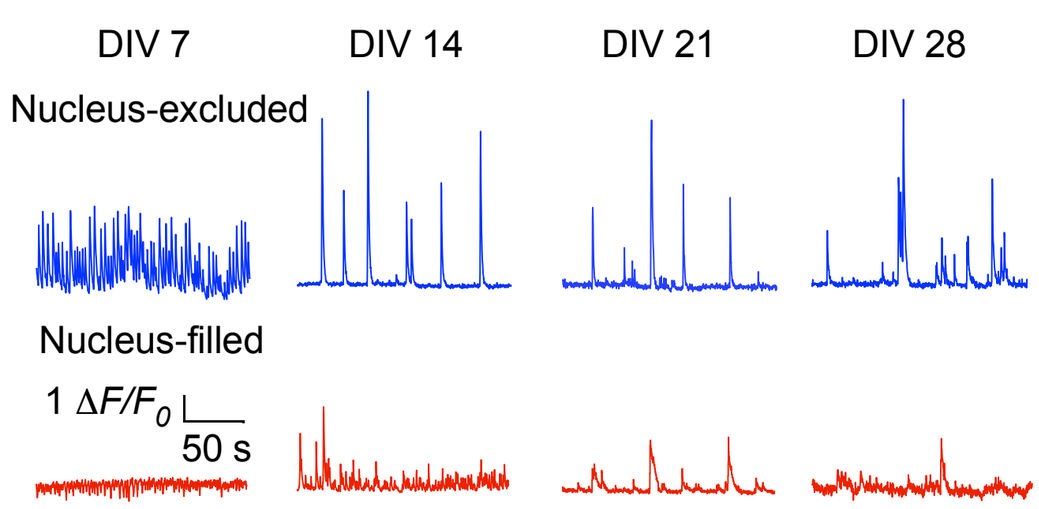
DIV 7
DIV 14
DIV 21
DIV 28
Nucleus-excluded
Nucleus-filled
1 ΔF/F0
50 s

I

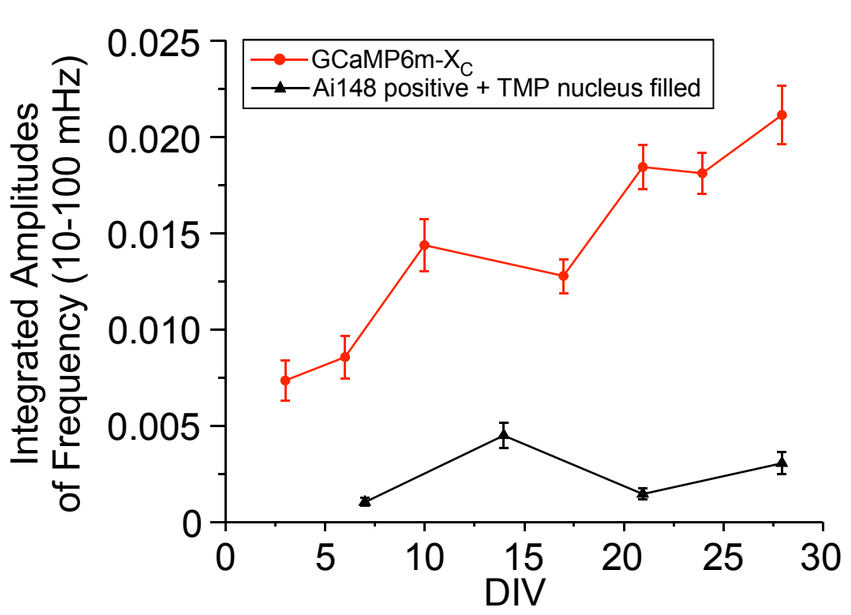
GCaMP6m-X_C
Ai148 positive + TMP nucleus filled
Integrated Amplitudes
of Frequency (10-100 mHz)
0.025
0.020
0.015
0.010
0.005
0
0
5
10
15
20
25
30
DIV

A

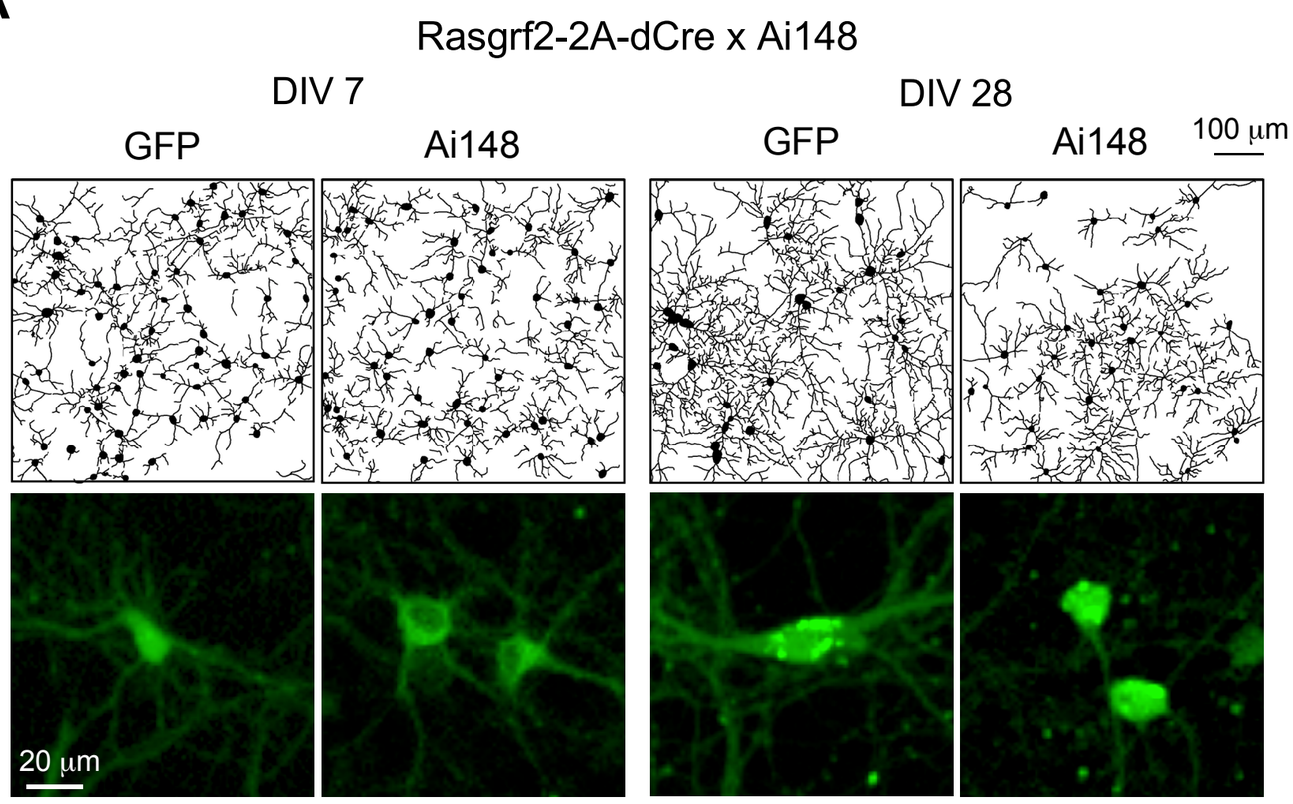
Rasgrf2-2A-dCre x Ai148
DIV 7
DIV 28
GFP
Ai148
GFP
Ai148
100 μm
20 μm

B

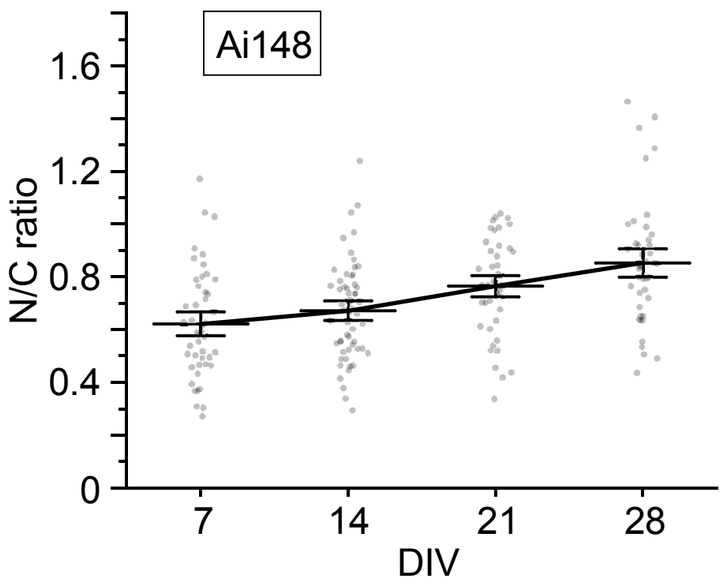
Ai148
N/C ratio
1.6
1.2
0.8
0.4
0
7
14
21
28
DIV

C

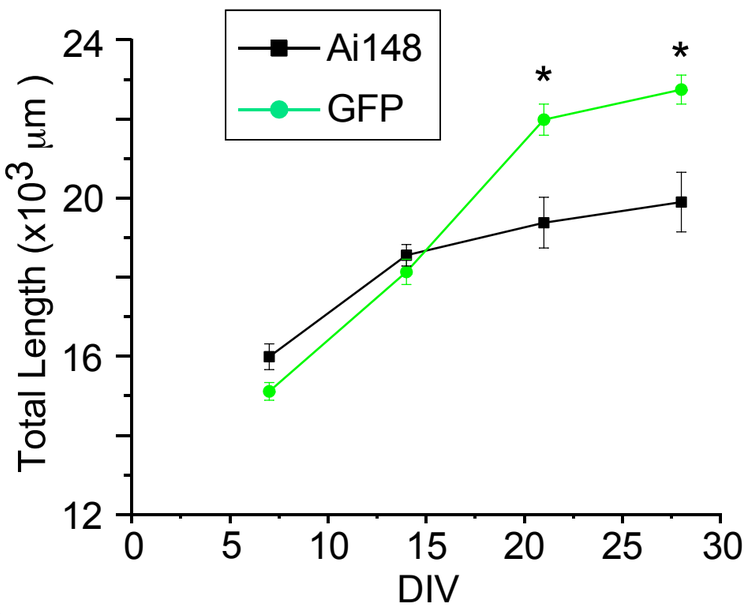
Ai148
GFP
Total Length (x10^3 μm)
24
20
16
12
0
5
10
15
20
25
30
DIV
*
*

D

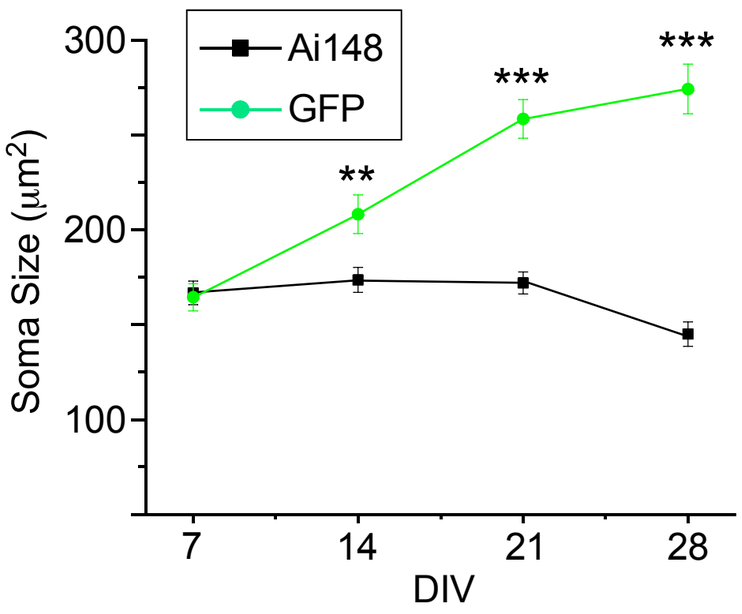
Ai148
GFP
Soma Size (μm^2)
300
200
100
7
14
21
28
DIV
**
***
***

E

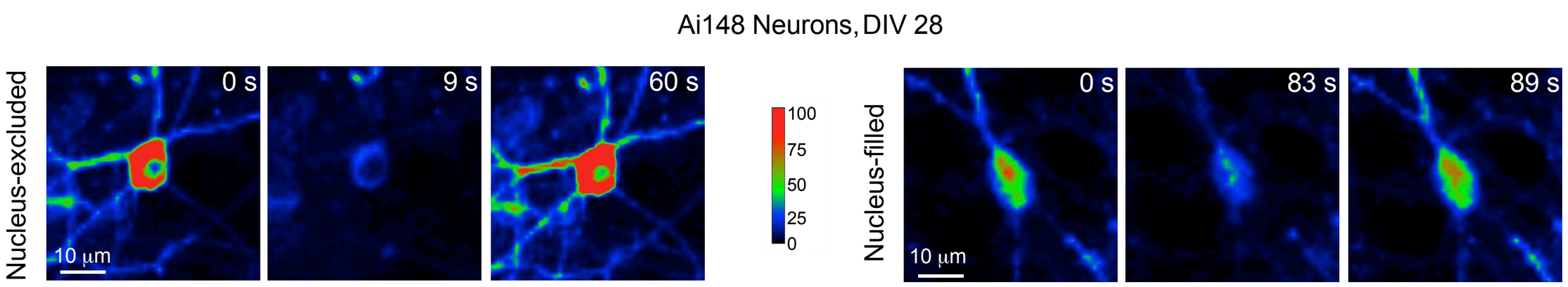
Ai148 Neurons, DIV 28
Nucleus-excluded
0 s
9 s
60 s
10 μm
100
75
50
25
0
Nucleus-filled
0 s
83 s
89 s
10 μm

F

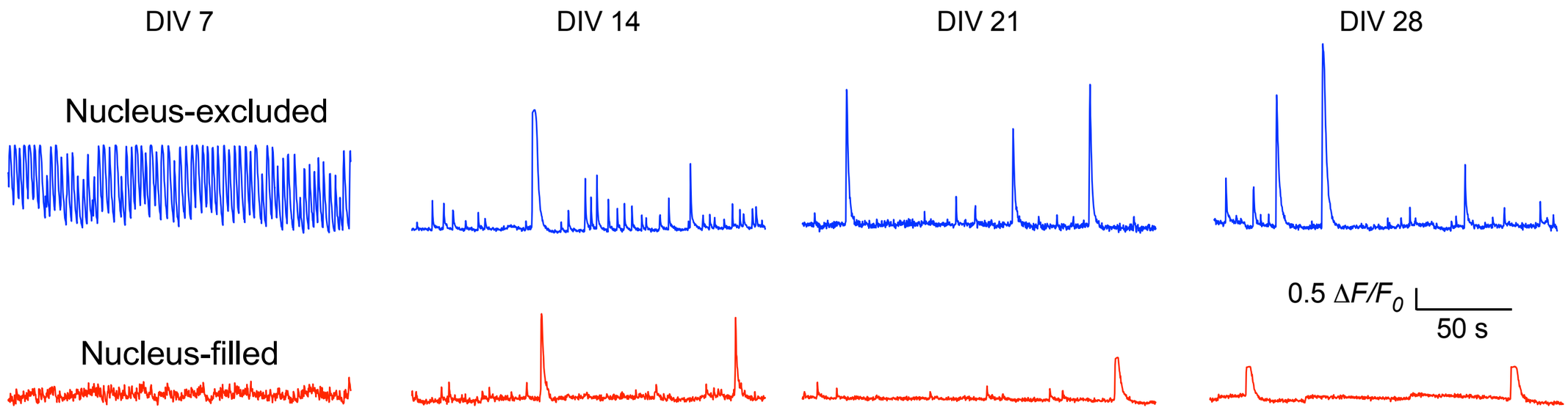
DIV 7
DIV 14
DIV 21
DIV 28
Nucleus-excluded
Nucleus-filled
0.5 ΔF/F0
50 s

G

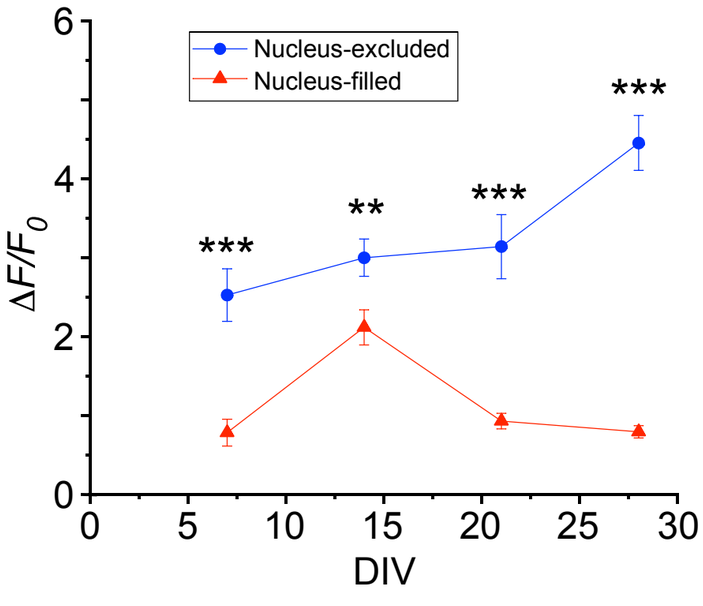
Nucleus-excluded
Nucleus-filled
ΔF/F0
6
4
2
0
0
5
10
15
20
25
30
DIV
***
**
***
***

H

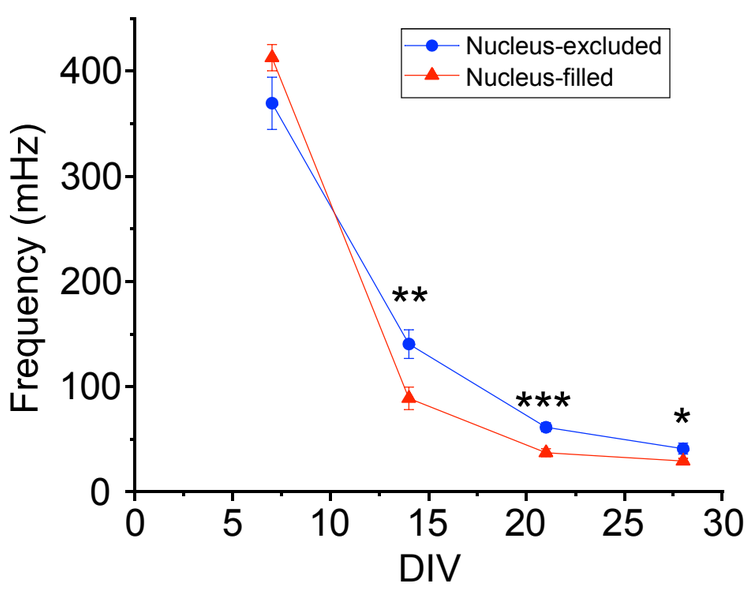
Nucleus-excluded
Nucleus-filled
Frequency (mHz)
400
300
200
100
0
0
5
10
15
20
25
30
DIV
**
***
*

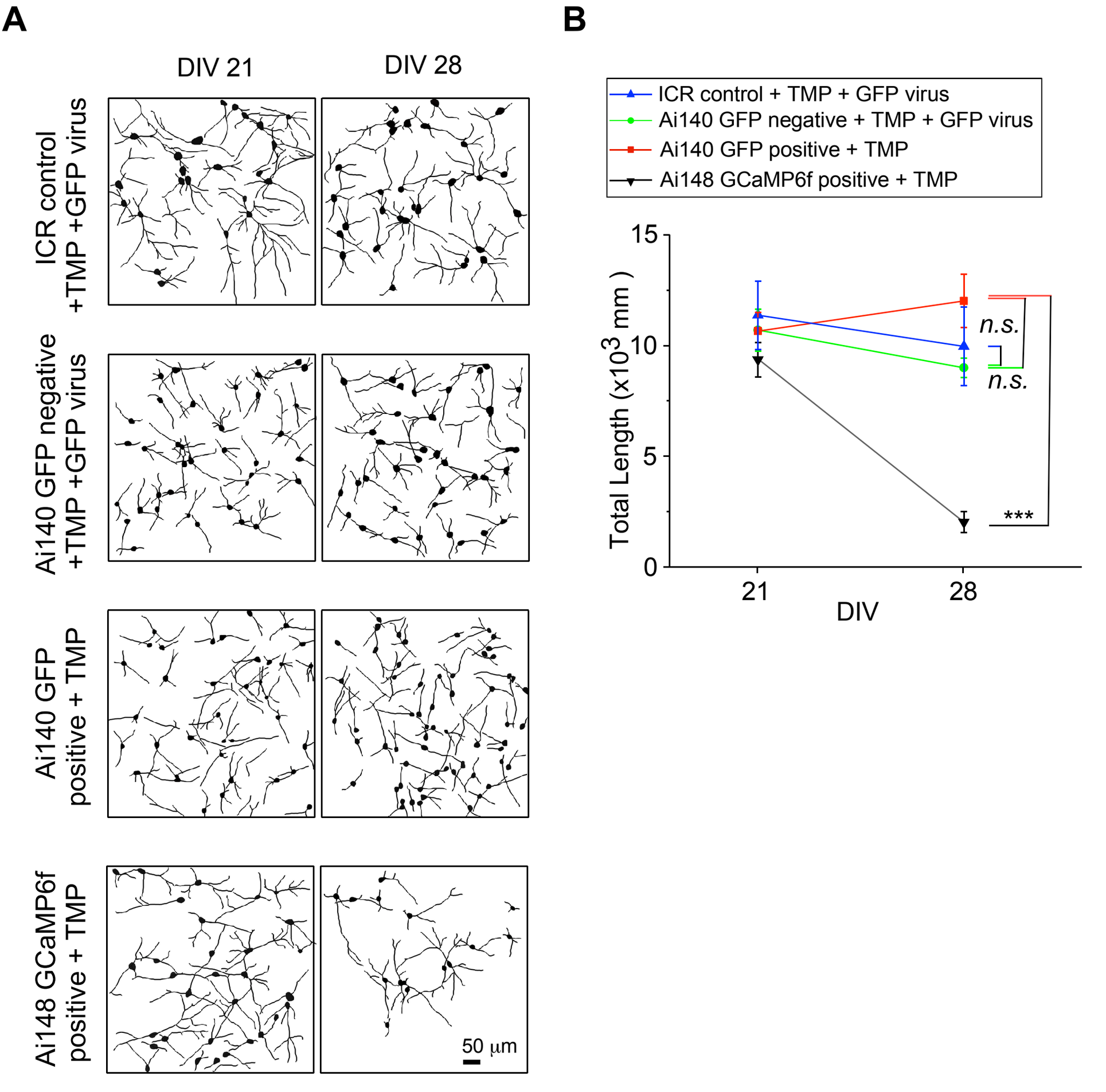
A
DIV 21
DIV 28
ICR control +TMP +GFP virus
Ai140 GFP negative +TMP +GFP virus
Ai140 GFP positive + TMP
Ai148 GCaMP6f positive + TMP
50 μm
B
ICR control + TMP + GFP virus
Ai140 GFP negative + TMP + GFP virus
Ai140 GFP positive + TMP
Ai148 GCaMP6f positive + TMP
Total Length (x10^3 mm)
15
10
5
0
21
28
DIV
n.s.
n.s.
***

A

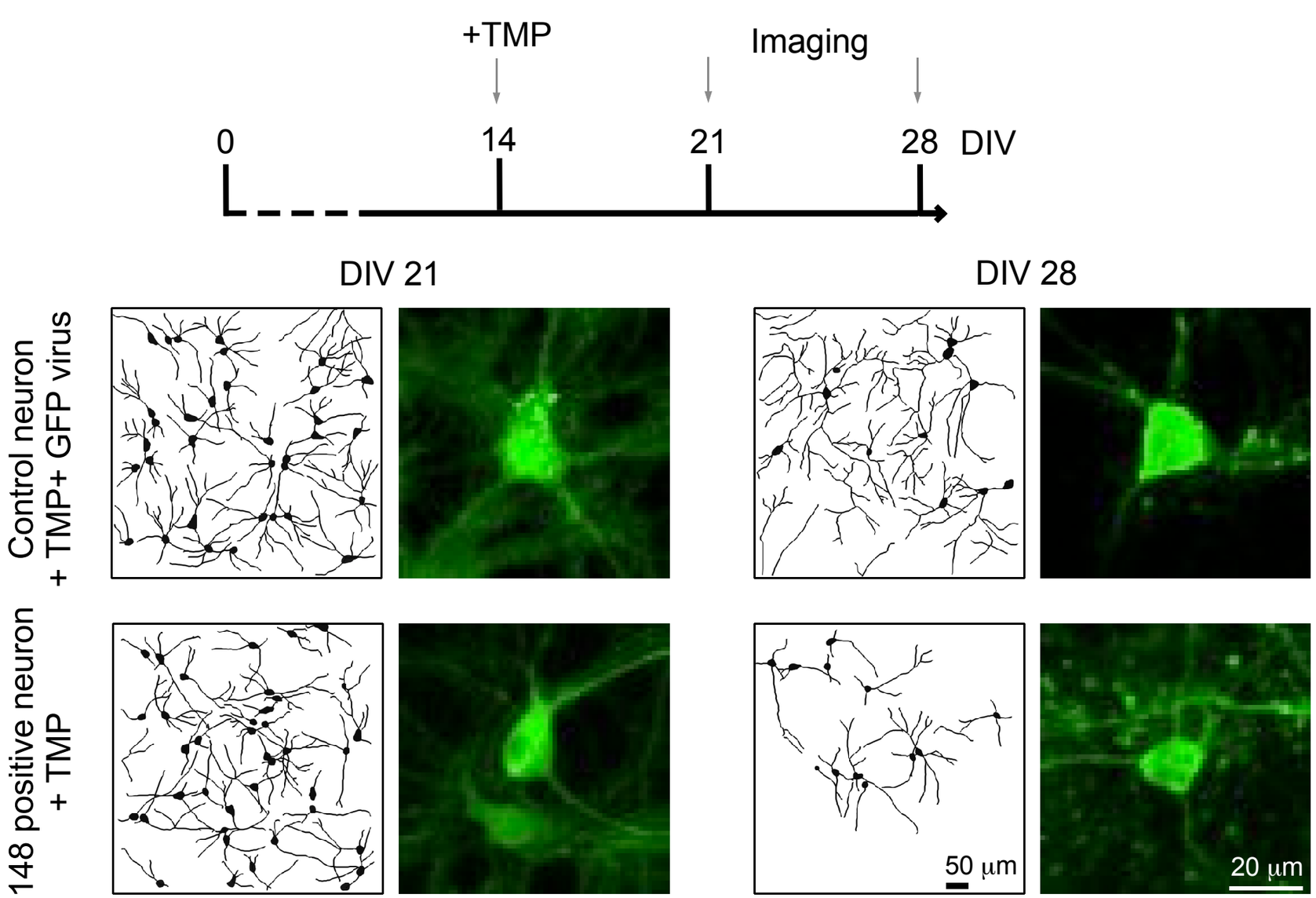
+TMP
Imaging
0
14
21
28 DIV
DIV 21
DIV 28
Control neuron + TMP+ GFP virus
Ai148 positive neuron + TMP
50 μm
20 μm

B

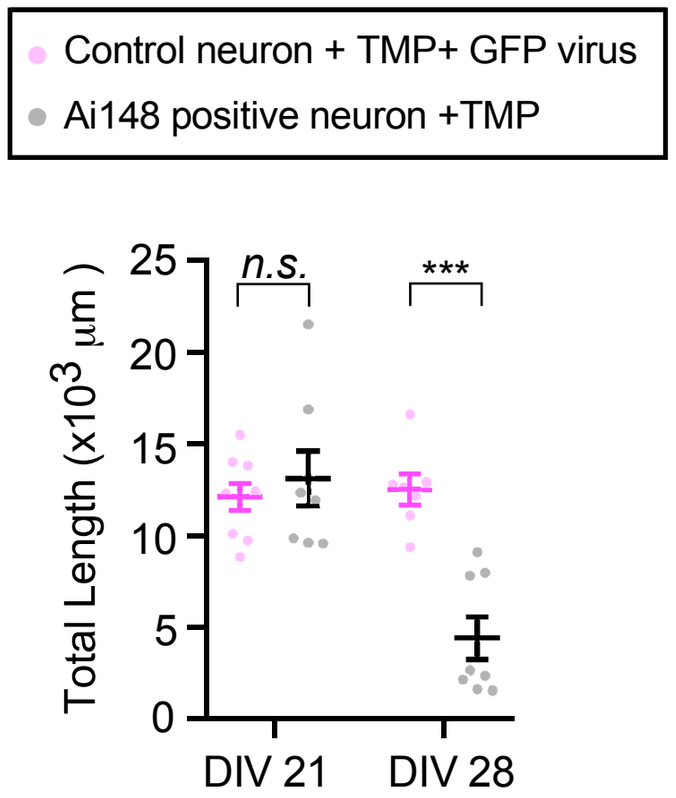
Control neuron + TMP+ GFP virus
Ai148 positive neuron +TMP
Total Length (x10³ μm)
n.s.
***
DIV 21
DIV 28

C

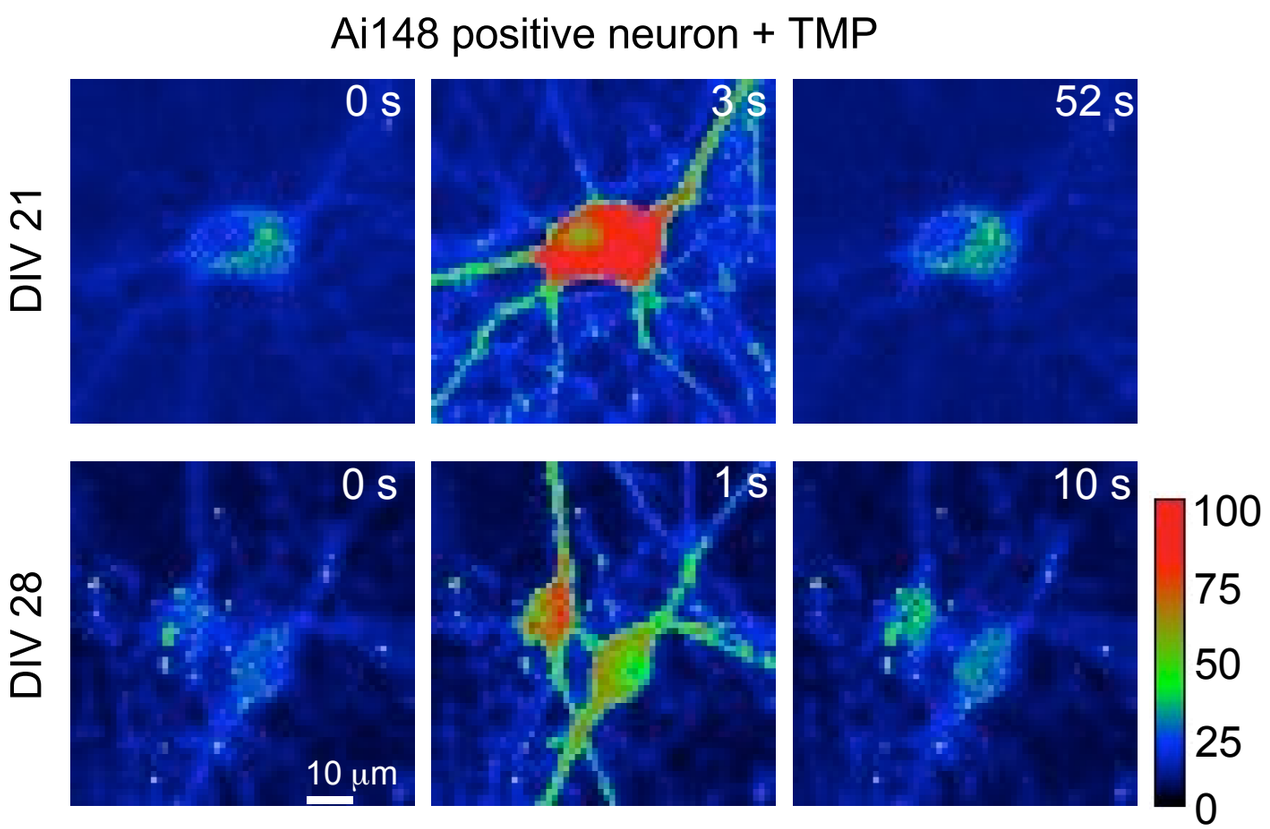
Ai148 positive neuron + TMP
DIV 21
DIV 28
0 s
3 s
52 s
0 s
1 s
10 s
10 μm
100
75
50
25
0

D

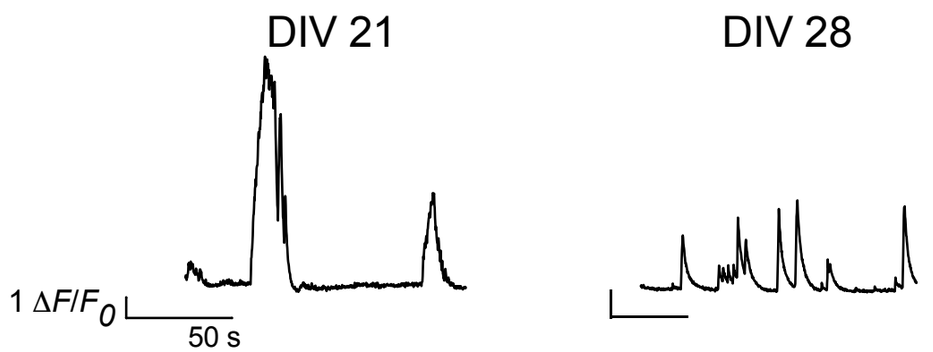
DIV 21
DIV 28
1 ΔF/F0
50 s

E

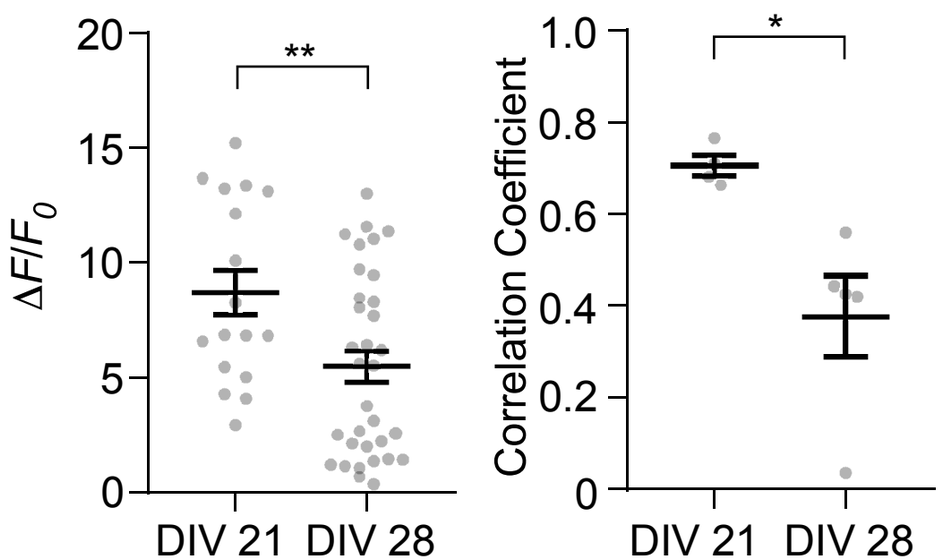
ΔF/F0
**
DIV 21
DIV 28
Correlation Coefficient
*
DIV 21
DIV 28

A

Emx1-Cre;Ai148

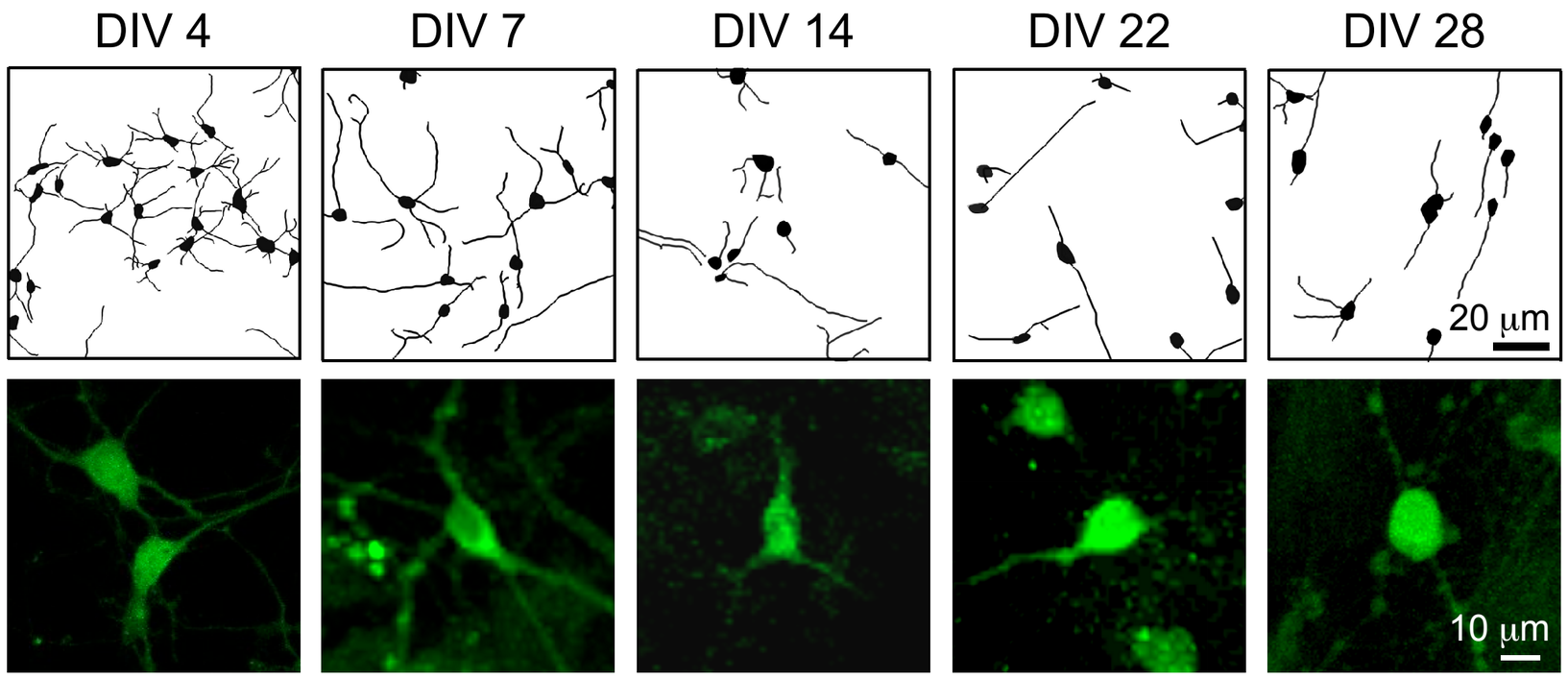

B

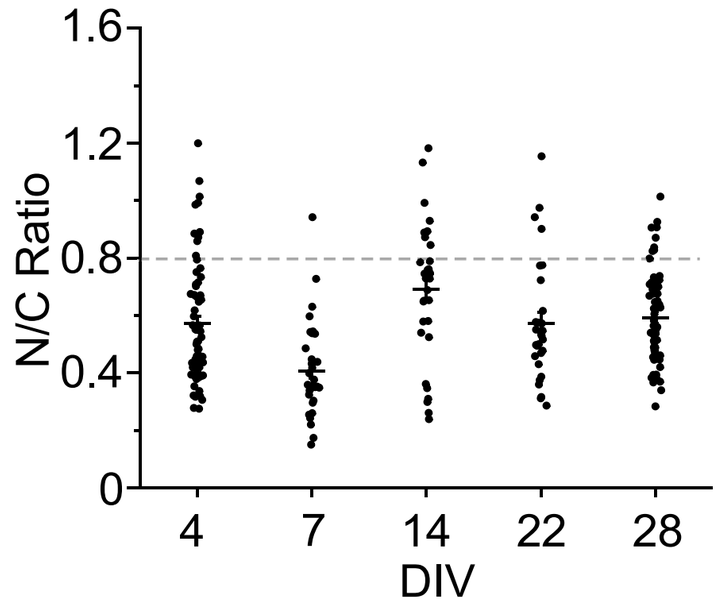

C

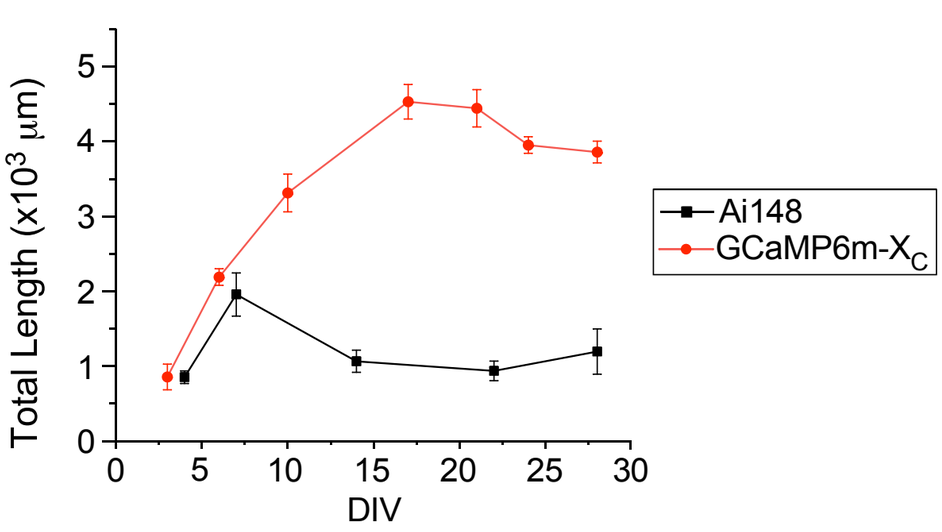

D

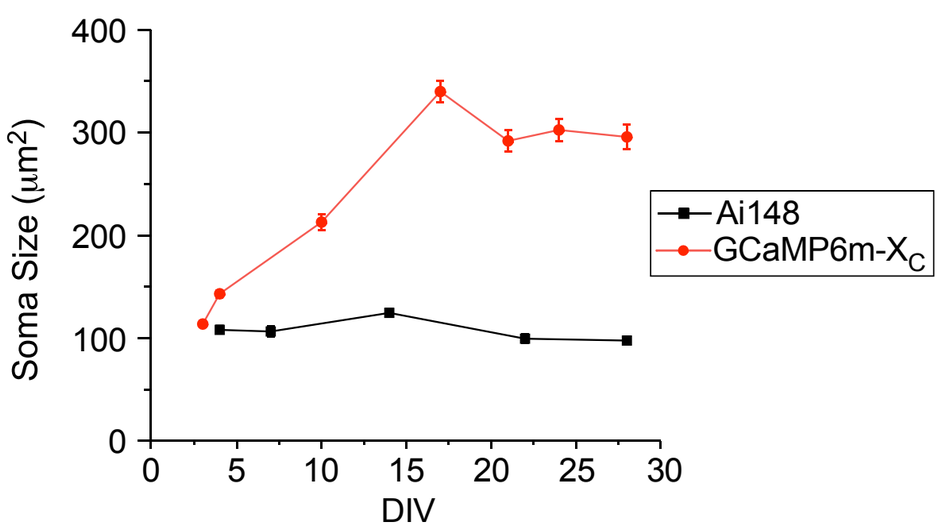

E

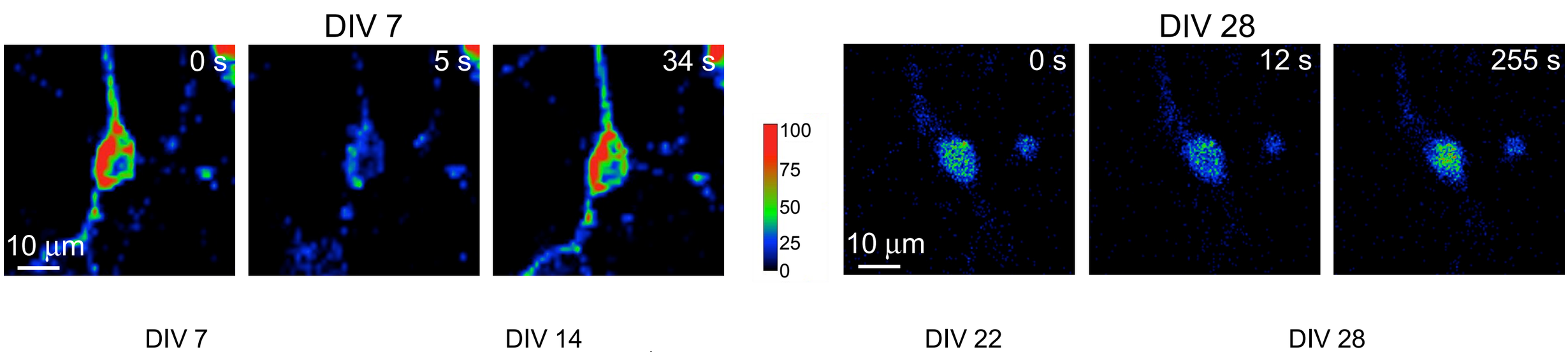

F

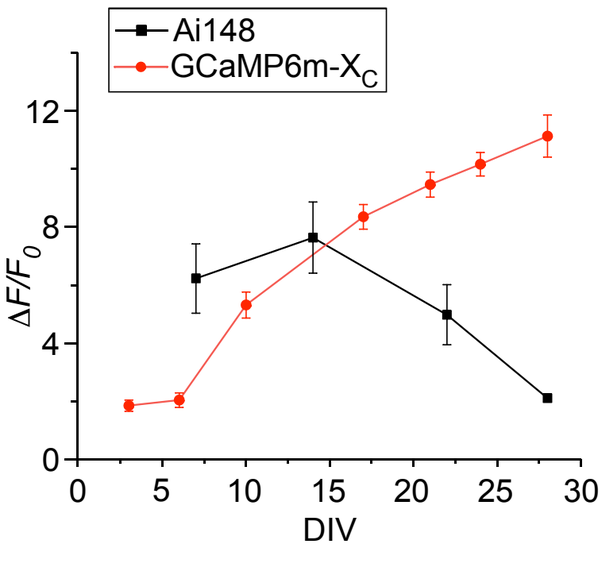

G

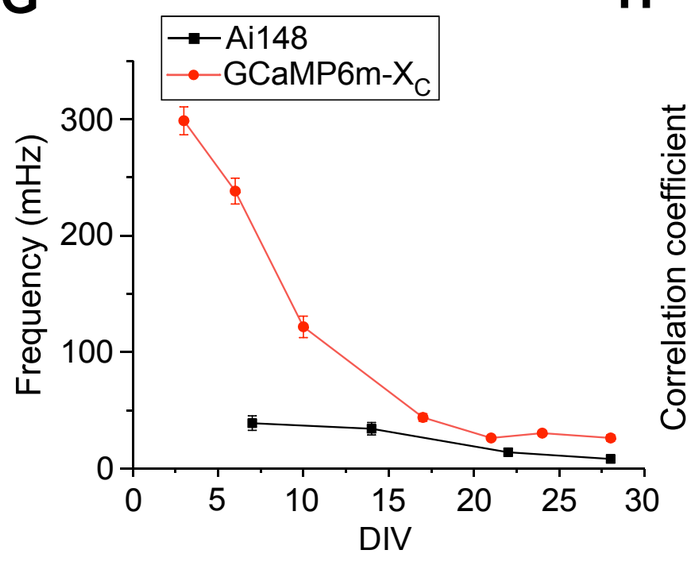

H

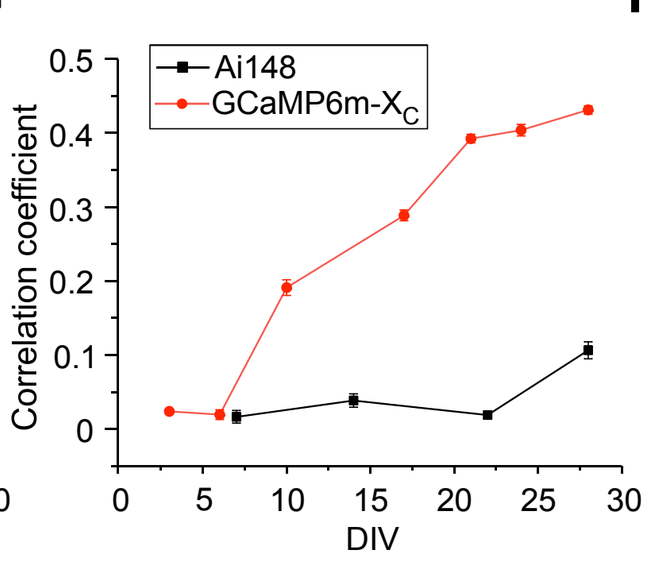

I